IMPROVED STATE ESTIMATION FOR MINIATURE AIR VEHICLES

by

Andrew Mark Eldredge

A thesis submitted to the faculty of

Brigham Young University

in partial fulfillment of the requirements for the degree of

Master of Science

Department of Mechanical Engineering

Brigham Young University

December 2006

Copyright © 2006 Andrew Mark Eldredge

All Rights Reserved

BRIGHAM YOUNG UNIVERSITY

GRADUATE COMMITTEE APPROVAL

of a thesis submitted by

Andrew Mark Eldredge

This thesis has been read by each member of the following graduate committee and by majority vote has been found to be satisfactory.

Date
Timothy W. McLain, Chair

Date
Randal W. Beard

Date
Christopher A. Mattson

BRIGHAM YOUNG UNIVERSITY

As chair of the candidate's graduate committee, I have read the thesis of Andrew Mark Eldredge in its final form and have found that (1) its format, citations, and bibliographical style are consistent and acceptable and fulfill university and department style requirements; (2) its illustrative materials including figures, tables, and charts are in place; and (3) the final manuscript is satisfactory to the graduate committee and is ready for submission to the university library.

Date

Timothy W. McLain
Chair, Graduate Committee

Accepted for the Department

Matthew R. Jones
Graduate Coordinator

Accepted for the College

Alan R. Parkinson
Dean, Ira A. Fulton College of
Engineering and Technology

ABSTRACT

IMPROVED STATE ESTIMATION FOR MINIATURE AIR VEHICLES

Andrew Mark Eldredge

Department of Mechanical Engineering

Master of Science

Research in Unmanned Air Vehicles (UAV's) continues to push the limitations of size and weight. As technical advances have made UAV's smaller and less expensive, they have become more flexible and extensive in their roles. To continue using smaller and less expensive components while retaining and even enhancing performance requires more sophisticated processing of sensor data in order for the UAV to accurately determine its state and thereby allow the use of feedback in controlling the aircraft automatically. This work presents a three-stage state-estimation scheme for the class of UAV's know as Miniature Air Vehicles (MAV's). The first stage estimates pitch and roll, the second stage estimates heading, and the third stage produces a position estimate and an estimate of wind speed and direction. All three stages make use of the extended Kalman filter, a framework for using a system dynamic model to predict future states and to update the predictions using weighted sensor measurements as they become available, where the weighting is based on the relative uncertainty of the dynamic model and the sensors. Using the three-stage state esti-

mation scheme, significant improvements in the estimation of pitch, roll and heading have been achieved in simulation and flight testing. Performance of the navigation (position and wind) stage is comparable to an existing baseline algorithms for position and wind, and shows additional promise for use in dead reckoning when GPS updates become unavailable.

ACKNOWLEDGMENTS

I wish to express thanks to the Members of my graduate committee, to my Chair, Professor Tim McLain for his helpful suggestions and critiquing of this work, and for helping trim down the scope of the work so that would fit within a few years of work.

Randy Beard is the man who taught me that state estimation is something to get excited about. In my mind's eye I can see him rocking back on his heels, marker in hand with that smile on his face, ready to reach the climax where he shows the class the observability matrix.

Steve Griffiths laid much of the groundwork and was the first to take on the miserable task of interfacing with the magnetometer and getting it to work. Steve also shared much of the burden of maintaining the fleet of MAGICC Lab airplanes and autopilots. His work facilitated not only mine, but the work of many lab members who have run experiments on lab airplanes.

Blake Barber, one of the most intimately familiar with the autopilot code, consulted with me on changes and how they would affect operation. Blake is also the lab's most accomplished Virtual Cockpiteer and could be called on to execute an experiment while I kept my hands ready to take over the airplane when things got hairy with an bold new or un-tuned estimation or control scheme. Blake is also responsible for many of the baseline algorithms and contributed to the material in Appendix A.

Dave Johanson is a man I wish I could always have on my team. Dave was the one I turned to when I needed help with the inner workings of the Virtual Cockpit,

and was the one who could come to the rescue when the compiler started doing something bizarre.

Jon Ostler has the steadiest camera aiming hands in the lab. It seems whenever there was a great shot that really did a good job of capturing the action, Jon was the man behind the camera.

Joe Jackson is a great listener. He brings in treats, and nearly made some textures I needed for the quaternion attitude window, and came up with an 11th hour hardware fix I needed. Joe also did a great job fielding questions and helping people that would normally ask me for help when it came down to crunch time.

Nate Knoebel is a capable extra set of hands and the best quaternion attitude controller tuner I know of. James Hall brought a mature eye to the proofreading process and was very helpful in pointing out things that could be clarified or misunderstood. Derek Kingston made himself available to discuss difficult theoretical questions and provided a veteran student's point of view when it came time to articulate an idea. James Hall brought a mature eye to the revision process, in reviewing manuscripts, pointing out locations where clarification is needed, and helping to implement dozens of changes.

Finally, I wish to acknowledge my lovely and talented wife Natalie, who endured my exuberant explanation of each new breakthrough and explained patiently to the children that daddy was busy with his airplanes again.

Table of Contents

Acknowledgements **xiii**

List of Tables **xxi**

List of Figures **xxv**

1 Introduction **1**

1.1 Motivation 1

1.2 Background 1

1.2.1 Coordinate frames, attitude representation, and equations of motion 1

1.2.2 State Estimation Using the Kalman Filter 2

1.2.3 Approaches to the Attitude Estimation Problem 3

1.2.4 Attitude Estimation for MAV's 4

1.2.5 State Estimation in the BYU MAGICC Lab 4

1.3 Contributions 4

1.4 Document Organization 5

2 Technical Approach **7**

2.1 Experimental Setup 7

2.1.1 Airframe 7

2.1.2 Autopilot 7

2.1.3 Hardware: 3-Axis Magnetometer 10

2.1.4 User Interface 11

2.1.5 Simulation Environment 12

2.2 Variables, Reference Frames and Notation 13

2.3 System Model 14

2.4 Review of the Extended Kalman Filter 17

2.4.1 Extended Kalman Filter Time Update 18

2.4.2 Extended Kalman Filter Measurement Update 19

2.4.3 Simplification: Independent Sensor Updates 20

2.5 Cascaded Filter Structure 21

2.6 Stage 1: Pitch and Roll Estimation 21

2.6.1 Stage 1: Time Update 23

2.6.2 Stage 1: Measurement Update 23

2.6.3 Other Stage 1 Tuning Considerations 25

2.7 Stage 2: Heading Estimation 26

2.7.1 Stage 2: Time Update 29

2.7.2 Stage 2: Measurement Update 29

2.7.3 Adaptation for Two-Axis Magnetometers 30

2.8 Stage 3: Position and Wind Estimation 30

2.8.1 Stage 3: Time Update 32

2.8.2 Stage 3: Measurement Update 32

2.8.3 Stage 3: Noise Model 33

2.9 Summary of Technical Approach 35

3 Simulation Results **37**

3.1 Stage 1: Pitch and Roll Estimation 37

3.1.1 Climb, Turn Maneuver 38

3.1.2 Steady Orbit Maneuver 41
3.2 Stage 2: Heading Estimation 47
3.3 Stage 3: Position and Wind Estimation 50
3.4 Summary of Simulation Results 55

4 Flight Test Results **57**
4.1 Stage 1: Pitch and Roll Estimation 57
4.1.1 Bank Angle Hold Experiment 57
4.1.2 Loiter experiment 58
4.2 Stage 2: Heading Estimation 65
4.3 Stage 3: Position and Wind Estimation 66
4.4 Summary of Flight Test Results 72

5 Conclusions and Future Work **75**
5.1 Conclusions 75
5.1.1 Pitch and Roll Estimation 75
5.1.2 Heading, Position and Wind Estimation 76
5.2 Future Work 77
5.2.1 Assumptions Revisited 77
5.2.2 Variation: Tuning Constant Covariance Matrix 77
5.2.3 Computational Streamlining 78

A Original State Estimation Algorithms **81**
A.1 Attitude Estimation with the Variable Gain Observer 81
A.1.1 Formulation 81
A.1.2 Kinematic (Time) Update 82
A.1.3 Accelerometer Updates 82

A.2 Position Estimation with GPS Smoothing 83
  A.2.1 GPS Smoothing Kinematic Update 83
  A.2.2 GPS Smoothing Measurement Update 84
A.3 Wind and Heading Estimation 85
A.4 Nonlinear Solver 87

B Inclusion of Climb information in Attitude EKF **91**
  B.0.1 Revised Filter Summary 93

C Airborne Magnetic Field Determination **95**
C.1 Magnetometer Calibration Data 95

Bibliography **98**

List of Tables

2.1 Standard MAV State Variables 15
2.2 Alternate State Variables 15
2.3 Variables Representing Sensor Measurements 15
2.4 Variables Used in the Extended Kalman Filter 19

C.1 Magnetometer Data Summary from North, East, South and West Runs 97

List of Figures

2.1 Ryan Holt Displays the Research Vehicle 8

2.2 Procerus Technologies Kestrel Autopilot, Versions 1.45 and 2.0 9

2.3 Furuno GH-80 GPS Receiver 9

2.4 Hardware Schematic 10

2.5 The PNI Mircromag 3-axis Magnetometer 10

2.6 Virtual Cockpit MAV Interface 12

2.7 The Aviones MAV Simulator 13

2.8 MAV Body Frame Coordinate Axes 14

2.9 Three-Stage State-Estimation Scheme 21

2.10 Relationship of Pitch, Angle of Attack and Flight Path Angles 24

3.1 Roll and Pitch Estimates With Truth Data During a Climb, Turn maneuver 38

3.2 Error in Pitch and Roll Estimates 39

3.3 Stage 1 Outputs During a Climb, Turn Maneuver 40

3.4 Stage 1 Gains During a Climb, Turn Maneuver 42

3.5 Roll and Pitch Estimates During a 150 Meter Orbit Maneuver 43

3.6 Stage 1 Errors During a 150 Meter Orbit 44

3.7 Stage 1 Predictions and Measurements During a 150 Meter Orbit 45

3.8 Stage 1 Gains During a 150 Meter Orbit 46

3.9 Heading Estimates and Error in Estimates Before and During an Orbit . . 48

3.10 Magnetometer Predictions and Measurements Before and During an Orbit 49

3.11 Heading Observer Gains Before and During an Orbit 50

3.12 Segment of Simulated Orbit Showing Actual Ground Track and Estimated Locations 51

3.13 Position vs. Time and Position Error vs. Time in Position Estimates . . . 52

3.14 North and East Wind Estimates 53

3.15 Inputs to Estimator With Ground Track and Ground Speed 54

4.1 Bank Angle Hold at 55 Degrees Using the Variable Gain Observer for Feedback Control. 59

4.2 Bank Angle Hold at 55 Degrees Using the EKF for Feedback Control. . . 60

4.3 Bank Angle Estimates During 15 Meter Radius Orbit 61

4.4 Difference Between EKF and VGO Bank Angle Estimates During 15 Meter Radius Orbit 62

4.5 Accelerometer Predictions and Measurements During 15 Meter Radius Orbit 63

4.6 Sensor Correction Gains During 15 Meter Radius Orbit 64

4.7 Heading Estimates During a Right-handed Rectangular Pattern 65

4.8 Magnetometer Predictions and Measurements During a Right-handed Rectangular Pattern 67

4.9 Heading Estimates During a Right-handed Rectangular Pattern 68

4.10 Position Estimate During a Segment of a Rectangular Pattern 69

4.11 Position Estimates With GPS Updates to the EKF Stopped Mid-experiment 70

4.12 Position Estimates, Difference in Position Estimates in Time 71

4.13 Wind Estimate While in a Rectangular Pattern 72

4.14 Observer Inputs and Helpful GPS Ground-track and Ground-speed Estimate from a Rectangular Pattern 73

A.1 Relationship Between Ground, Air, and Wind Velocities. 85

A.2 $V_w = 10$ m/s, $\xi = 0.0$. 86

A.3 Execution Time vs. Number of Data Points for the Solution of Equation (A.20). 88

B.1 Relationship of Pitch, Angle of Attack and Flight Path Angles 91

C.1 Calibration Flight Data From the PNI Micromag 3-axis Magnetometer. 96

Chapter 1

Introduction

1.1 Motivation

Unmanned Air Vehicles (UAV's) continue to have an increased role in fields of defense, homeland security, and civil applications. These and other fields can benefit from the use of Miniature Air Vehicles (MAV's) especially as improvements in micro-controller, battery and propulsion technologies are proliferated, making the use of MAV's increasingly cost effective.

Most scenarios in which MAV's are used, particularly automated data collection applications, presume that the vehicle has accurate information about vehicle state—such as location, altitude, heading, roll and pitch angles—in order to accurately resolve other sensor information to a global reference frame. Accurate state information is also necessary for automated control of the vehicle. When state information of the air vehicle is improved, the quality of acquired data is improved.

State estimation is challenging for MAV's due to several factors, especially limited computational power and noise on the sensors. Due to these factors, efficient and accurate state estimation algorithms become critically important to make a reliable, inexpensive unmanned system feasible.

1.2 Background

1.2.1 Coordinate frames, attitude representation, and equations of motion

In any study of state estimation, it is helpful to review linear transformations, attitude representations and the supporting mathematics. Aerospace textbooks provide a framework for discussion of aircraft states including geographic location and attitude. They also contain established equations of motion, aircraft dynamics and kinematics for six degree-of-freedom models [25][19].

Shuster provided a thorough review of attitude representations and associated kinematic equations [24]. This treatment, as with much of the literature concerning attitude estimation, is written primarily with spacecraft in mind. A similar treatment, aimed at state representation for aircraft comes from Phillips, Hailey and Gebert [16]. These papers provide a basis for discussions on attitude representation and transformations in special orthogonal three space (S0(3)), in which all three-dimensional rotations can be represented.

1.2.2 State Estimation Using the Kalman Filter

The Kalman filter was introduced as a means of estimating the state of a linear system in 1960 [11] and has since found wide application as an optimal linear observer in situations where there are multiple sources of state information. The Kalman filter is particularly useful in cases where there are equations of motion which model the response of a system in time, and sensor measurements which are related to the states of interest. There now exist numerous treatments of the Kalman approach to suit the taste of the student of estimation. The first chapter of [15] provides a clear and concise introduction to the Kalman filter. Gelb [8] gives a complete treatment which includes the adaptation of the Kalman filter for nonlinear systems, such as with attitude estimation. Some other adaptations which show promise for the attitude estimation problem include the use of an unscented transform, described in [10] and the SCAAT, or single constraint at a time approach, described in [27]. The unscented filter uses a few discreetly sampled points to parameterize mean and variance, and generalizes elegantly to the nonlinear case. The SCAAT approach streamlines the measurement process, decreasing latency in measurement correction by applying single measurements rather than an entire vector of measurements at once. The same author also provides a useful introduction to the Kalman filter [26].

1.2.3 Approaches to the Attitude Estimation Problem

Attitude estimation is necessary for a wide range of autonomous systems. Fiscal, computational and operational constraints have generated multiple approaches using a variety of sensors. While the Kalman Filter has found application for cost-sensitive applications, where it is effective in fusing low-cost, light-weight, relatively noisy sensor data, it has also been applied on modern fighter jets in a situation where true airspeed, angle of attack, and other very useful sensor information is available [14]. On the other end of the mass and cost spectrum is an effort to miniaturize and proliferate autonomous systems. Toward this goal, the use of inexpensive, lightweight sensors is being investigated [6][3].

Additional computation is useful in improving accuracy of estimators, one approach involves a technique called smoothing, in which one Kalman filter propagates the states forward until a sensor measurement is received, then a second Kalman filter running backward in time is use to "smooth" the estimate [20] [21] [22]. Other approaches include solving an optimization problem using simultaneous vector measurements as inputs and the vehicle attitude as the variable being optimized (Wahba's problem) using an iterated least squares [7] or quasi-Newton method [23]. One use of the extended Kalman filter simultaneously calibrates and uses magnetometer measurements in an attitude estimation problem [5].

A great portion of the research in the field of attitude estimation deals with satellites and other spacecraft. One of the difficulties that arises in adapting these algorithms for use on air vehicles is that spacecraft are generally in fixed orbits, free from some dynamic accelerations experienced by an aircraft on a changing flight path. For a UAV, gravitational and magnetic field measurements are often the most effective earth frame vector measurements which are available. In sensing the gravity vector, however, the effect of dynamic loading cannot be ignored without an impact on observer performance. Psiaki has extended a quasi-Newton approach to include dynamic acceleration measurements [17]. Other work has approached the problem of attitude estimation of accelerated bodies, such as the walking robot in [18].

1.2.4 Attitude Estimation for MAV's

The Kestrel^{TM} autopilot, which is used in the BYU MAGICC Lab and in this research, is equipped with MEMS rate gyros and accelerometers. Other examples of attitude estimation research that use a similar sensor package include [9], [2] and[1]. The original state estimation scheme used in the BYU lab is detailed in [4]. Further investigation on the same platform is detailed in [13] and [12].

1.2.5 State Estimation in the BYU MAGICC Lab

Work on control algorithms in the BYU MAGICC Lab has advanced to a point where waypoint paths can be flown autonomously in a reliable and repeatable manner by restricting the envelope of operation to relatively small pitch and roll angles. This limitation is due in part to the current attitude estimation scheme, which provides sufficient stability for flying waypoint paths, but its accuracy is flawed during turns and other dynamic loading situations. For example, aircraft flown under the current estimation scheme have exhibited a tendency to lose altitude immediately following execution of a waypoint turn. It has become desirable to revisit the problem of attitude estimation in an effort to improve the autopilot's ability to accurately fly desired paths by improving the accuracy of the estimated states. The improvements discussed in this work increase the controllable flight envelope of the vehicle, improve control of altitude during turns, and improve performance of algorithms which rely on state information to locate ground targets accurately.

In addition to enhancements to the existing flight envelope, improved attitude estimation addresses the special challenges of large angle maneuvers, sustained turns and orbits. These operations have been limited by a weakness in the current attitude estimation scheme, referred to herein as the Variable Gain Observer (VGO).

1.3 Contributions

The research described in this thesis formulates a state estimation structure which includes estimates of pitch, roll and heading angles, as well as geographic location and estimates of wind speed and direction. The estimation algorithms are formulated and tested in simulation and hardware. The work described herein represents an improvement over baseline algorithms in the accuracy of the attitude estimate, and provides the capability to estimate a heading without reliance on the GPS measurement, an important capability to increase robustness of the autopilot to GPS system failures. Also represented is the possibility of estimating wind without changing heading, which becomes important in situations when a MAV flies a long mission without turning.

1.4 Document Organization

This thesis presents a three-stage, cascaded state-estimation scheme, described in Chapter 2. Implementation details such as hardware and test environment are covered in Section 2.1. The mathematical model used to represent the MAV and the derivation of the observers is covered in Section 2.3. General notation and background on the extended Kalman filter is presented in Section 2.4, while Section 2.5 outlines the structure of the estimation scheme, with individual stages treated in detail in Sections 2.6 through 2.8.

Simulation results are given for the estimation scheme in Chapter 3, followed by hardware results in Chapter 4. Each chapter contains results for each stage, given in the order of each successive stage. In these chapters, comparisons are made to the original state estimates taken simultaneously with the new estimates. A description of the baseline state estimation algorithms is contained in Appendix A. Chapter 5 contains conclusions and descriptions of possible further development which may be investigated, including augmentations to attitude estimation and ways to decrease the computational burden, speeding the processing of each stage. One of the proposed changes to the attitude estimation algorithm is detailed in Appendix B. Appendix C contains data used in determining an inertial frame magnetic field in the flight test area, as well as sensor calibration data.

In this document, we will call the original attitude estimation scheme the Variable Gain Observer (VGO). This thesis describes the development of a new attitude estimation scheme which makes use of an extended Kalman filter. For brevity, the new scheme will simply be called the extended Kalman filter (EKF), note, however, that some references to the EKF such as those in Section 2.4 are referring to the extended Kalman filter generally, while at other times, particularly in Chapter 3 and beyond, EKF refers to specific implementations which are based on the extended Kalman filter.

The second and third stages of the state estimation scheme are compared to original estimates which have already been implemented on the autopilot and detailed in Appendix A. These algorithms include a GPS smoothing program which interpolates geographic position between GPS measurements. Another algorithm uses groundtrack and groundspeed from GPS in conjunction with airspeed measurements to determine wind direction and speed, as well as vehicle heading.

Chapter 2

Technical Approach

This chapter describes a miniature air vehicle (MAV) test bed, including airframe, autopilot, sensors, operator interface and simulation environment. The Extended Kalman Filter (EKF) is reviewed, and a three stage MAV state estimation scheme, which makes use of the EKF at each stage, is developed.

2.1 Experimental Setup

The experimental apparatus consists of an autopilot-equipped MAV which communicates via radio modem with a ground station. The ground station consists of a communications box and a laptop computer running Virtual Cockpit software. Estimation algorithms are tested on the ground in a simulator prior to flight testing.

2.1.1 Airframe

The airframe used in these experiments is a kit-built flying-wing design of expanded polypropylene (EPP) construction, with a 48 inch wingspan. The foam construction lends itself well to addition of components and is extremely durable. This flexibility and durability has proved particularly useful when testing new flight control schemes and mission specific hardware. Propulsion is by an electric motor. The fully-loaded weight of the aircraft is under two pounds.

2.1.2 Autopilot

The autopilot used in these experiments is the Kestrel$^{\text{TM}}$0.05inautopilot available from Procerus Technologies. The Kestrel autopilot is equipped with a RabbitCore 3000 series microprocessor, solid-state rate gyros and accelerometers, and

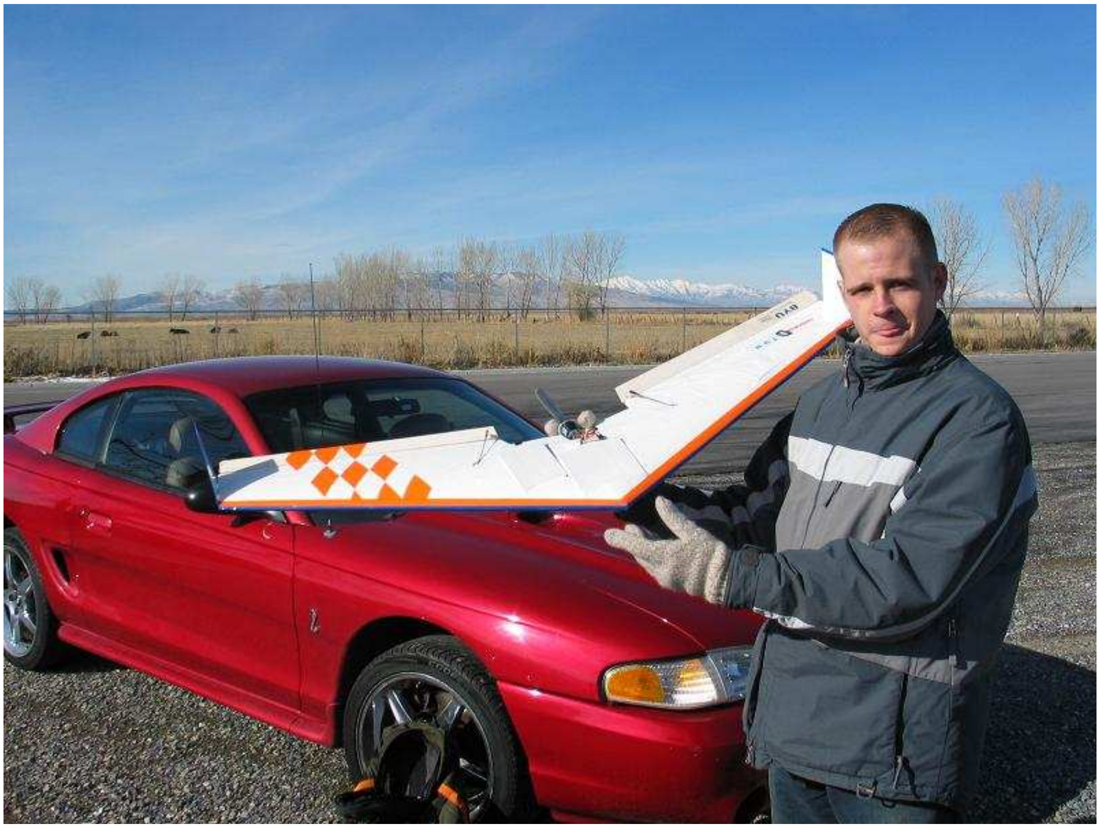

Figure 2.1: Ryan Holt Displays the Research Vehicle

pressure sensors. The autopilot is also equipped with serial, I^2C, serial peripheral interface (SPI) and general purpose digital I/O ports. The autopilot used in this research is a Kestrel 1.45 model interfaced an external magnetometer over the SPI interface. The external unit is a Micro-Mag model manufactured by PNI Corporation, mounted on the wing-tip, away from other electrical components. The magnetometer communicates with the autopilot via a SPI bus. The MAV test bed is also equipped with a Furuno GH-80 Global Positioning System (GPS) receiver, connected by an asynchronous serial interface to the Kestrel autopilot.

The autopilot's micro-controller is programmed using the C programming language with some extensions specific to the controller. No matrix libraries or operators were used on the processor. Instead, matrix operations were expanded to their long form, which allowed some computational streamlining by eliminating some redundan-

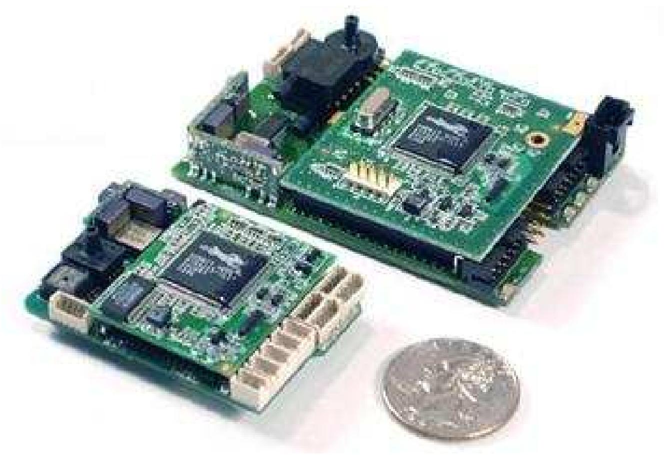

Figure 2.2: Procerus Technologies Kestrel Autopilot, Versions 1.45 and 2.0

Figure 2.3: Furuno GH-80 GPS Receiver

cies in matrices with symmetric structure and reduction in the number of operations such as multiplication by matrix elements equal to zero.

The existing autopilot software has basic state estimation and can execute auto takeoff, fly designated waypoints, land automatically, and communicate telemetry to the ground station. It also provides means to record many of the variables for subsequent download to the Virtual Cockpit on the ground station laptop computer. This feature is particularly useful when it is desired to record data at a rate exceeding the transmission capabilities of the radio link.

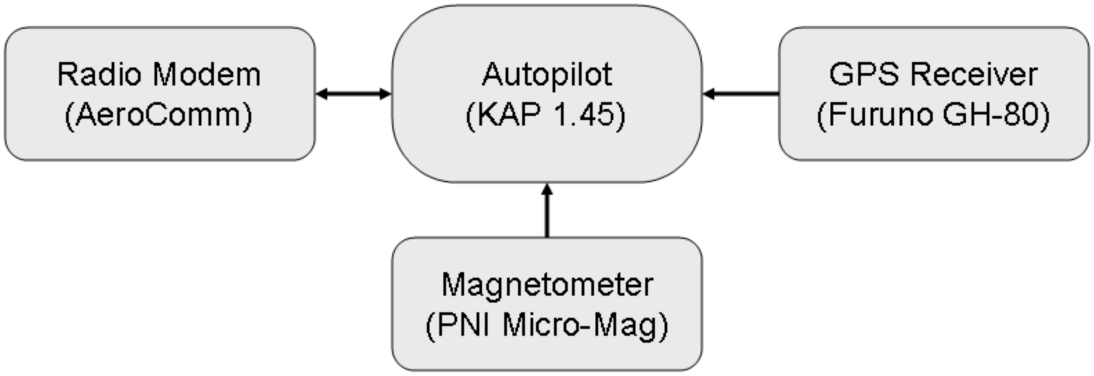
Radio Modem
(AeroComm)
Autopilot
(KAP 1.45)
GPS Receiver
(Furuno GH-80)
Magnetometer
(PNI Micro-Mag)

Figure 2.4: Hardware Schematic

2.1.3 Hardware: 3-Axis Magnetometer

The PNI digital 3-axis magnetometer shown in Figure 2.5 provided a natural choice for magnetic sensing earth's magnetic field aboard a MAV. The existing autopilot hardware and software are well suited to interface with this device using its SPI. The device has on-board temperature compensation and features the ability to select resolution, which trades off with latency between the query and delivery of the measurement.

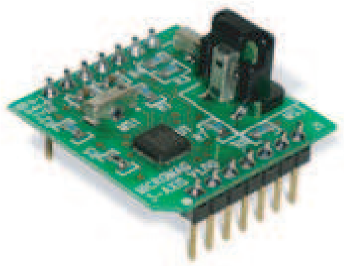

Figure 2.5: The PNI Mircromag 3-axis Magnetometer

The magnetometer is queried by the autopilot's processor for the magnetic field one axis at a time. The request includes a desired resolution and the axis to be measured. When the command is received, the magnetometer performs the measurement then signals the autopilot that the data is ready. The autopilot then reads a signed integer value from the magnetometer which corresponds to the strength of the magnetic field on the axis requested.

Ideally, the magnetometer should be calibrated in a known magnetic field, with the integer values returned from the autopilot converted to units of magnetic flux. A magnetic field standard being absent, magnetometer data in known operating conditions can be used. This is accomplished with the vehicle on a known, constant heading while magnetometer data is logged for each axis, along with pitch and roll information from the autopilot. Rotating the magnetic field measurements through the pitch and roll angles gives a measurement at each sample similar in direction to the published magnetic field data for the area, but scaled in terms of magnetic field strength measurements rather than units of magnetic flux. Repeating the experiment on the four cardinal headings, and applying an inverse heading rotation for each direction gives bias information for each magnetometer axis.

Monitoring the norm of the measured vector shows total field noise, and provides a basis for calibrating the magnetometer into units of magnetic flux. A basis for calibration is now available by comparing a mean norm to published field strength data[1]. However, since the filter can be written in terms of raw sensor values, there is no need to compute such a calibration unless the individual sensor axes are shown to be in disagreement. Details of the process are contained in Appendix C.

2.1.4 User Interface

Ground station hardware includes a laptop computer which communicates with the aircraft through a communications box containing a 900 MHz radio modem. The communications box, also interfaces with a radio control transmitter by a trainer cable, which can send overriding commands to the autopilot.

---

[1] Field strength data available from the National Oceanic and Atmospheric Administration (NOAA) at http://www.ngdc.noaa.gov/seg/geomag/magfield.shtml

The Virtual Cockpit software records telemetry packets from the aircraft, displaying information such as pitch, roll and other vital information on a heads-up display, and displays position information in a map window. The Virtual Cockpit also contains a framework to view and change many autopilot variables, allowing in-flight tuning of estimation and control parameters.

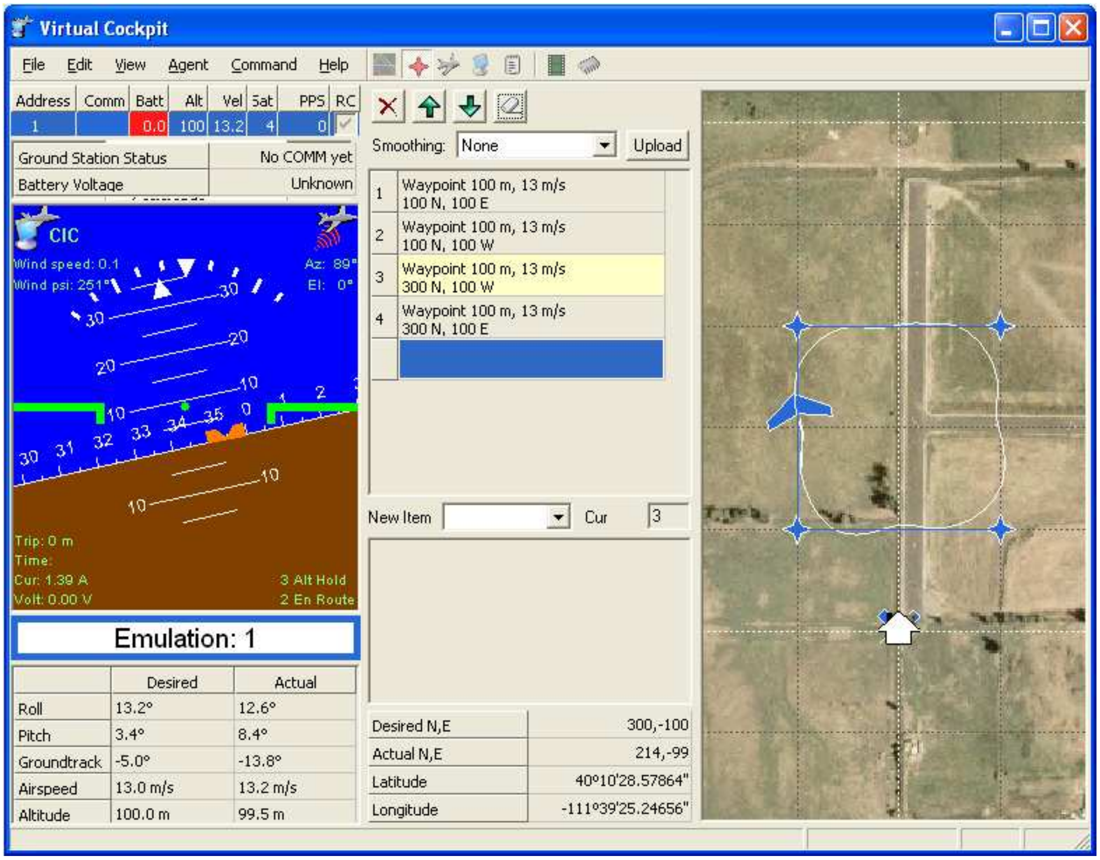

Address	Comm	Batt	Alt	Vel	Sat	PPS	RC
1		0.0	100	13.2	4	0	✓

Ground Station Status	No COMM yet
Battery Voltage	Unknown

Wind speed: 0.1
Wind psi: 251°
Az: 89°
El: 0°
Trip: 0 m
Time:
Cur: 1.39 A
Volt: 0.00 V
3 Alt Hold
2 En Route

Emulation: 1

	Desired	Actual
Roll	13.2°	12.6°
Pitch	3.4°	8.4°
Groundtrack	-5.0°	-13.8°
Airspeed	13.0 m/s	13.2 m/s
Altitude	100.0 m	99.5 m

Smoothing: None

1	Waypoint 100 m, 13 m/s 100 N, 100 E
2	Waypoint 100 m, 13 m/s 100 N, 100 W
3	Waypoint 100 m, 13 m/s 300 N, 100 W
4	Waypoint 100 m, 13 m/s 300 N, 100 E

New Item
Cur 3

Desired N,E	300,-100
Actual N,E	214,-99
Latitude	40°10'28.57864"
Longitude	-111°39'25.24656"

Figure 2.6: Virtual Cockpit MAV Interface

2.1.5 Simulation Environment

In the MAGICC Lab, preliminary algorithm testing takes place in the Aviones flight simulator, which includes an autopilot emulation framework that allows code written for the Rabbit microprocessor to be compiled as a dynamically linked library.

In this way, code written for the embedded processor can be tested in a software environment before committing it to the air on a hardware platform. This code is called from the Aviones[2] simulator and communicates with the Virtual Cockpit over a TCP/IP socket as though the simulated aircraft were a physical aircraft communicating via radio. This arrangement allows for rapid development, testing and initial tuning of estimation and control algorithms in the simulator prior to flight testing. The Aviones simulator allows alteration of aircraft parameters such as aircraft lift and drag coefficients, as well as environmental factors such as gravitational fields and wind speed and direction.

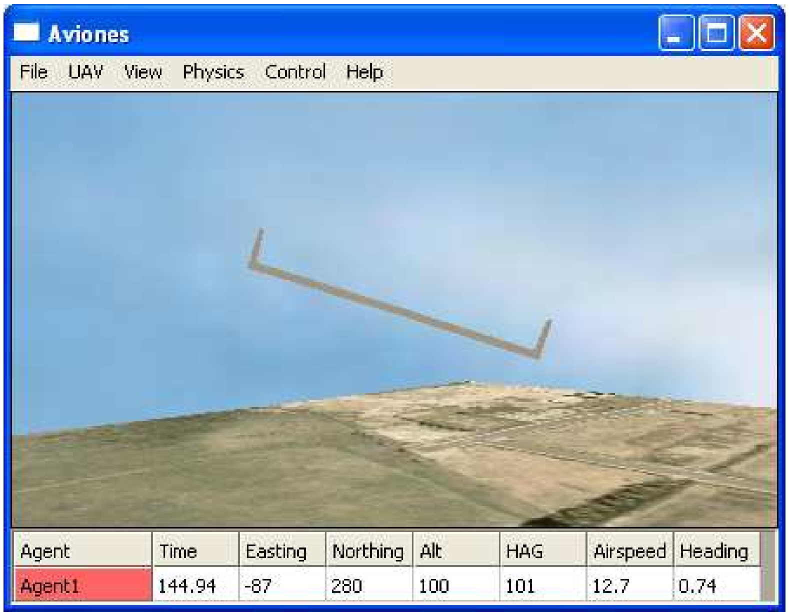

Agent	Time	Easting	Northing	Alt	HAG	Airspeed	Heading
Agent1	144.94	-87	280	100	101	12.7	0.74

Figure 2.7: The Aviones MAV Simulator

2.2 Variables, Reference Frames and Notation

In this discussion, the MAV body coordinate frame is a right-handed system centered at the vehicle center of mass. The x-axis points out the nose, the y-axis points out the right wing, and the z-axis points out the belly. The airspeed of the airplane is expressed in terms of velocity components on each of these axes, or alternatively, as the magnitude of the velocity components in conjunction with angle of attack and side slip. See table Table 2.1.

---

[2] Available from SourceForge: http://sourceforge.net/projects/aviones

The inertial coordinate frame is centered at a home base, with the x-axis pointed north, the y-axis pointed east, and the z-axis pointed into the earth. An intermediate frame, called the vehicle frame, is collocated with the body frame and is oriented to the inertial frame. Pitch and roll angles relate the MAV body frame to the vehicle frame. The complete description of change of orientation from vehicle to body frame includes the heading angle, but that will be treated separately from this discussion, as it is easily separated into an independent estimation and control problem. Refer to Table 2.1 for a list of the state variables and other pertinent variables used in this discussion.

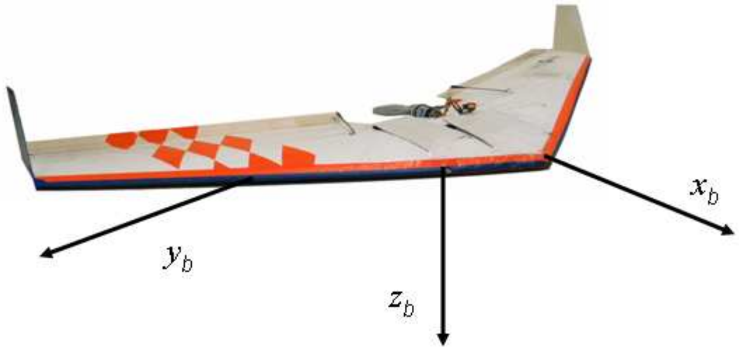

Figure 2.8: MAV Body Frame Coordinate Axes

2.3 System Model

The nonlinear equations of motion used here are kinematic in nature, presuming the availability of angular rate and airspeed information, as noted by their inclusion in the input vector $\mathbf{u}$. The vector $\mathbf{x}$ contains the state variables which will be estimated in this treatment. The vector $\mathbf{y}$ shows the variables which are measured

Table 2.1: Standard MAV State Variables

P_N	inertial North position of MAV
P_E	inertial East position of MAV
h	inertial MAV altitude
u	airspeed along body x-axis
v	airspeed along body y-axis
w	airspeed along body z-axis
ϕ	roll angle
θ	pitch angle
ψ	heading
p	angular rate about body x-axis
q	angular rate about body y-axis
r	angular rate about body z-axis

Table 2.2: Alternate State Variables

V_{air}	total airspeed
α	angle of attack
β	sideslip angle

Table 2.3: Variables Representing Sensor Measurements

a_x	x accelerometer reading
a_y	y accelerometer reading
a_z	z accelerometer reading
B_x	x-axis magnetometer reading
B_y	y-axis magnetometer reading
B_z	z-axis magnetometer reading
GPS_N	GPS North measurement
GPS_E	GPS East measurement

by the sensors. MAV system states, inputs and outputs are

$$\mathbf{x} = [\ \phi\ \ \theta\ \ \psi\ \ P_n\ \ P_e\ \ W_n\ \ W_e\ ]^T, \tag{2.1}$$

$$\mathbf{u} = [\ p\ \ q\ \ r\ \ V_{air}\ ]^T \tag{2.2}$$

and

$$\mathbf{y} = [\ a_x\ \ a_y\ \ a_z\ \ B_x\ \ B_y\ \ B_z\ \ P_N\ \ P_E\ ]^T. \tag{2.3}$$

We use the convention that wind comes from the direction indicated, or in other words, facing the direction of the wind vector results in facing upwind. The relationships between the change in states and the system inputs are

$$\dot{\mathbf{x}} = \begin{bmatrix} \dot{\phi} \\ \dot{\theta} \\ \dot{\psi} \\ \dot{P_N} \\ \dot{P_E} \\ \dot{W_N} \\ \dot{W_E} \end{bmatrix} = \begin{bmatrix} p + q\sin\phi\tan\theta + r\cos\phi\tan\theta \\ q\cos\phi + r\sin\phi \\ q\frac{\sin\phi}{\cos\theta} + r\frac{\cos\phi}{\cos\theta} \\ V_{air}\cos\psi - W_N \\ V_{air}\sin\psi - W_E \\ 0 \\ 0 \end{bmatrix}, \tag{2.4}$$

which will be considered in smaller groups in approaching the estimation problem.

Measurements available on the MAV platform are related to the states and inputs. For the state equations above, body frame accelerations, a_x, a_y and a_z may be calculated as system outputs. Newton's laws can be used to express body frame accelerations in terms of gravity, angular rates and axial accelerations. For the accelerometer measurements, we may expect

$$\begin{bmatrix} a_x \\ a_y \\ a_z \end{bmatrix} = \begin{bmatrix} \frac{\dot{u}+qw-rv}{g} & + & \sin\theta \\ \frac{\dot{v}+ru-pw}{g} & - & \cos\theta\sin\phi \\ \frac{\dot{w}+pv-qu}{g} & - & \cos\theta\cos\phi \end{bmatrix} \tag{2.5}$$

in gravity units.

Magnetometer readings can be anticipated as the earth's magnetic field vector rotated from the inertial to the body frame using the transformation

$$\begin{bmatrix} B_x \\ B_y \\ B_z \end{bmatrix} = \begin{bmatrix} \cos\theta\cos\psi & \cos\theta\sin\psi & -\sin\theta \\ (\sin\phi\sin\theta\cos\psi - \cos\phi\sin\psi) & (\sin\phi\sin\theta\sin\psi + \cos\phi\cos\psi) & \sin\phi\cos\theta \\ (\cos\phi\sin\theta\cos\psi + \sin\phi\sin\psi) & (\cos\phi\sin\theta\sin\psi - \sin\phi\cos\psi) & \cos\phi\cos\theta \end{bmatrix} \begin{bmatrix} B_{0x} \\ B_{0y} \\ B_{0z} \end{bmatrix} \tag{2.6}$$

where B_{0x}, B_{0y} and B_{0z} denote components of the earth's magnetic field as measured in the inertial frame.

The expected value of GPS measurement corresponds to the estimated location of the vehicle, expressed as

$$\begin{bmatrix} GPS_N \\ GPS_E \end{bmatrix} = \begin{bmatrix} P_N \\ P_E \end{bmatrix}, \tag{2.7}$$

which is updated between the relatively infrequent GPS measurements. The global coordinates are first converted to a local reference frame and are expressed in meters east and north of a home position.

2.4 Review of the Extended Kalman Filter

The Kalman filter was introduced by R.E. Kalman in 1960 [11] as a stochastically-based optimal linear observer. The extended Kalman filter is similar to the linear Kalman filter in that it uses an estimate of statistical variance to calculate the weight of sensor corrections to state estimates. We will be dealing with nonlinear systems which have the form

$$\begin{aligned} \dot{\mathbf{x}} &= \mathbf{f}(\mathbf{x}, \mathbf{u}) + \mathbf{w}(t) && (2.8) \\ \mathbf{z}_k &= \mathbf{h}(\mathbf{x}(t_k), \mathbf{u}) + \mathbf{v}_k. && (2.9) \end{aligned}$$

In the case where system dynamics are described using such a continuous nonlinear model, the vector $\mathbf{w}(t)$ is used to account for disturbances and unmodeled dynamics. At the discreet measurements, we may expect that readings include some noise, represented by $\mathbf{v}_k$. It is assumed that the vectors $\mathbf{w}(t)$ and $\mathbf{v}_k$ are represent random variables with zero mean, and covariances Q and R respectively.

Between sensor measurements, the nonlinear model is used to update the estimates. The covariance matrix $\mathbf{P}$ contains confidence information for the state estimates and is updated using a linearization of the state equations. By propagating the kinematic model, we make intelligent predictions of what sensors related to the states of interest will be at the next measurement. Because the relationship of the states to the measurements is also nonlinear, another linearization is required to calculate sensor update gains.

While no proof has been discovered to show that the extended Kalman filter is optimal, experience has shown that it is very effective. Inasmuch as there are several variations on state space and Kalman filter notation, the EKF notation to be used throughout this work is provided here.

2.4.1 Extended Kalman Filter Time Update

In the extended Kalman filter, state estimates are propagated by numerically integrating the nonlinear state equations. In the update, we must account for

$$\dot{\hat{\mathbf{x}}} = \mathbf{f}(\hat{\mathbf{x}}, \mathbf{u}), \qquad (2.10)$$

$$\mathbf{A}(\hat{\mathbf{x}}, \mathbf{u}) = \left.\frac{\partial \mathbf{f}(\mathbf{x}, \mathbf{u})}{\partial \mathbf{x}}\right|_{\mathbf{x}=\hat{\mathbf{x}}} \qquad (2.11)$$

Table 2.4: Variables Used in the Extended Kalman Filter

$\hat{\mathbf{x}}$	Estimated state vector
$\mathbf{f}(\mathbf{x}, \mathbf{u})$	Nonlinear state update
$\mathbf{h}(\mathbf{x}, \mathbf{u})$	Nonlinear model outputs
$\mathbf{z}$	Sensor measurements
$\mathbf{A}$	Linearized state update matrix
$\mathbf{C}$	Linearized model output matrix
$\mathbf{P}$	State covariance matrix
$\mathbf{L}$	Sensor update gain matrix
$\mathbf{Q}$	Process noise covariance matrix
$\mathbf{R}$	Sensor noise covariance matrix

and

$$\dot{\mathbf{P}} = \mathbf{A}(\hat{\mathbf{x}}, \mathbf{u})\mathbf{P} + \mathbf{P}\mathbf{A}(\hat{\mathbf{x}}, \mathbf{u})^T + \mathbf{Q}. \tag{2.12}$$

Growth of uncertainty in the estimated states is represented in equation Equation 2.12, which makes use of the linearized state matrix from Equation 2.11.

2.4.2 Extended Kalman Filter Measurement Update

For the update of state estimates when a measurement is received, we have

$$\mathbf{C}(\mathbf{x}, \mathbf{u}) = \frac{\partial \mathbf{h}(\mathbf{x}^{-}, \mathbf{u})}{\partial \mathbf{x}}, \tag{2.13}$$

$$\mathbf{L} = \mathbf{P}^{-}\mathbf{C}^{\mathbf{T}}(\mathbf{R} + \mathbf{C}(\hat{\mathbf{x}}, \mathbf{u})\mathbf{P}^{-}\mathbf{C}(\hat{\mathbf{x}}, \mathbf{u})^{\mathbf{T}})^{-1}, \tag{2.14}$$

$$\mathbf{P} = (\mathbf{I} - \mathbf{L}\mathbf{C}(\hat{\mathbf{x}}, \mathbf{u}))\mathbf{P}^{-} \tag{2.15}$$

and

$$\hat{\mathbf{x}} = \hat{\mathbf{x}}^{-} + \mathbf{L}(\mathbf{z} - \mathbf{h}(\hat{\mathbf{x}}^{-}, \mathbf{u})). \tag{2.16}$$

Correction of state estimates from sensor data takes place in Equation 2.16 using gains calculated in Equation 2.14. Superscript minus indicates *a priori* values.

The use of the extended Kalman filter requires additional caution over the linear Kalman filter, particularly when estimating angles such as roll, pitch and heading. In these cases, one must consider the meaning of a large covariance value, since in the cases of angles, there is a limitation on incorrectness, that is an angle value can be no more incorrect than π before it begins to be correct again. For this reason, it is wise to limit the variance to reflect the improbability of an error greater than π. This becomes important during the calculation of sensor correction gains, the danger being that nonsensical gains can be chosen for large variances. For example, a large variance may lead to a sensor correction greater than reasonably justifiable using the linear approximation. Simulation results for the heading estimate provide illustration for further discussion of this topic in Section 3.2.

2.4.3 Simplification: Independent Sensor Updates

In the event that noise on each sensor axis is uncorrelated, there are no nonzero off-diagonal terms in the matrix $\mathbf{R}$. In implementation, matrix $\mathbf{C}$ is divided into a set of row vectors, for example, for a three-axis measurement $\mathbf{C} = [\mathbf{c}_x \ \mathbf{c}_y \ \mathbf{c}_z]^T$. Each of the rows in the Kalman gain matrix $\mathbf{L}$ is calculated independently as shown in Equation 2.17. This approach greatly reduces computation by eliminating a costly matrix inversion operation, replacing it instead with

$$\begin{aligned} \mathbf{l}_x &= \frac{\mathbf{P}\mathbf{c}_x^T}{R_x + \mathbf{c}_x\mathbf{P}\mathbf{c}_x^T}, \\ \mathbf{l}_y &= \frac{\mathbf{P}\mathbf{c}_y^T}{R_y + \mathbf{c}_y\mathbf{P}\mathbf{c}_y^T} \end{aligned} \tag{2.17}$$

and

$$\mathbf{l}_z = \frac{\mathbf{P}\mathbf{c}_z^T}{R_z + \mathbf{c}_z\mathbf{P}\mathbf{c}_z^T},$$

which requires only a single division operation for each sensor axis. Since sensor measurement corrections can be made independently, it is not necessary to take all of the sensor measurements at the same time. Therefore each measurement can be made independently, and the appropriate adjustment to the state estimate made incrementally rather than in batches.

2.5 Cascaded Filter Structure

Estimation of the states of interest, shown in ?? is accomplished using a three-stage state-estimation scheme. The estimates of pitch and roll calculated in the first stage are used as inputs to the second stage filter to calculate vehicle heading using rate gyro updates and magnetometer outputs. A final stage can use this information, along with GPS to compute the location and wind states. The cascaded structure is illustrated in Figure 2.9. The mechanics of each stage are described in detail below.

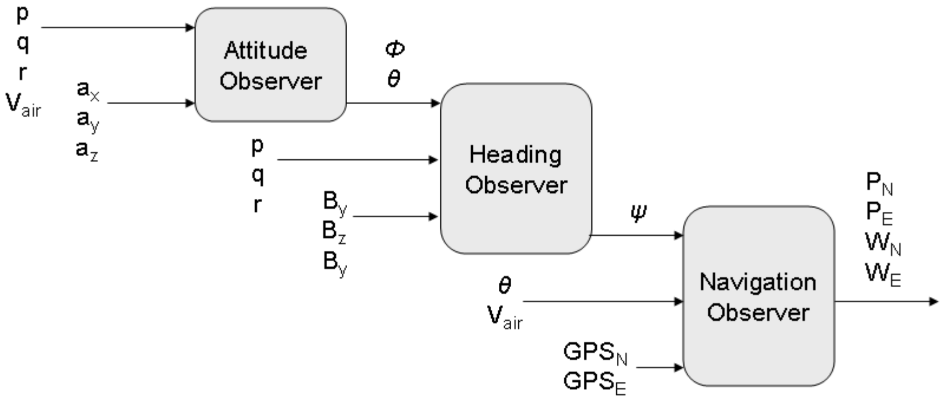
p
q
r
V_{air}
a_x
a_y
a_z
Attitude Observer
Φ
θ
p
q
r
B_y
B_z
B_y
Heading Observer
ψ
θ
V_{air}
GPS_N
GPS_E
Navigation Observer
P_N
P_E
W_N
W_E

Figure 2.9: Three-Stage State-Estimation Scheme

2.6 Stage 1: Pitch and Roll Estimation

While the observer described in this section is more computationally complex than the original algorithm, it promises to open the operational envelope of miniature air vehicles, (MAV's) and improve the accuracy of the attitude estimates by reducing errors which occur during sustained turns. Although integral control allows the vehicle to track desired courses over the ground and hold altitudes in spite of bias errors in the pitch and roll estimate, this reduction in error is valuable for resolving sensor data to real World coordinates.

For this stage we have

$$\mathbf{x} = \begin{bmatrix} \phi \\ \theta \end{bmatrix}, \qquad \mathbf{u} = \begin{bmatrix} p \\ q \\ r \\ V_{air} \end{bmatrix} \qquad \text{and} \qquad \mathbf{z} = \begin{bmatrix} a_x \\ a_y \\ a_z \end{bmatrix}$$

for states, inputs and outputs. The state variables (denoted by the vector $\mathbf{x}$) to be estimated in this stage are pitch and roll (ϕ and θ). Angular rates and airspeed make up the input vector $\mathbf{u}$ and body frame accelerations compose the system outputs ($\mathbf{z}$) for this stage.

For the kinematic portion of this model, we have

$$\begin{bmatrix} \dot{\phi} \\ \dot{\theta} \end{bmatrix} = \mathbf{f}(\mathbf{x}, \mathbf{u}) = \begin{bmatrix} p & + & q \sin\phi \tan\theta & + & r \cos\phi \tan\theta \\ & & q \cos\phi & + & r \sin\phi \end{bmatrix}, \tag{2.18}$$

which comes directly from Section 2.3. The sensor output model for this stage,

$$\begin{bmatrix} a_x \\ a_y \\ a_z \end{bmatrix} = \mathbf{h}(\mathbf{x}, \mathbf{u}) = \begin{bmatrix} \frac{V_{air} q \sin\theta}{g} & + & \sin\theta \\ \frac{V_{air}(r \cos\theta - p \sin\theta)}{g} & - & \cos\theta \sin\phi \\ \frac{-V_{air} q \cos\theta}{g} & - & \cos\theta \cos\phi \end{bmatrix}, \tag{2.19}$$

is modified from the model in Section 2.3, containing some assumptions explained Section 2.6.2.

2.6.1 Stage 1: Time Update

The Stage 1 Kalman filter time update includes propagating the pitch and roll estimates with angular rate information from the rate gyros. The relationship between body frame rotations and changes in roll, pitch and heading are nonlinear. Letting angular rates and airspeed p, q, r and V_{air} be inputs, for the the update of the states we have

$$\begin{bmatrix} \dot{\hat{\phi}} \\ \dot{\hat{\theta}} \end{bmatrix} = \mathbf{f}(\hat{\mathbf{x}}, \mathbf{u}) = \begin{bmatrix} p & + & q\sin\hat{\phi}\tan\hat{\theta} & + & r\cos\hat{\phi}\tan\hat{\theta} \\ & & q\cos\hat{\phi} & + & r\sin\hat{\phi} \end{bmatrix}, \tag{2.20}$$

which is unmodified from Equation 2.4, because all angular rate information is available. We simply substitute the current estimates for pitch and roll into Equation 2.20 only that the update is calculated using the current estimates.

Evaluation of the linearized state equations and update of the filter covariance matrix follows in execution. Evaluating the linearization about the current estimate gives

$$A(\hat{\mathbf{x}}, \mathbf{u}) = \left.\frac{\partial \mathbf{f}(\mathbf{x}, \mathbf{u})}{\partial \mathbf{x}}\right|_{\mathbf{x}=\hat{\mathbf{x}}} = \begin{bmatrix} q\cos\hat{\phi}\tan\hat{\theta} - r\sin\hat{\phi}\tan\hat{\theta} & \frac{q\sin\hat{\phi} - r\cos\hat{\phi}}{\cos^2\hat{\theta}} \\ -q\sin\hat{\phi} + r\cos\hat{\phi} & 0 \end{bmatrix}. \tag{2.21}$$

These time update steps are outlined in Equation 2.10 through Equation 2.12, which makes use of Equation 2.20 and Equation 2.21.

2.6.2 Stage 1: Measurement Update

All the information necessary to propagate the state vector using Equation 2.4 is available as a current estimate or input, so it is used as shown in Equation 2.20. Ideally, Equation 2.5 would be used to model sensor outputs, but unlike Equation 2.4, not all of the information in Equation 2.5 available. In particular, airspeed is not resolved into components. To make the most accurate prediction of the sensor measurements with the information available, a number of simplifying assumptions are made. We begin with

$$\begin{bmatrix} u \\ v \\ w \end{bmatrix} = V_{air} \begin{bmatrix} \cos\alpha\cos\beta \\ \sin\beta \\ \sin\alpha\cos\beta \end{bmatrix}, \tag{2.22}$$

an alternative expression of the body-frame component velocities.

Component velocity information absent from Equation 2.5 can be approximated for level flight using pitch angle information. Pitch, θ, and angle of attack, α are related by

$$\theta = \alpha + \gamma. \tag{2.23}$$

This relationship is illustrated Figure 2.10. If the vehicle is not climbing or descending, that is , γ is equal to zero, then we assume the pitch angle is equal to the angle of attack. Further, we may assume negligible side slip in an aircraft with a fixed rudder and reasonable aerodynamic characteristics. Under these assumptions,

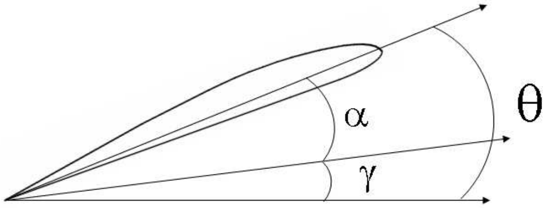

Figure 2.10: Relationship of Pitch, Angle of Attack and Flight Path Angles

we replace Equation 2.22 with

$$\begin{bmatrix} u \\ v \\ w \end{bmatrix} \approx V_{air} \begin{bmatrix} \cos\theta \\ 0 \\ \sin\theta \end{bmatrix}. \tag{2.24}$$

We assume also that the rate of change in component velocities are small, that is,

$$\begin{bmatrix} \dot{u} \\ \dot{v} \\ \dot{w} \end{bmatrix} \approx \mathbf{0}. \tag{2.25}$$

Gathering the assumptions from Equation 2.24 and Equation 2.25, Equation 2.5 simplifies to give us

$$\begin{bmatrix} \hat{a}_x \\ \hat{a}_y \\ \hat{a}_z \end{bmatrix} = \mathbf{h}(\hat{\mathbf{x}}, \mathbf{u}) = \begin{bmatrix} \frac{V_{air} q \sin\hat{\theta}}{g} & + & \sin\hat{\theta} \\ \frac{V_{air}(r\cos\hat{\theta} - p\sin\hat{\theta})}{g} & - & \cos\hat{\theta}\sin\hat{\phi} \\ \frac{-V_{air} q \cos\hat{\theta}}{g} & - & \cos\hat{\theta}\cos\hat{\phi} \end{bmatrix}, \tag{2.26}$$

which will be used as the model sensor output equations. For the gain calculation and variance update, we again linearize and evaluate at the current estimates to get

$$\mathbf{C}(\hat{\mathbf{x}}, \mathbf{u}) = \left.\frac{\partial \mathbf{h}(\mathbf{x}, \mathbf{u})}{\partial \mathbf{x}}\right|_{\mathbf{x}=\hat{\mathbf{x}}} = \begin{bmatrix} 0 & \frac{qV_{air}}{g}\cos\hat{\theta} + \cos\hat{\theta} \\ -\cos\hat{\theta}\cos\hat{\phi} & \frac{-rV_{air}}{g}\sin\hat{\theta} - \frac{pV_{air}}{g}\cos\hat{\theta} + \sin\hat{\theta}\sin\hat{\phi} \\ \cos\hat{\theta}\sin\hat{\phi} & (\frac{qV_{air}}{g}\sin\hat{\theta} + \cos\hat{\phi})\sin\hat{\theta} \end{bmatrix}, \tag{2.27}$$

which is used as shown in section 2.4.2 to calculate gains and update variance.

2.6.3 Other Stage 1 Tuning Considerations

The sensor noise matrix **R** used in Equation 2.14 or Equation 2.17 directly affects the trust placed on the sensor during sensor measurement updates. Normally, this parameter would account only for noise on the sensor, but because we are using noisy sensor measurements for p, q and r, the predictions for the accelerometer measurements are also noise laden. These noisy measurements enter the calculation of the output in the form of a vector cross product with component airspeeds u, v and w. For normal flight, u is much greater than w, and v is practically insignificant, resulting in a considerably varied affect of the gyro noise on each accelerometer axis, forcing us to consider the noise estimate **R** for each accelerometer individually.

Another consideration is the affect of the assumption resulting in Equation 2.22. This assumption is not damaging in any unaccelerated flight condition, even steady climbs and descents, since u, v and w are always multiplied by an angular rate. In cases where the assumption is violated and there is an angular rate, there may be a large, unmodeled acceleration measured by the sensor. The most common occurrence of this situation is during a sharp rotation at the beginning or end of a climb or descent. To deal with this situation, we can add a penalty to the noise estimate of the x-axis, proportional to the pitch rate, q, which is associated with the unmodeled dynamics. Continuing to model the other accelerometer axes with constant noise, we have

$$\begin{bmatrix} Rx \\ Ry \\ Rz \end{bmatrix} = \begin{bmatrix} Rx_0 + \tau q \\ Ry_0 \\ Rz_0 \end{bmatrix}. \tag{2.28}$$

This penalty significantly attenuates the x-axis accelerometer's effect on state estimate during maneuvers with high pitch rates, allowing the observer to rely mainly on the model update during the maneuver. The resulting accelerometer noise model uses τ as a tuning parameter which is increased to reduce the Kalman gain on the sensor during times when the sensor measurement may be unreliable. This is similar to the gain scheduling implemented for the Variable Gain Observer, described in Appendix A, with the important distinction that in this case, gain scheduling is done on a per axis basis. Instead of penalizing all accelerometer measurements, only the suspect information will be attenuated, allowing the other sensor axes to update the state. The unmodeled dynamics affecting other axes are not significant in normal flight modes, so it is not necessary to attenuate other accelerometer measurement updates. See Algorithm 1 for a summary of the first stage attitude observer.

2.7 Stage 2: Heading Estimation

A magnetometer updated heading estimate is useful for cases where a wind induced crab angle needs to be accounted for when interpreting data from cameras or other sensors. Magnetometer based headings are also helpful in windy situations

Algorithm 1 Stage 1: Roll and Pitch Estimation

```
Obtain $V_{air}$ $p$, $q$, $r$, $a_x$, $a_y$, and $a_z$ from sensors.
Update the state estimate using the kinematic update (Equation 2.20).
Compute the linearized state update matrix (Equation 2.21).
Propagate the covariance matrix (Equation 2.12).
for each accelerometer axis do
    Calculate appropriate sensor output using current state estimate (Equation 2.26).
    Calculate linearized output equations (Equation 2.27).
    Calculate sensor noise penalty (Equation 2.28).
    Calculate Kalman gain (Equation 2.17).
    Update state estimate (Equation 2.16).
    Update covariance matrix (Equation 2.15).
end for
```

where headings approximated from GPS become inaccurate because the groundspeed becomes small. Such situations have led to vehicles flying uncontrollably downwind because in the upwind situation they cannot hold a heading estimate sufficient to continue upwind.

Integration of rate gyros can be used to update heading estimates in the same manner as in the attitude estimate, but additional information is needed to remove the inevitable drift. In this case, the additional information comes from the earth's magnetic field, as read by the magnetometer. One approach to retrieving heading from the magnetometer consists of reading the magnetometer axes and calculating the magnetic heading using trigonometry from the field strength on each axis. Appropriately summing declination data gives true heading. While it is convenient to think of an instrument which could simply be calibrated to give the heading angle, calibrating and interpreting magnetometer data using this approach introduces significant problems which affect the measurement accuracy.

The Earth's magnetic field is not generally aligned with the north pole, but varies in relative direction to true north all over the World. The coordinates of the test facility are approximately 40.2 degrees north, 111.5 degrees west. At this location, the magnetic field is pointed to the east of true north and toward the center of the earth from horizontal. The declination, also known as deviation, is approximately 14 degrees east of north. The inclination, sometimes called dip, of the earth's magnetic field is roughly 60 degrees, making the z-component of the field twice as strong as the north component. The magnetometer is therefore extremely sensitive to variations in pitch and roll while measuring heading. No compass is immune from these problems induced by the strong z-component of the magnetic field, commonly referred to as dip errors. Pilots using a magnetic compass for navigation are instructed to use it only when in level, unaccelerated flight, since the z-component will affect the reading of the instrument when it is not level.

Instead of interpreting the heading from the magnetometer at each time step and filtering that data, we prefer to deal directly with the field strength data for each axis. Beginning with the autopilot estimates of pitch and roll, which are determined using rate gyros and accelerometer measurements, and a knowledge of the local magnetic field, a current heading estimate can be used to estimate the three-dimensional body-frame measurement of the magnetic field. This information is compared directly to information from the sensor to update the heading estimate.

In this scheme, the heading estimation is a single-state extended Kalman filter. The states, inputs, and model outputs are

$$\mathbf{x} = \psi \qquad \mathbf{u} = \begin{bmatrix} \phi \\ \theta \\ q \\ r \end{bmatrix} \qquad \mathbf{z} = \begin{bmatrix} B_x \\ B_y \\ B_z \end{bmatrix}.$$

The kinematic model equation for this estimator include the kinematic relationship between body frame angular rates and heading, or

$$\dot{\psi} = f(\mathbf{x}, \mathbf{u}) = q\frac{\sin\phi}{\cos\theta} + r\frac{\cos\phi}{\cos\theta}. \tag{2.29}$$

The sensor model is simply a rotational transformation of the earth-frame magnetic field to the body-frame sensor, given by

$$\begin{bmatrix} B_x \\ B_y \\ B_z \end{bmatrix} = \mathbf{h}(\mathbf{x}, \mathbf{u}) =$$
$$\begin{bmatrix} \cos\theta\cos\psi & \cos\theta\sin\psi & -\sin\theta \\ (\sin\phi\sin\theta\cos\psi - \cos\phi\sin\psi) & (\sin\phi\sin\theta\sin\psi + \cos\phi\cos\psi) & \sin\phi\cos\theta \\ (\cos\phi\sin\theta\cos\psi + \sin\phi\sin\psi) & (\cos\phi\sin\theta\sin\psi - \sin\phi\cos\psi) & \cos\phi\cos\theta \end{bmatrix} \begin{bmatrix} B_{0x} \\ B_{0y} \\ B_{0z} \end{bmatrix}. \tag{2.30}$$

2.7.1 Stage 2: Time Update

Between magnetometer measurements, the estimate is updated using rate gyros by the expression

$$\dot{\hat{\psi}} = \mathbf{f}(\hat{\mathbf{x}}, \mathbf{u}) = q\frac{\sin\phi}{\cos\theta} + r\frac{\cos\phi}{\cos\theta}. \tag{2.31}$$

Because the linearization of this single state update, evaluated about the current estimate results in

$$A(\hat{\mathbf{x}}, \mathbf{u}) = \left.\frac{\partial \mathbf{f}(\mathbf{x}, \mathbf{u})}{\partial x}\right|_{\mathbf{x}=\hat{\mathbf{x}}} = 0, \tag{2.32}$$

the growth in the estimate variance will by the model noise only.

2.7.2 Stage 2: Measurement Update

The output equations for the heading estimator predict magnetometer measurements, again, given by

$$\begin{bmatrix} \hat{B}_x \\ \hat{B}_y \\ \hat{B}_z \end{bmatrix} = \mathbf{h}(\hat{\mathbf{x}}, \mathbf{u}) =$$
$$\begin{bmatrix} \cos\theta\cos\hat{\psi} & \cos\theta\sin\hat{\psi} & -\sin\theta \\ (\sin\phi\sin\theta\cos\hat{\psi} - \cos\phi\sin\hat{\psi}) & (\sin\phi\sin\theta\sin\hat{\psi} + \cos\phi\cos\hat{\psi}) & \sin\phi\cos\theta \\ (\cos\phi\sin\theta\cos\hat{\psi} + \sin\phi\sin\hat{\psi}) & (\cos\phi\sin\theta\sin\hat{\psi} - \sin\phi\cos\hat{\psi}) & \cos\phi\cos\theta \end{bmatrix} \begin{bmatrix} B_{0x} \\ B_{0y} \\ B_{0z} \end{bmatrix}. \tag{2.33}$$

Linearizing and evaluating at the current estimate gives us

$$C(\hat{\mathbf{x}},\mathbf{u}) = \left.\frac{\partial \mathbf{h}(\mathbf{x},\mathbf{u})}{\partial \mathbf{x}}\right|_{\mathbf{x}=\hat{\mathbf{x}}} =$$

$$\begin{bmatrix} -\cos\theta\sin\hat{\psi}B_{0x} & + & \cos\theta\cos\hat{\psi}B_{0y} \\ (-\sin\phi\sin\theta\sin\hat{\psi}-\cos\phi\cos\hat{\psi})B_{0x} & + & (\sin\phi\sin\theta\sin\hat{\psi}+\cos\phi\sin\hat{\psi})B_{0y} \\ (-\cos\phi\sin\theta\sin\hat{\psi}+\sin\phi\cos\hat{\psi})B_{0x} & + & (\sin\phi\sin\theta\cos\hat{\psi}-\cos\phi\sin\hat{\psi})B_{0y} \end{bmatrix}. \tag{2.34}$$

These expressions are used in updating the heading as shown in section Section 2.4.2. Note that the z-component of the magnetic field drops predictably out of the linearization.

Data from the calibration runs serve as the basis for $\mathbf{B_0}$ and also serves as a baseline for the noise characteristics for the sensor, which will be used in tuning the state estimation filter.

2.7.3 Adaptation for Two-Axis Magnetometers

Because this EKF implementation predicts the measurement on each magnetometer axis using the roll and pitch angles and updates the heading using each axis independently, any axis can be ignored as long as the linearization allows the use of the remaining axis. Depending on the heading, the magnetometer is effectively used a single axis at a time, and the z-axis is suitable for dropping most of the time. The only difference in implementation is the removal of the last row from Equation 2.33 and Equation 2.34.

2.8 Stage 3: Position and Wind Estimation

The third and final stage of this state estimation scheme keeps an estimate of vehicle location. With the heading obtained in Stage 2 and measured airspeed, the location of the airplane is predicted using a simple kinematic model and checked against GPS measurements. Differences in the prediction and measurement of position are applied to the position estimate and update an estimate of the wind, which has no dynamics of its own. The wind estimate is then used in updating the predicted

Algorithm 2 Stage 2: Heading Estimation

```
Obtain $q$ and $r$ from sensors and $\phi$ and $\theta$ from stage 1.
Update the state estimate using the kinematic update (Equation 2.31).
Compute the linearized state update matrix (Equation 2.32).
Propagate the covariance variable (Equation 2.12).
if new magnetometer measurement available then
    for each magnetometer axis do
        Calculate sensor output using current heading estimate (Equation 2.33).
        Calculate linearized output equations (Equation 2.34).
        Calculate Kalman gain (Equation 2.17).
        Update state estimate (Equation 2.16).
        Update covariance variable (Equation 2.15).
    end for
end if
```

position of the MAV. Inputs to this stage are heading and airspeed, and the system outputs are north and east position.

The EKF based navigation observer shows promise in being able to update wind estimates without necessitating the MAV to make turns. The wind estimates can also update more quickly or can filter updates as lightly or heavily as the GPS update will allow. This algorithm also shows promise for navigating in GPS denied conditions. Third stage states, inputs and outputs are

$$\mathbf{x} = \begin{bmatrix} P_N \\ P_E \\ W_N \\ W_E \end{bmatrix} \qquad \mathbf{u} = \begin{bmatrix} \psi \\ \theta \\ V_{air} \end{bmatrix} \qquad \text{and} \qquad \mathbf{z} = \begin{bmatrix} GPS_N \\ GPS_E \end{bmatrix}.$$

The model for the third stage,

$$\begin{bmatrix} \dot{P}_N \\ \dot{P}_E \\ \dot{W}_N \\ \dot{W}_E \end{bmatrix} = \mathbf{f}(\mathbf{x}, \mathbf{u}) = \begin{bmatrix} V_{air} \cos\psi \cos\theta - W_N \\ V_{air} \sin\psi \cos\theta - W_E \\ 0 \\ 0 \end{bmatrix}, \tag{2.35}$$

is a simple kinematic relationship for position and speed in two dimensions. The speed is scaled by the cosine of pitch. The model outputs,

$$\mathbf{h}(\mathbf{x},\mathbf{u}) = \begin{bmatrix} P_N \\ P_E \end{bmatrix}, \tag{2.36}$$

are trivial, since GPS simply provides an alternate measure of selected the states.

2.8.1 Stage 3: Time Update

The third stage kinematic update uses the current wind estimate in the update of position, giving us

$$\begin{bmatrix} \dot{\hat{P}}_N \\ \dot{\hat{P}}_E \\ \dot{\hat{W}}_N \\ \dot{\hat{W}}_E \end{bmatrix} = \mathbf{f}(\hat{\mathbf{x}},\mathbf{u}) = \begin{bmatrix} V_{air}\cos\psi\cos\theta - \hat{W}_N \\ V_{air}\sin\psi\cos\theta - \hat{W}_E \\ 0 \\ 0 \end{bmatrix}. \tag{2.37}$$

By convention, wind comes from, rather than going toward, the indicated direction. The linearization,

$$A(\hat{\mathbf{x}},\mathbf{u}) = \left.\frac{\partial \mathbf{f}(\mathbf{x},\mathbf{u})}{\partial \mathbf{x}}\right|_{\mathbf{x}=\hat{\mathbf{x}}} = \begin{bmatrix} 0 & 0 & -1 & 0 \\ 0 & 0 & 0 & -1 \\ 0 & 0 & 0 & 0 \\ 0 & 0 & 0 & 0 \end{bmatrix}, \tag{2.38}$$

is predictably sparse, which leads to a simple update of the covariance in implementation.

2.8.2 Stage 3: Measurement Update

The output equations for the inertial estimator are shown in Equation 2.39 and Equation 2.40 below. Although the GPS sensor will output groundspeed and ground track data, the usefulness of the information is questionable. Because they are calculated from successive locations, the relatively infrequent updates of the GPS cause the groundspeed and ground track data to lag, which is a problem while the MAV is turning. While the position measurements are nearly current at the time they are received, the airspeed and groundspeed measurements represent a historical average. The data could be used effectively if a log of estimates, sensor measurements and input data were kept, and a correction applied to a historical estimate, then the model forward propagated in time to the current time, but the merit of using the GPS speed and track data must be weighed against the computational overhead. These equations reflect using only GPS position, which will update each of the states in this filter.

Output equations for this stage are simple when compared to the earlier stages. Because the GPS measurement simply provides another state variables, the sensor update process is relatively straightforward, again, following the procedure outlined in Section 2.4.2, where

$$\mathbf{h}(\hat{\mathbf{x}},\mathbf{u}) = \begin{bmatrix} \hat{P_N} \\ \hat{P_E} \end{bmatrix} \tag{2.39}$$

and

$$C(\hat{\mathbf{x}},\mathbf{u}) = \left.\frac{\partial \mathbf{h}(\mathbf{x},\mathbf{u})}{\partial \mathbf{x}}\right|_{\mathbf{x}=\hat{\mathbf{x}}} = \begin{bmatrix} 1 & 0 & 0 & 0 \\ 0 & 1 & 0 & 0 \end{bmatrix}. \tag{2.40}$$

2.8.3 Stage 3: Noise Model

As with the Stage 1 attitude observer, the noise model of this nonlinear observer requires additional treatment. The inputs to this observer are themselves estimates, and the way that uncertainty enters the states changes with value of the inputs themselves.

Considering uncertainties in heading and airspeed, the uncertainty of subsequent position estimates will be proportional to the airspeed uncertainty along the heading of the vehicle, while the cross-track uncertainty will be proportional to both the airspeed and the uncertainty in the heading. Instead of the uncertainty in the position growing simply with position estimates, the following approximation is made.

We let

$$Q = \begin{bmatrix} Q_{P_N} & 0 & 0 & 0 \\ 0 & Q_{P_E} & 0 & 0 \\ 0 & 0 & Q_{W_N} & 0 \\ 0 & 0 & 0 & Q_{W_E} \end{bmatrix}$$

where

$$\begin{bmatrix} Q_{P_N} \\ Q_{P_E} \end{bmatrix} = \begin{bmatrix} |\cos\psi| & |\sin\psi| \\ |\sin\psi| & |\cos\psi| \end{bmatrix} \begin{bmatrix} Q_{OT} \\ Q_{XT} \end{bmatrix}. \tag{2.41}$$

These estimates of uncertainty are calculated at each time step using the current airspeed and heading and used to update the covariance matrix in Equation 2.12. The user may tune the on-track and cross-track uncertainty (Q_{OT} and Q_{XT}) according to confidence in airspeed and heading estimates.

In addition to this time-varying method of the covariance time update, the noise model for the GPS is dependent on the number of satellites that are being received and used for the GPS measurement. When five or more satellites are being used, confidence in the GPS measurement is high. Confidence in the position measurement drops with four and three satellites, and the measurements will not be used when fewer than three satellites are being used.

Algorithm 3 Stage 3: Position and Wind Estimation

```
Obtain $V_{air}$ from sensors and $\psi$ and $\theta$ from stages 2 and 1.
Update the state estimate using the kinematic update (Equation 2.37).
Compute the linearized state update matrix (Equation 2.38).
Propagate the covariance matrix (Equation 2.41 and Equation 2.12).
if new GPS measurement available then
    for easting and northing measurement do
        Calculate Kalman gain (Equation 2.17).
        Update position and wind estimates (Equation 2.16).
        Update covariance matrix (Equation 2.15).
    end for
end if
```

2.9 Summary of Technical Approach

This chapter began with an overview of test equipment and software, including the test vehicle, human interface, and simulation environment in Section 2.1. After establishing reference frames and notations for variables related to state estimation on MAV's in Section 2.2, the mathematical model representing MAV kinematics is given in Section 2.3. The extended Kalman filter was reviewed as it applies to the the estimation problem presented in Section 2.4. The estimation problem was broken down into a three stage cascaded structure described in Section 2.5. The first stage estimates pitch and roll angles and is detailed in Section 2.6. Section 2.7 covers stage two, estimating heading. Stage three, explained in Section 2.8, estimates position and wind. In the next chapter, simulation results are presented which compare results from these algorithms with baseline algorithms described in Appendix A.

Chapter 3

Simulation Results

Each of the algorithms developed in this work were tested in simulation. Simulation serves at least two important functions. First, when running the test on the MAV hardware, there is no convenient measure of the true state. In this type of research, it is common to compare results to a larger, higher power reference system, which is not possible on this platform, and still does not provide a "true" measure of the state. Simulation has the advantage that, although a the product of a model, a truth values is available for comparison. In the simulation environment, emulated sensor measurements may be logged with the estimated and true states, with any number of intermediate variables. In this way, deficiencies can be identified and initial gain tuning of the observers can be accomplished. This chapter contains results from simulation, where baseline algorithms and the new EKF based algorithms are both compared to the true state data from the simulator, giving a measure of which algorithm is closer to the truth.

3.1 Stage 1: Pitch and Roll Estimation

Results in this section include plots of pitch and roll angles, plots of errors in pitch and roll estimates, a plot of predicted accelerometer measurements and a plot of the sensor update gains. For these simulations, a truth value for each state was available, which is included on the state plots, and is the value used in calculating estimate error.

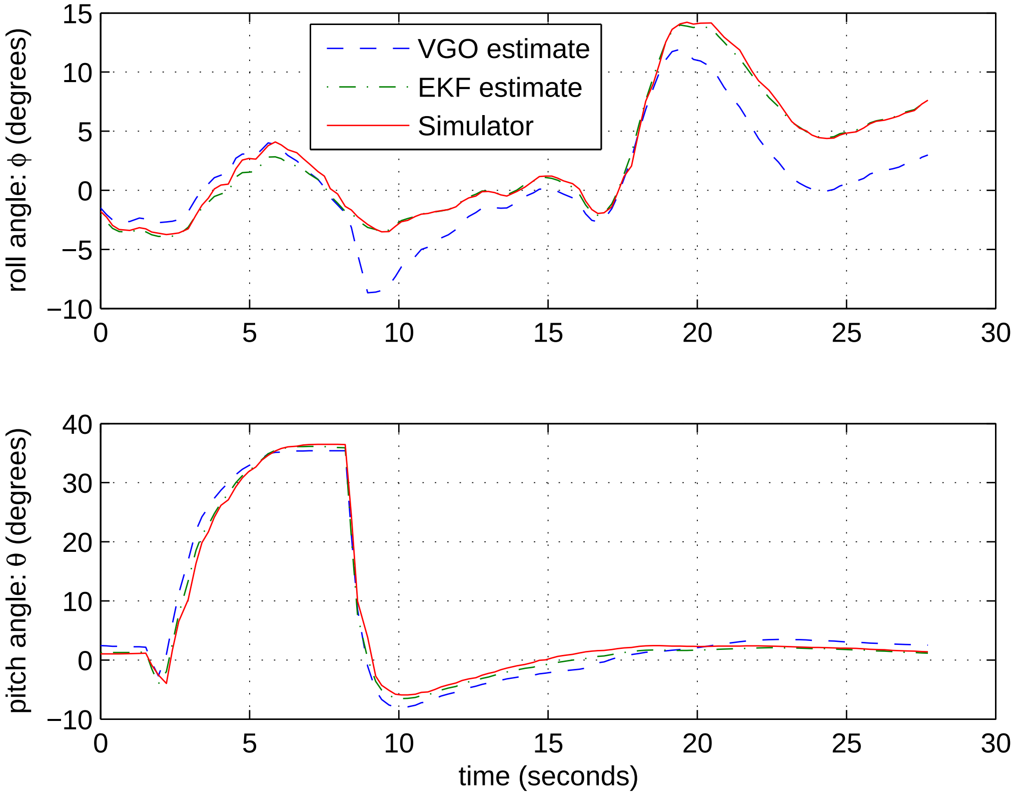

Figure 3.1: Roll and Pitch Estimates With Truth Data During a Climb, Turn maneuver

3.1.1 Climb, Turn Maneuver

The graphs in this section come from a set of data taken in a test in which the simulated vehicle begins a climb two seconds into the test, leveling off at one hundred meters altitude at nine seconds, continues straight and level for several seconds, then rolls into an orbit to the right beginning at 17 seconds. This maneuver was chosen because the rotation into and out of the climb includes a sharp, unmodeled acceleration which tests the gain scheduling described in Section 2.6.3. The orbit portion of the maneuver showcases the ability of the EKF observer to maintain an accurate estimate in a sustained bank, where it is necessary to account for centripetal accelerations to use the accelerometer measurements effectively.

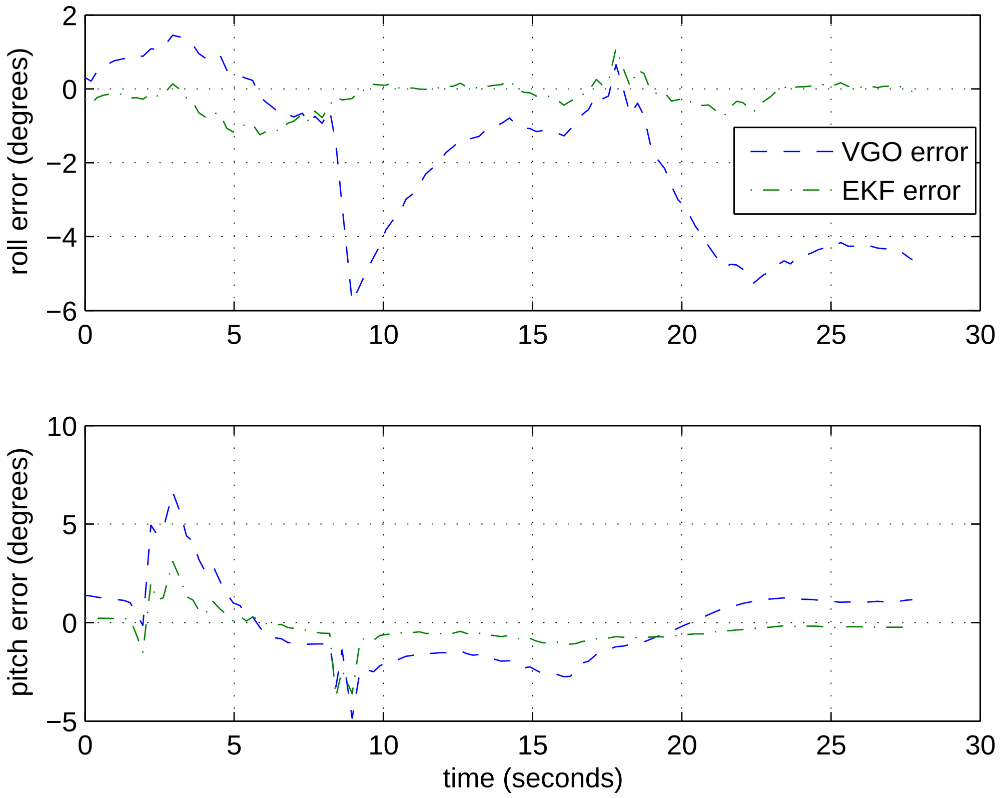

Figure 3.2: Error in Pitch and Roll Estimates

Figure 3.1 shows both the variable gain observer estimates and the estimate from the extended Kalman filter plotted with the states from the simulator. Figure 3.2 shows more clearly the magnitude of the errors. Notice that the errors from the EKF estimate estimate are within two degrees in roll and three degrees in pitch, in both cases an improvement over the VGO. The EKF measurement remains relatively close to the truth value in pitch and roll, while the VGO roll estimate deviates at two notable times. At seven seconds, the VGO roll estimate overshoots by more than five degrees to the right while the MAV is in a rapidly pitching down. At nineteen seconds, the MAV has rolled into a turn, and the VGO is five degrees in error, this time, lagging, and does not appear to be recovering.

Figure 3.3 shows the the predictions and measurements of the accelerometers. The measurements come from the calibrated sensor readings, while the predictions

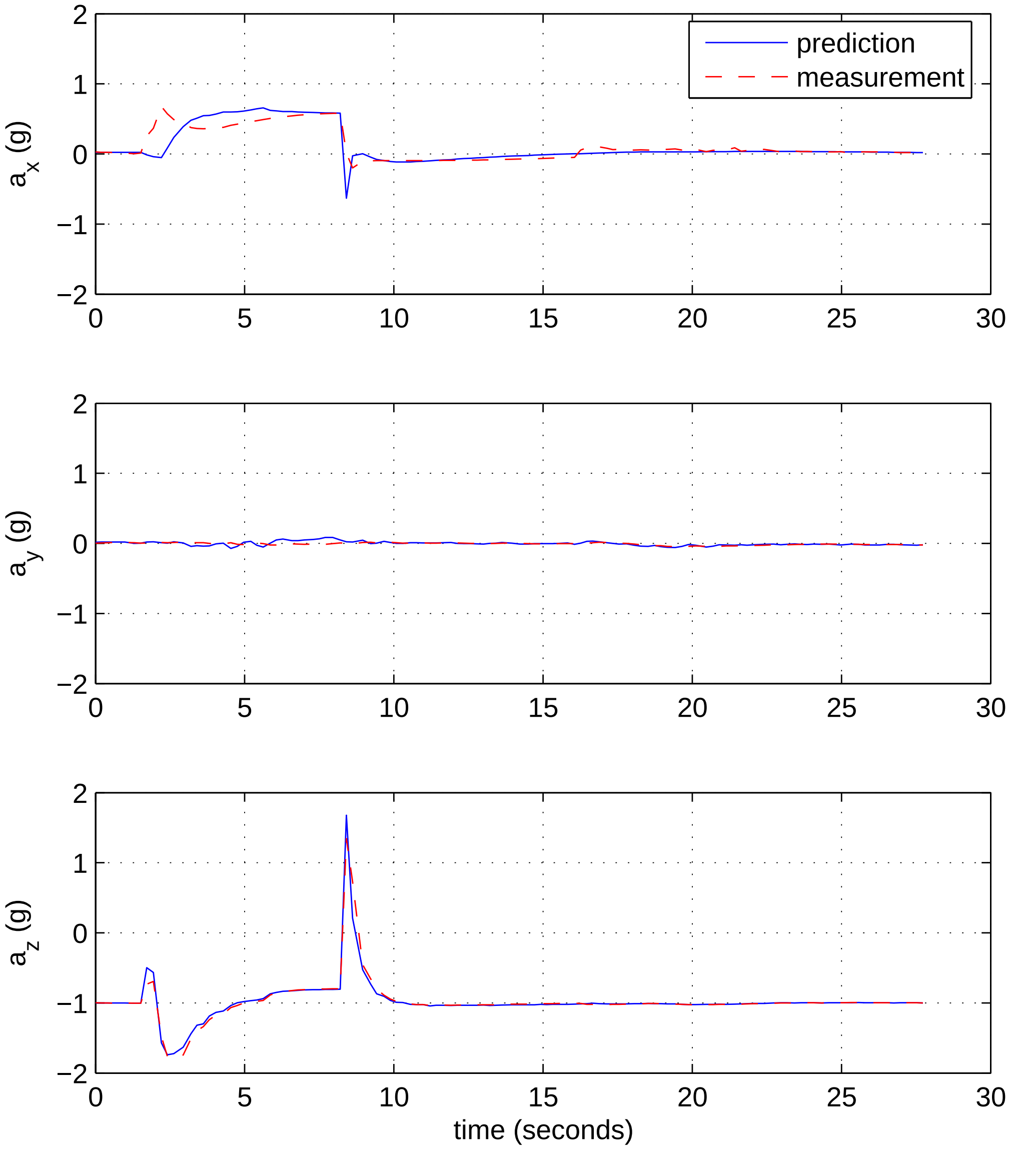

Figure 3.3: Stage 1 Outputs During a Climb, Turn Maneuver

are calculated as described in Section 2.6.2. These predictions include centripetal accelerations calculated using resolved airspeeds and angular rates.

The first graph shows the weakness of the prediction on the x-accelerometer in some stages of the maneuver. This failure to predict the x-accelerometer measurement is due to the level flight assumption described in Section 2.6.2. In a climb, the body frame z component of velocity (w) will be overestimated, while the x component (u) will be underestimated. When these components are crossed with a large angular rate q, as shown in Equation 2.5 the result is an error in the prediction of the x accelerometer reading. The relative sizes of u and w appear to leave less of an effect on the z-accelerometer prediction, which follows large swings accurately.

Figure 3.4 shows the weight of each sensor correction on each of the states. The first graph of shows that the filter was able to shut down accelerometer updates from the x-axis during the high pitch rate portion of the maneuver, when its prediction was inaccurate. It is instructive, also, to look at the relative weight each sensor lends to the states. The y-accelerometer, for instance, is the only sensor which gives more input to roll than pitch. Also note that the z-accelerometer is largely ignored in level flight. Where there is a large deviation in pitch, such as between five and eight seconds, the z-accelerometer is used in the pitch update. After 22 seconds, there is a gain on pitch and roll, where the MAV has rolled into its orbit and has been holding a bank.

3.1.2 Steady Orbit Maneuver

A second simulation experiment consists of a position-holding orbit with a radius of 150 meters. Such a maneuver might be used in a surveillance operation. Because it is common to hold a circular orbit for a period of time, and because this maneuver steadily induces dynamic loads on the accelerometer measurements, it is important to observe the behavior of the observers in this situation.

Figure 3.5 shows the estimates of the roll and pitch angles during the maneuver, with roll corrections on the order of two degrees to maintain the orbit on center. Besides these corrections, the observers appear to have reached a steady behavior in both roll and pitch. In roll, the VGO estimate is clearly biased, but has transient behavior which lines up nicely with the truth value. In pitch there is also a bias error on the VGO, with a ripple which may be correlated with the changes in roll angle.

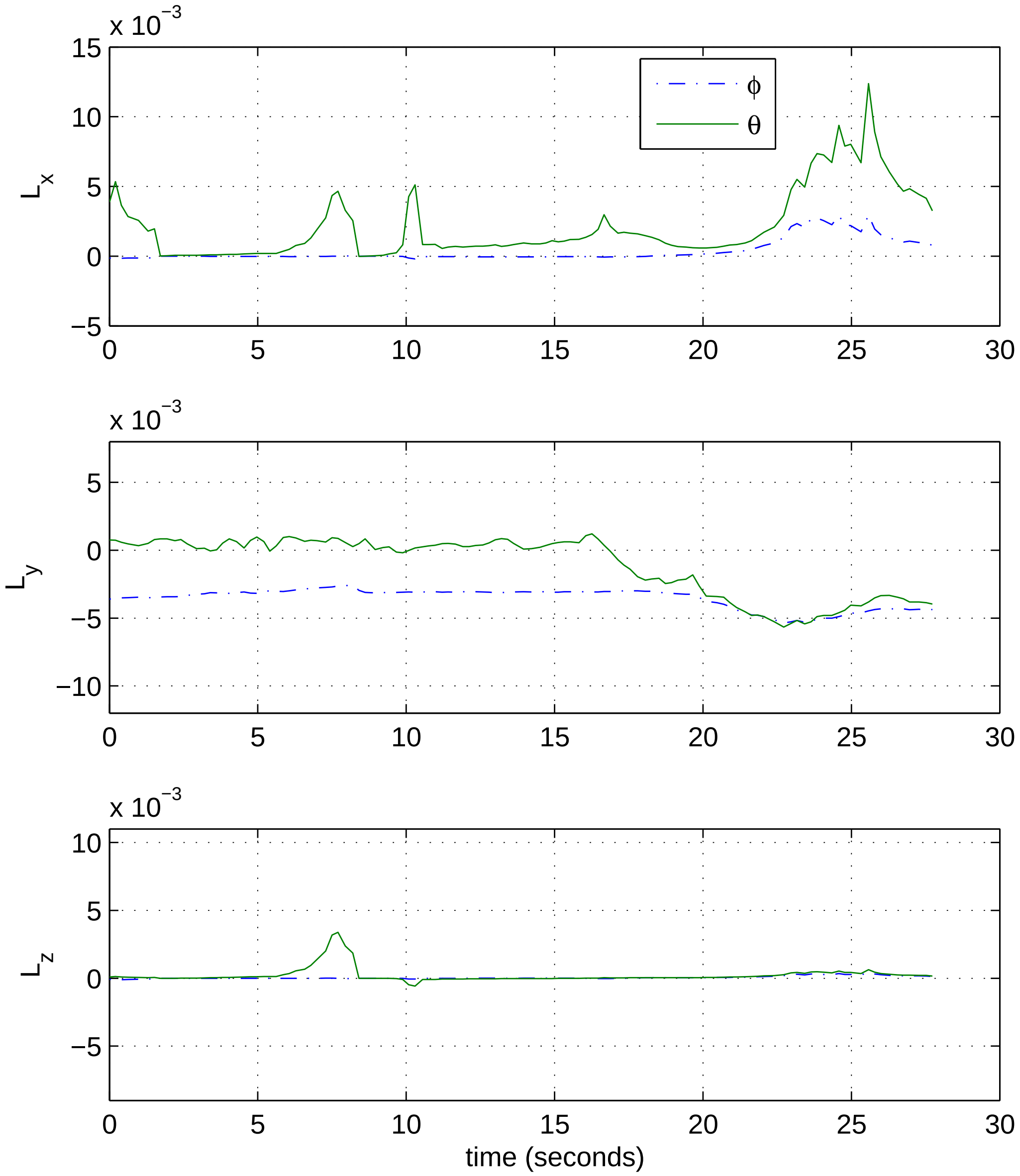

Figure 3.4: Stage 1 Gains During a Climb, Turn Maneuver

The EKF estimate is hardly distinguishable from the truth value in roll, and is a fraction of a degree in pitch.

Figure 3.6 shows more clearly the steady-state error in roll and pitch. Errors in the EKF appear to be zero mean and within a fraction of a degree in amplitude for

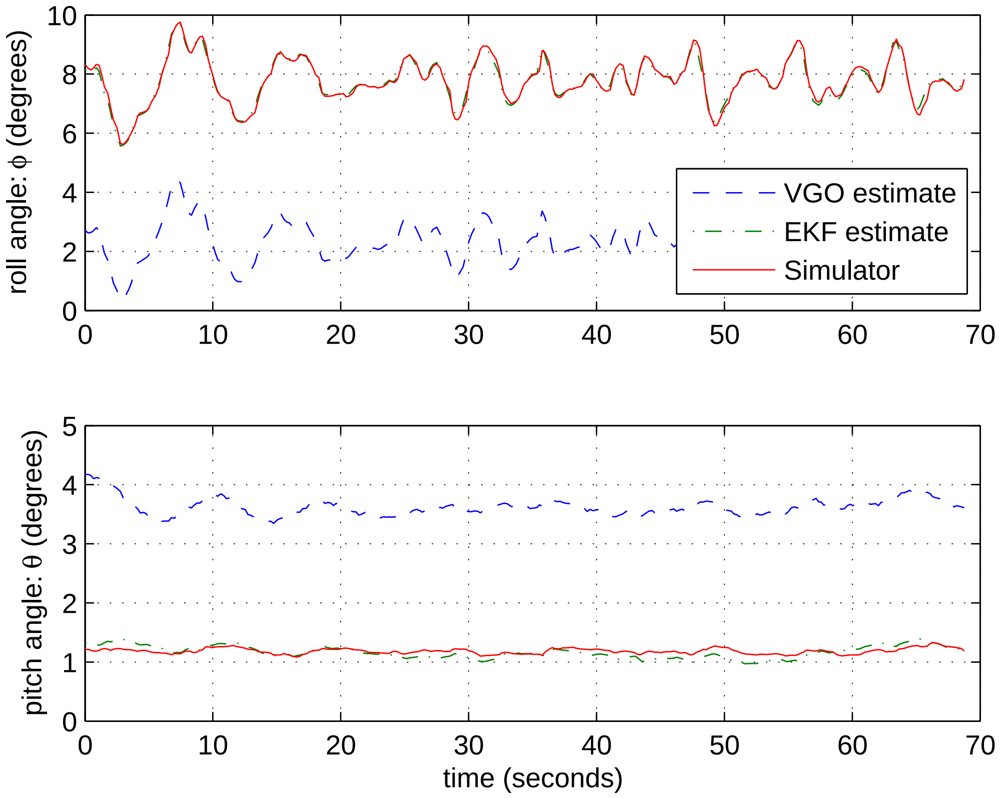

Figure 3.5: Roll and Pitch Estimates During a 150 Meter Orbit Maneuver

both pitch and roll. VGO errors have a mean of almost six degrees in roll and over two degrees in pitch. In both pitch and roll, the error oscillates with roughly half a degree of amplitude.

The need to account for noise in the sensor predictions as well as the measurements was mentioned in Section 2.6.3. Figure 3.7 illustrates cases where the dominance of noise by the sensor and predictor depends on the axis in question. For the x-axis, sensor noise is dominant, the prediction being relatively noiseless. On the other hand, the prediction on the y axis is noisier than the sensor measurement. Predictions and measurements for the z-axis are very well matched. The actual sensor noise for all three axes is similar, but a look at the relative magnitudes of the velocities u and w and a trip through Equation 2.26 gives insight to the different magnitudes of the predictor noise. The noise in the predictions originates with noise

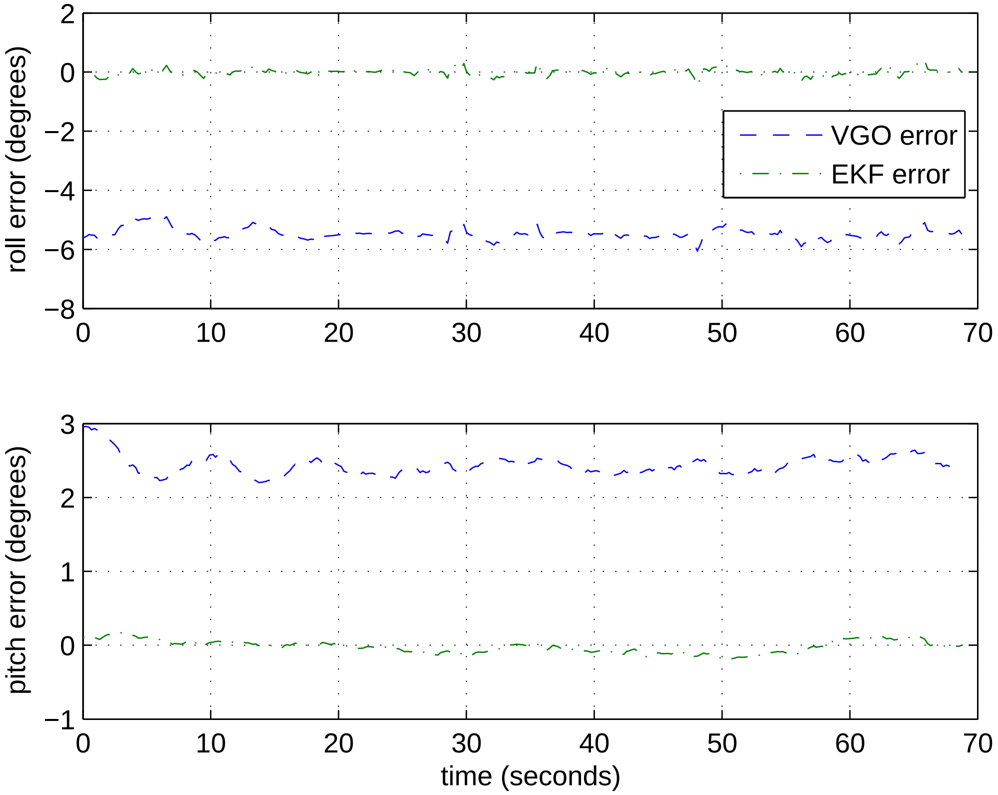

Figure 3.6: Stage 1 Errors During a 150 Meter Orbit

on the rate gyros, represented by p, q and r. When these sensor are cross multiplied with the approximations of u, v and w, the influence of the gyro noise is scaled by the magnitudes of the velocities. The value of v being assumed zero leaves the x-axis with noise from the q-gyro scaled by a relatively small w. The y axis prediction gets a relatively large amount of noise from the r gyro, being scaled by u, and also gets additional noise from the p-gyro, scaled by w. The z-axis prediction, with nothing from the p-gyro because it is scaled by zero, gets a moderate amount of noise from the q gyro, scaled by the larger value, u. In short, eliminating the gyros multiplied by v leaves the x axis with only a small amount of gyro noise, while the y-axis gets gyro noise from two gyro axes.

In a steady orbit, Figure 3.8 shows that gains for all axes are relatively constant. It is interesting to note which sensors are most heavily used in this orbit

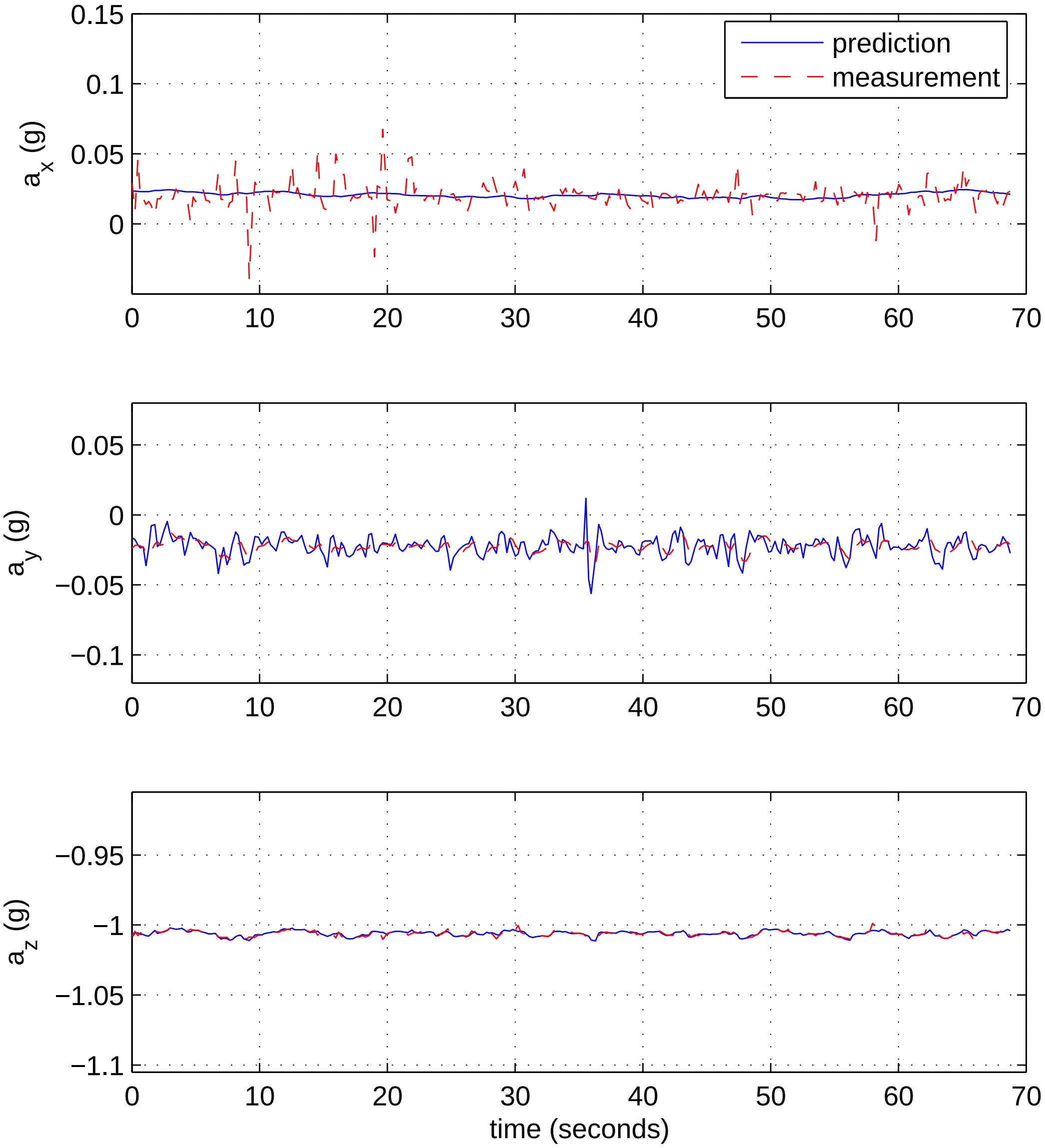

Figure 3.7: Stage 1 Predictions and Measurements During a 150 Meter Orbit

situation. Again, the z-axis is not heavily utilized, but the x and y axes are used for both pitch and roll updates. The relatively small consideration of the z-axis makes sense considering that perturbations in the z-accelerometer in a near-level attitude,

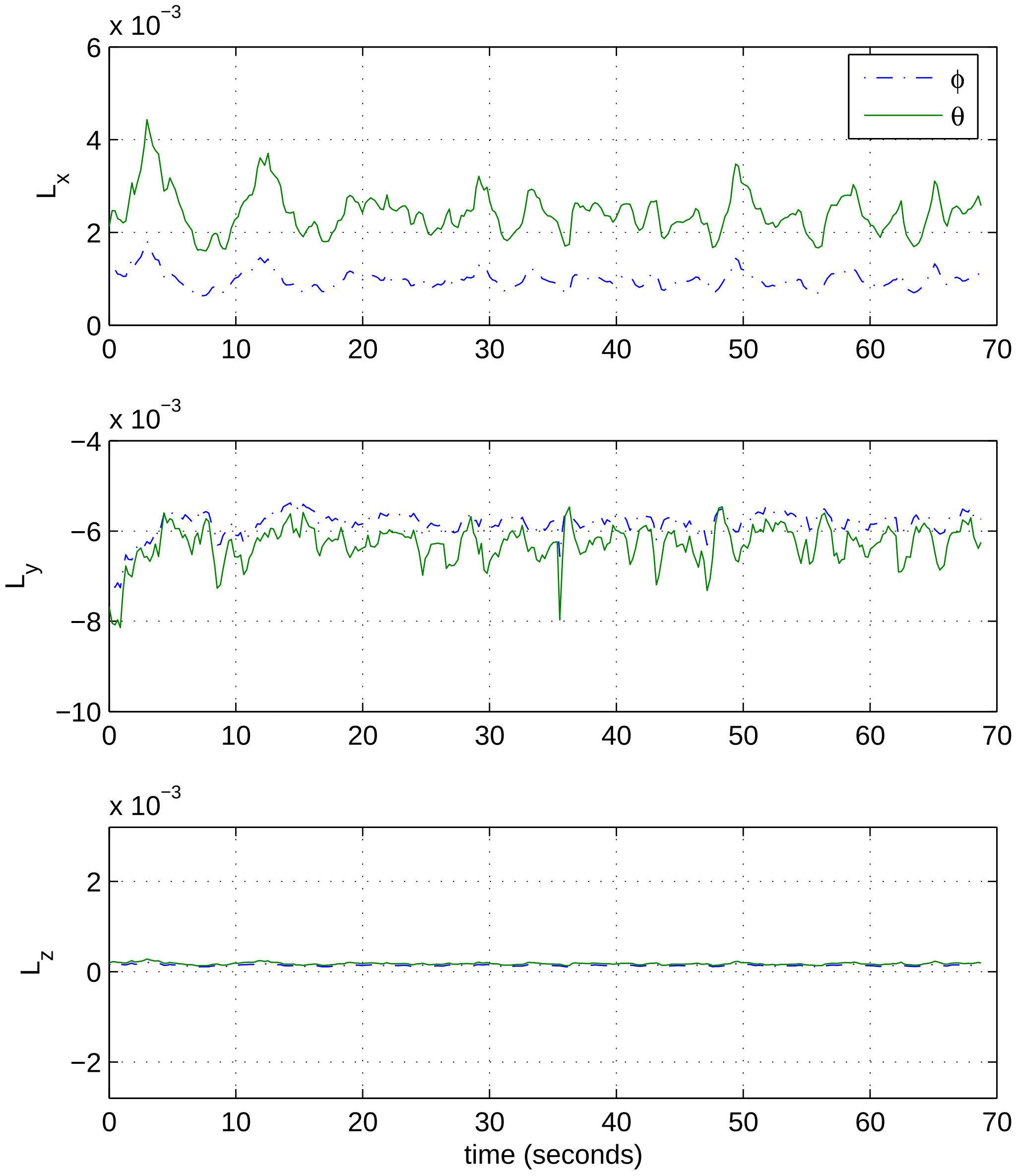

Figure 3.8: Stage 1 Gains During a 150 Meter Orbit

or in this case, a coordinated turn, cannot be distinguished as being due to a right or left turn nor forward or backward pitch.

In this sort of maneuver, the EKF observer is clearly superior at estimating pitch and roll. The superiority is likely due to the fact that there are no unmodeled dynamics in this maneuver. The centripetal acceleration from the turn is modeled in the sensor outputs shown in Equation 2.26. In this case, none of the simplifying assumptions are violated and the model is complete, yielding a good estimate of the pitch and roll.

3.2 Stage 2: Heading Estimation

The simulation data for the heading estimator was taken using a climb then turn maneuver similar to the first maneuver demonstrating the attitude estimator. In this case, the climb portion is not apparent in the estimation data, since the heading was not changed, but the heading data in Figure 3.9 does show that a complete turn through all headings was executed. EKF estimates are compared to the original heading derived from the simulated GPS measurement, described in Appendix A. EKF heading estimates are accurate within two degrees, where the original estimates are accurate within ten degrees.

Although the pitch up portion of the maneuver is invisible in the state estimate, The EKF sensor output plots in Figure 3.10 show a large change magnetometer predictions through the pitched up portion of the maneuver, followed by the predictably sinusoidal measurements during the turn. The large deviations on the x and z axes during the pitch up make clear the need for using pitch and roll information in making magnetometer predictions. Had these swings not been predicted, they would have caused the heading estimate to change when the heading was not changing.

The graphs of the observer gains in Figure 3.11 serve as an illustration for the same principle as was apparent in Stage 1. The magnetic field vector points in a direction roughly 11 degrees east of north, and when the vehicle is on that heading, the x-axis is at its peak reading, so a deviation is attributable to neither a turn to the left nor right. This insensibility is reflected by a gain of zero on the x-axis at that heading. The z-axis is predictably less weighted than the x and y-axes in general.

Another important feature of using an Extended Kalman Filter to measure an angle is apparent from Figure 3.10 and Figure 3.11. As the state continues to increase, the sensor predictions move in sinusoids. Consequently, the Kalman gains are also

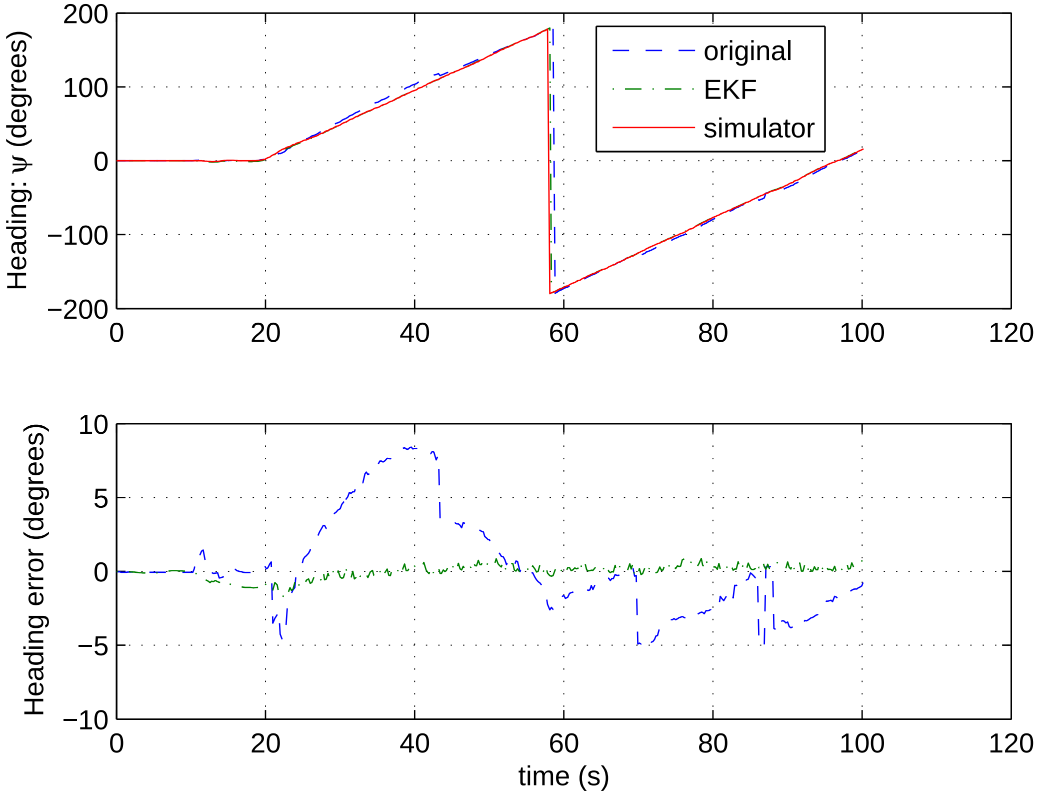

Figure 3.9: Heading Estimates and Error in Estimates Before and During an Orbit

sinusoidal. The implication of this is that the state can greatly affect, even change the sign of, the sensor update gains. It is therefore possible for a particular sensor measurement, if the state is sufficiently wrong, to drive the estimate to an even more incorrect state. Another problem arises when the state variance is allowed to grow unbounded. In that case, the the Kalman gains coupled with a sensor measurement could cause a correction which overshoots the true state. This phenomenon was not apparent in the pitch and roll estimates because the MAV does not often make a sweep through all possible pitch and roll angles, but stays relatively bounded, and therefore closer to a near linear condition.

Notice that when the sensors are at their peak values, the gain is closest to zero. This happens because the gain is largely driven by the linearization of the output equations, putting the two out of phase. The consequence is that the when

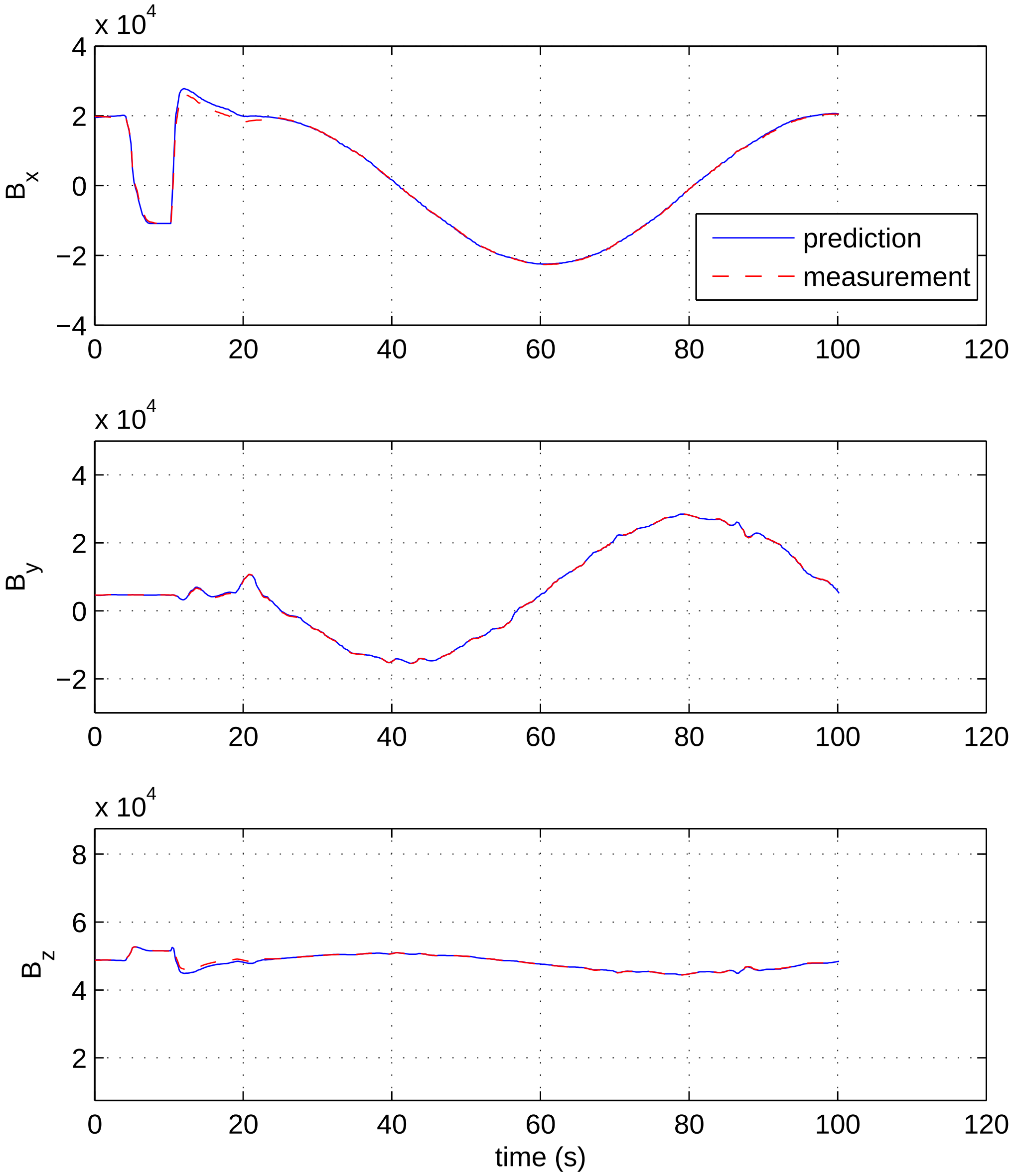

Figure 3.10: Magnetometer Predictions and Measurements Before and During an Orbit

the sensor readings are at their strongest, they are least useful. This makes sense, since at an extremity, it is difficult to distinguish a turn to the right from a turn to the left by a small drop from the peak reading. The sensor readings in this case are most useful while near the center of their sensing ranges.

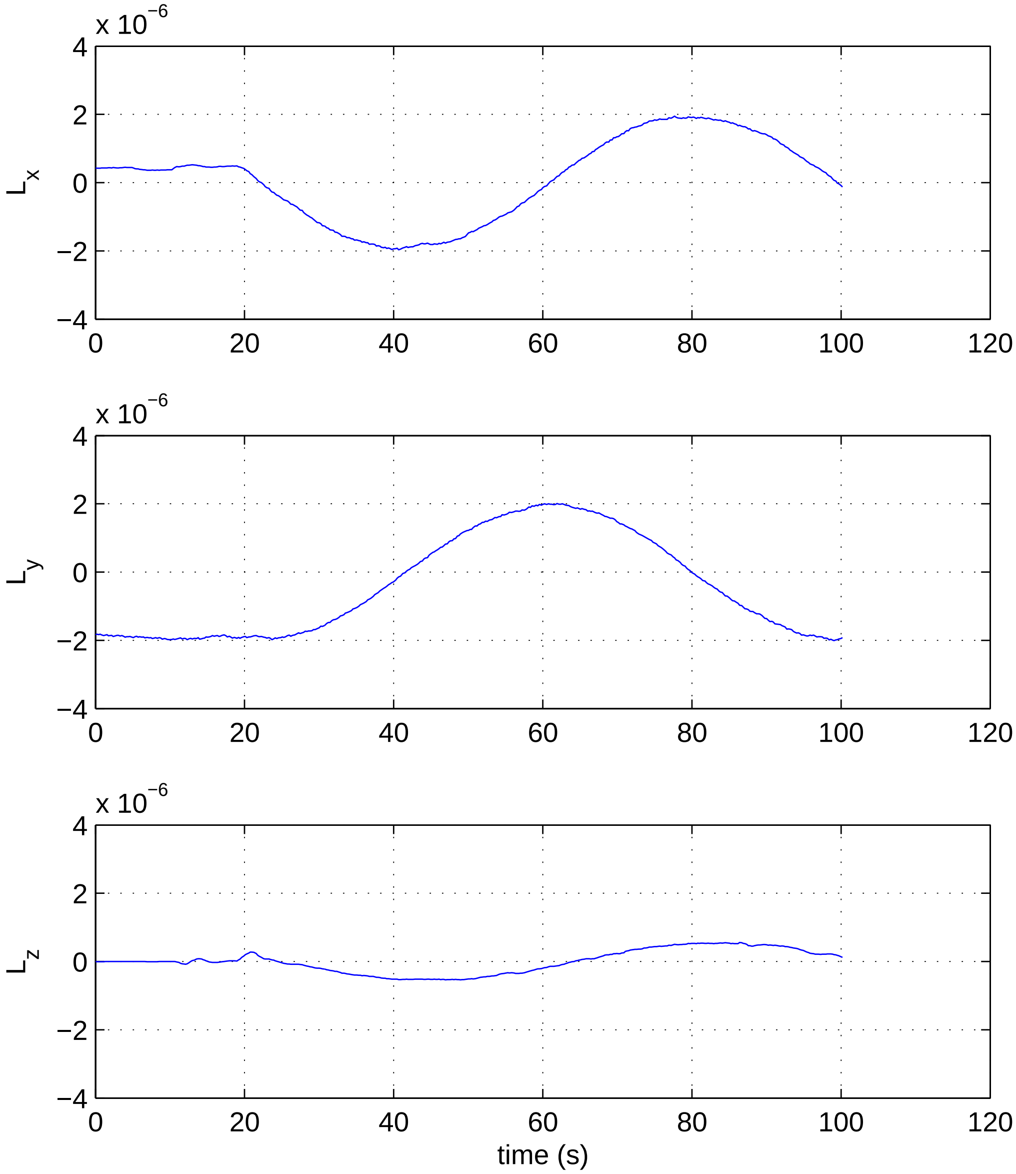

Figure 3.11: Heading Observer Gains Before and During an Orbit

3.3 Stage 3: Position and Wind Estimation

The third stage of the estimator was simulated in an orbit situation. The simulated GPS measurements were generated by taking the simulator location and adding random noise. Figure 3.12 shows a segment of the orbit. The MAV is in a right turn, so the progression in time is from the right of the graph to the upper left, moving upward in the plot as the vehicle turns right. A 4 m/s wind from the south was introduced a few moments after the vehicle passed through an Eastern heading. The radius of the orbit is 75 meters.

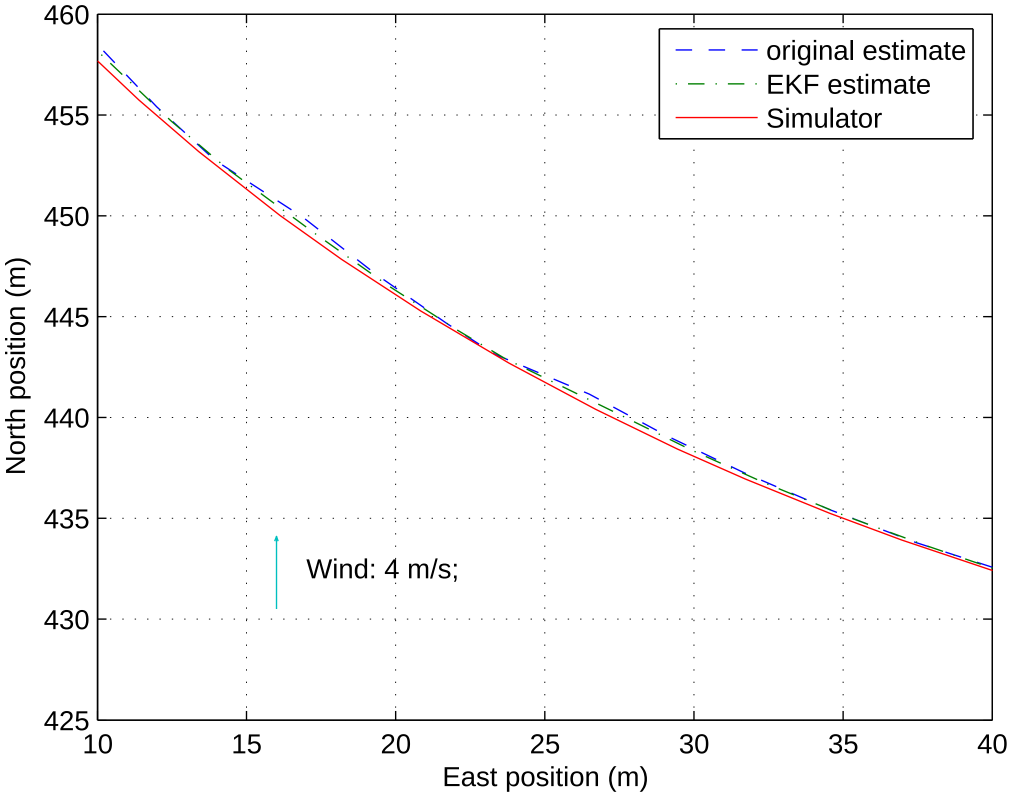

Figure 3.12: Segment of Simulated Orbit Showing Actual Ground Track and Estimated Locations

Errors in the default smoothed GPS measurement and the EKF are similar over the course of the orbit, as seen in Figure 3.13. The effect of the wind is apparent in the position plot, altering the shape of the periodic position measurements. The vehicle moves very quickly northbound, and more slowly southbound. Error in position estimates is comparable over the course of the orbit, both estimates are affected

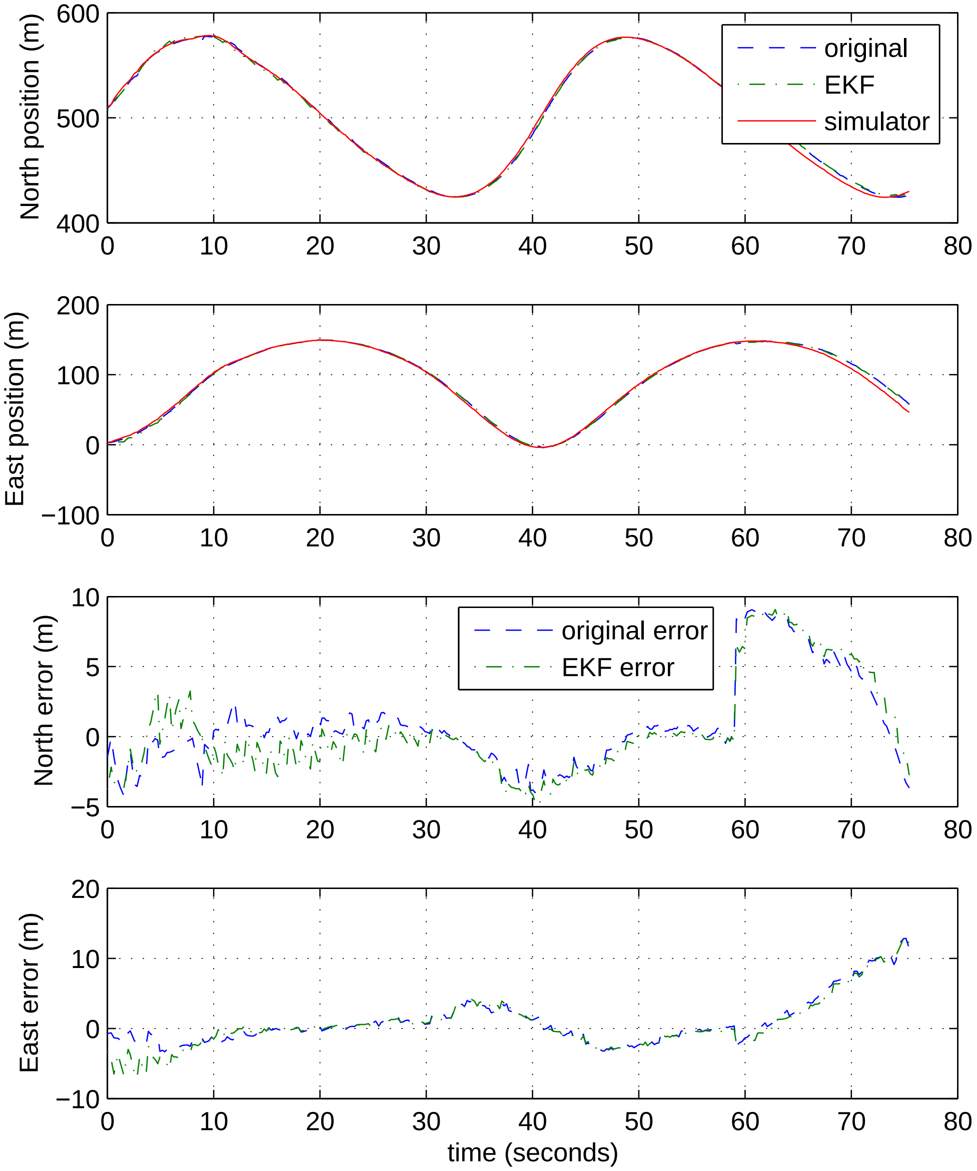

Figure 3.13: Position vs. Time and Position Error vs. Time in Position Estimates

by what appears to be a step in the GPS measurement at 59 seconds, and both estimates lag behind the truth when the vehicle makes its fast northbound portion of the orbit between 35 and 47 seconds.

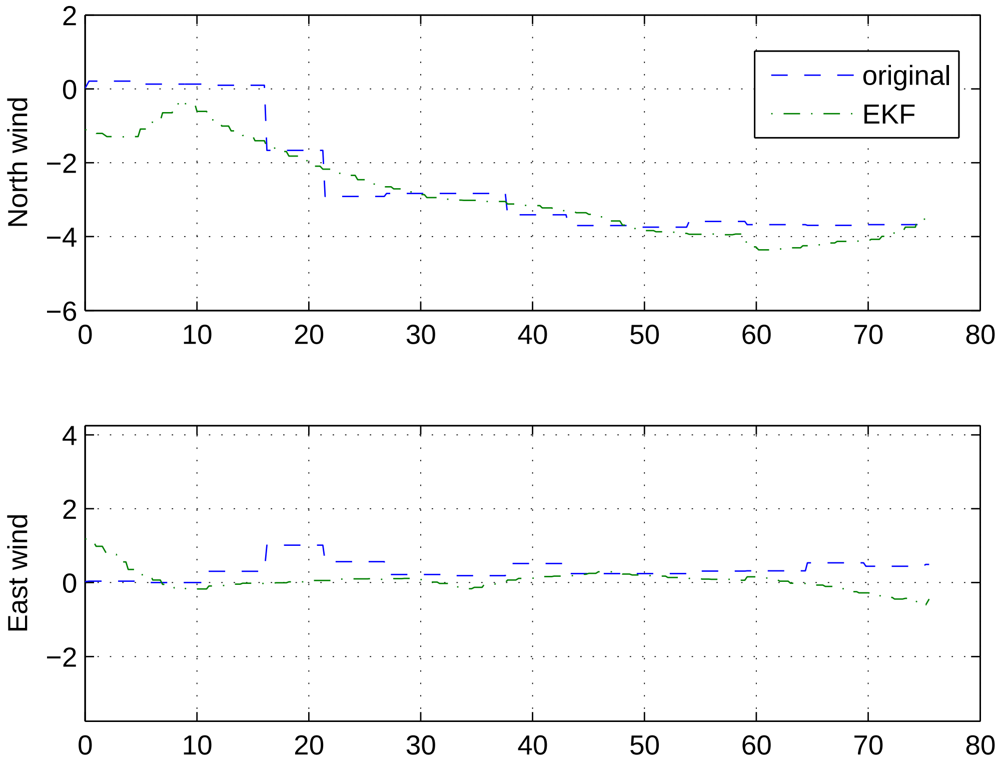

Figure 3.14: North and East Wind Estimates

The plot of wind estimates in Figure 3.14 shows both the default and the EKF east wind estimate remaining close to zero, while the north estimates move toward negative four meters per second, indicating a wind from the south. The EKF wind estimate is more continuous than the original estimate, which must wait for a sufficiently changed ground track to update its estimate, but both converge at roughly the same rate. Both estimates may be allowed to converge faster, but at the expense of a noisier estimate. Ideally, the supporting information to the EKF, that is the airspeed, heading, and GPS measurements, would be noiseless and perfectly calibrated, which would allow faster tracking. In this case, there is error in the heading and airspeed information, necessitating a slower convergence so that the estimate may converge over the period of an orbit and the errors are filtered. The rate of convergence represented here is useful for tracking the general trend of the wind, which would be the most useful information in the event of GPS denial. In that event, wind estimate updates cease, and the estimate remains at its last value. If that value represents a mean, the dead reckoning navigation will be most accurate over time, whereas if the estimate was tracking a transient change at the time of denial, the position estimate would deteriorate more rapidly.

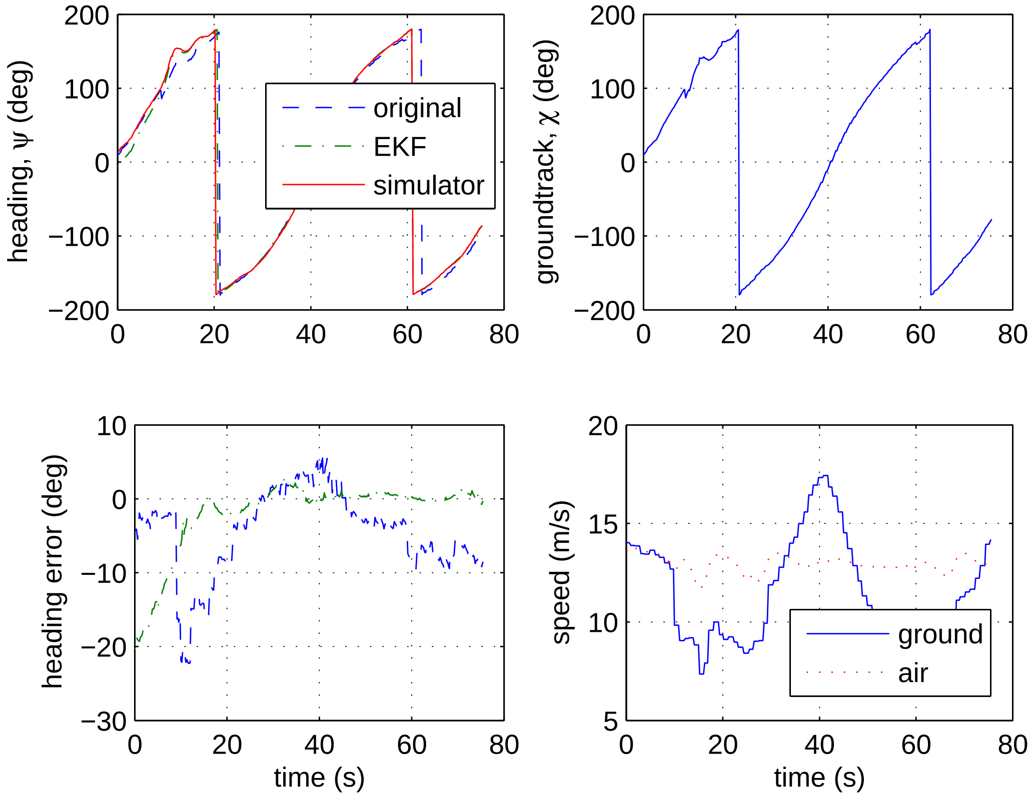

Figure 3.15: Inputs to Estimator With Ground Track and Ground Speed

In evaluation the performance of the navigation observer, it is of interest to watch the quality of the input variables, particularly airspeed and heading. Also of interest is observing the GPS derived ground speed and ground track. These variables are plotted in Figure 3.15. The step in wind is readily apparent in the plot of groundspeed, versus airspeed. Airspeed remains relatively constant, but the two estimates diverge where the wind step occurs at about ten seconds. Thereafter, the groundspeed alternates periodically about the airspeed, showing a maximum on Northbound ground tracks and minimums on Southbound ground tracks as is expected with a Southerly wind.

3.4 Summary of Simulation Results

Simulation results for each stage of the estimation scheme were compared to baseline algorithms described in Appendix A and to the ”true” states output by the simulator. Section 3.1 compared pitch and roll estimates. Transient performance of the EKF algorithm was superior to that of the VGO, demonstrated in a climb then orbit maneuver. A steady-state orbit maneuver showed the superiority of the EKF in compensating for dynamic accelerations, being free of bias in the error. In each test, the EKF error was within a degree of the truth value from the simulator. Section 3.2 compares the second stage of the estimation scheme, which estimates heading, with the baseline heading estimate, which is also described in Appendix A. The baseline estimate, however, is dependent on GPS smoothing. The EKF heading estimate shows favorable performance in a climb then turn maneuver, and is independent of the GPS measurement. Section 3.3 compares the EKF navigation observer to the original GPS smoothing and wind estimation algorithms, again covered in Appendix A. The performance of the navigation and wind estimation algorithms is similar.

Chapter 4

Flight Test Results

The end goal of this research is improvement of estimation results for miniature air vehicles (MAV's). To that end, it is necessary to test the algorithms on MAV hardware to evaluate their performance with the computational constraints of the autopilot processor, and real sensor measurements, complete with noise and biases. In the hardware environment, we do not have the luxury of having a truth value for the states, so it is sometimes necessary to compare estimates to each other and monitor emergent behaviors which result from the estimation. A side by side comparison of baseline estimation schemes and the three-stage cascaded scheme follows.

4.1 Stage 1: Pitch and Roll Estimation

Simulation results for the first stage are validated by hardware testing. The variable gain observer and the extended Kalman filter are again run simultaneously in two experiments. In the first experiment, a bank angle is held and altitude is held without regard for maintaining any geographic position. In the second experiment, bank angle is dictated by a heading controller which is holding an orbit about a specific location. Comparing the VGO to the EKF, it is clear that the EKF is less affected by sustained bank angles.

4.1.1 Bank Angle Hold Experiment

Figure 4.1 and Figure 4.2 represent state estimates from hardware flight tests using the VGO (described in Appendix A) and the EKF attitude estimation scheme. The two observers run simultaneously in each case. The distinction between the two data sets is that in Figure 4.1, the VGO is used for feedback control of the MAV, whereas Figure 4.2 represents the EKF being used for feedback.

The altitude of the vehicle is logged concurrently with the state estimates in the execution of a 55 degree bank while attempting to hold altitude. The affect of the attitude estimate on the altitude provides an interesting metric as to the health of the estimate, since actual pitch and roll are not available to for comparison, altitude behavior can give us an idea of what the actual pitch and in some cases, roll are.

The roll controller is generally clamped to limit the commanded roll angle to 35 degrees. For this experiment, the roll limits were expanded to allow a more aggressive maneuver. It is wise to limit the roll angle at times when the airspeed is slow to prevent an accelerated stall.

The controlled bank is held close to the desired value by the roll controller, but the Kalman Filter estimator indicates roughly 30 degree swings in roll. Both schemes report large pitch oscillations at the same frequency which are reflected in the altitude measurement. The period of these oscillations corresponds roughly with the period of the orbit generated by the bank. The EKF roll estimate continues to climb over 90 degrees, indicating that the VGO estimate was in decay. At 30 seconds in the experiment, it was necessary to terminate the experiment as the MAV was indeed rolled beyond 90 degrees and was no longer able to hold altitude.

In the next experiment, plotted in Figure 4.2, the roll angle was controlled using the EKF estimate. In this situation, the EKF pitch estimate remains relatively constant. The VGO estimates oscillate in both pitch and roll, but to contrast with the EKF estimate under VGO control, the VGO estimates remain bounded as the vehicle remains in a stable orbit. The correlation with the orbital period is not apparent in the gross behavior, and given time, the MAV returns to and holds at the desired altitude of 100 meters even at this relatively steep bank.

4.1.2 Loiter experiment

Holding a steep bank angle is useful for proving the stability of the attitude observer, but the maneuver is not terribly useful, as it leaves the aircraft drifting in

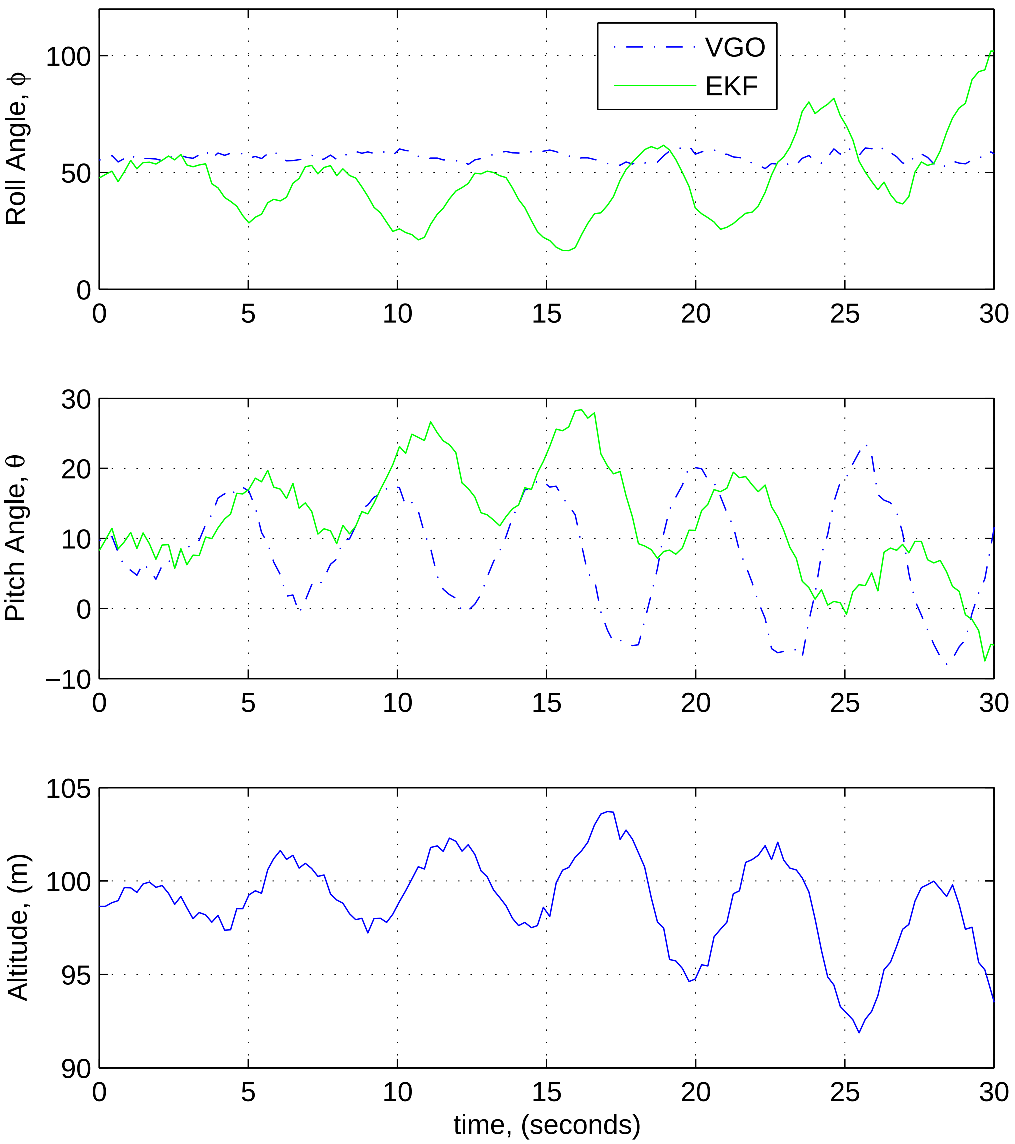

Figure 4.1: Bank Angle Hold at 55 Degrees Using the Variable Gain Observer for Feedback Control.

the wind. The following plots are from a data set in which the aircraft is holding a 15 meter radius orbit. For comparison, the smallest orbits generally flown are of 30 to 50 meter radius, requiring much shallower bank angles.

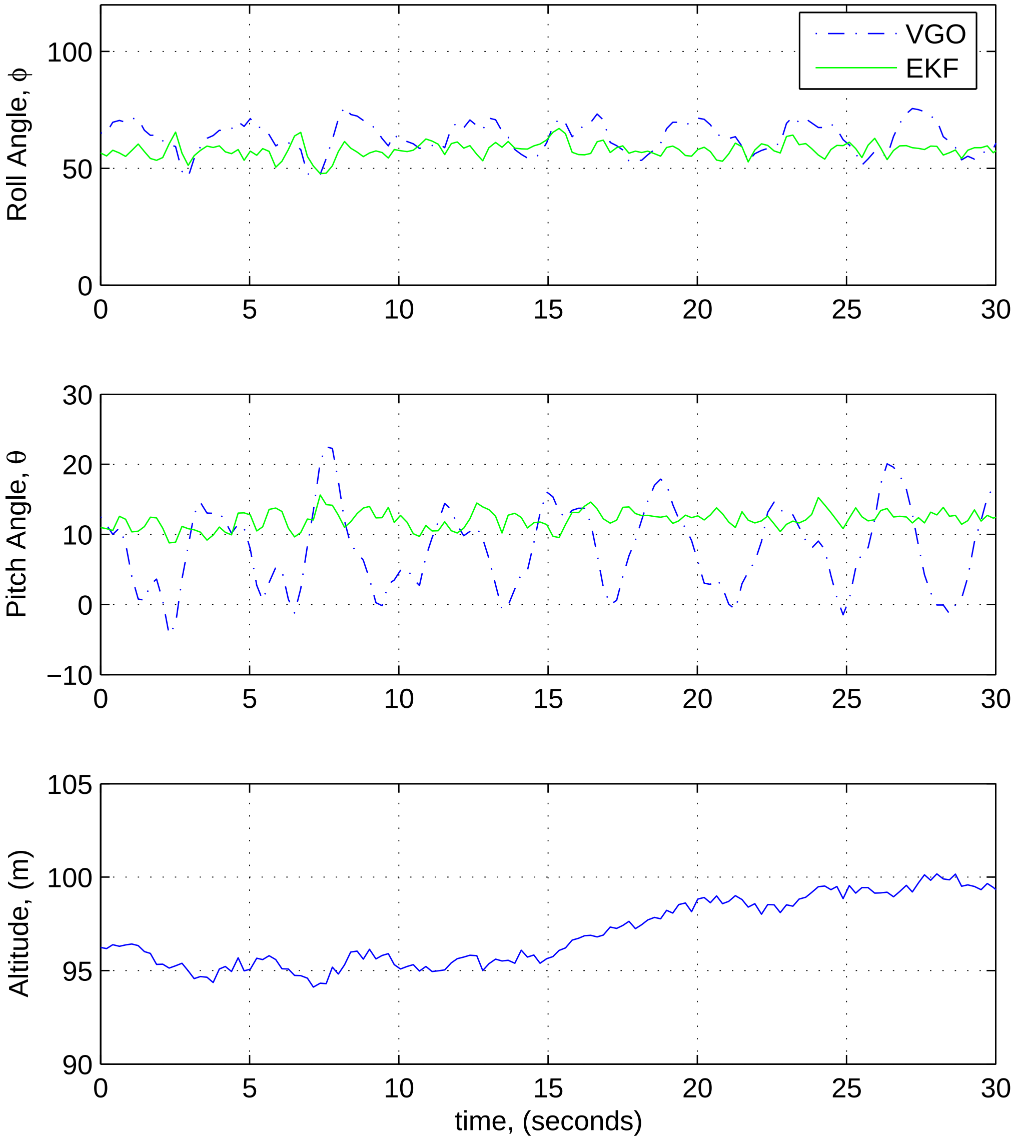

Figure 4.2: Bank Angle Hold at 55 Degrees Using the EKF for Feedback Control.

As with the previous experiments, it was necessary to expand the roll limitations on the roll controller. As can be seen in Figure 4.3, in this tight orbit, the swings in roll were necessarily large in order to keep the center of the orbit from drifting.

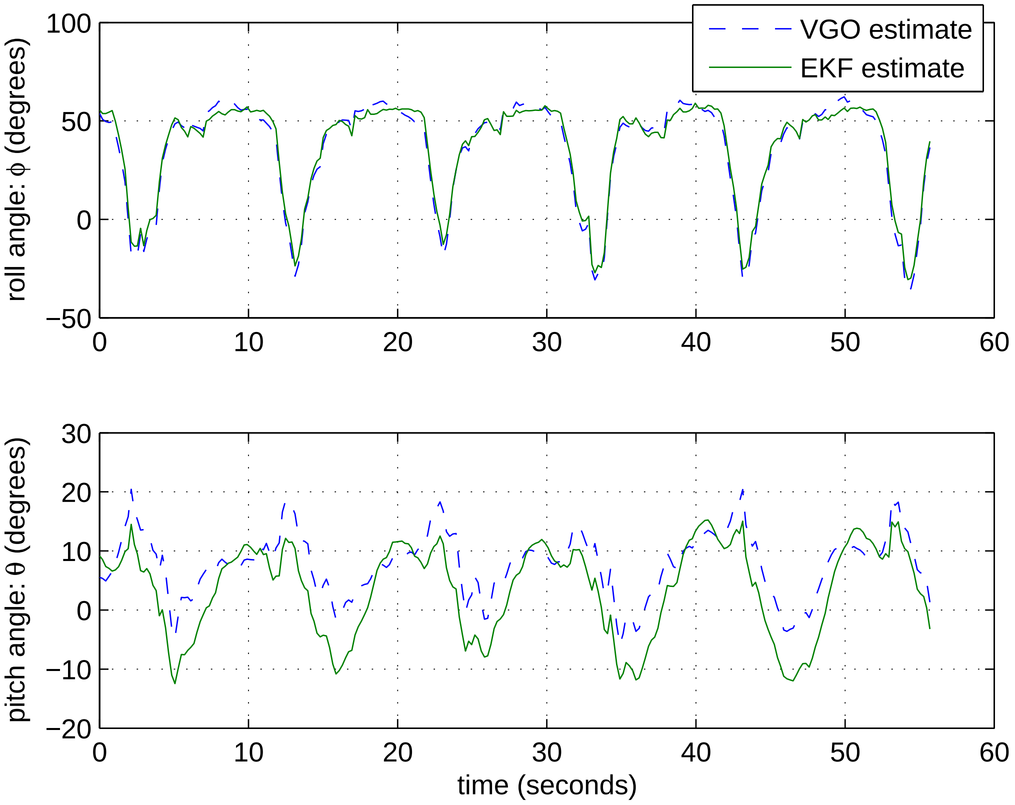

Figure 4.3: Bank Angle Estimates During 15 Meter Radius Orbit

The roll was high on the downwind half of the orbit, leveling for a small segment on the upwind side where the groundspeed was slowed by the wind.

Since truth data is is not available in the hardware test environment, it is instructive to view the difference between the estimates, shown in Figure 4.4. It appears that the decay of the roll angle estimate for the VGO is not as pronounced when the vehicle makes large angle corrections necessary to hold a tight orbit in a wind.

In this steep maneuver, the noise on the predictions becomes very apparent. It is clear that the noise on the rate gyros is affecting the noise of the accelerometer prediction, and that it is affecting the x accelerometer differently from the y and z accelerometers. It appears even more pronounced than in the simulation environment,

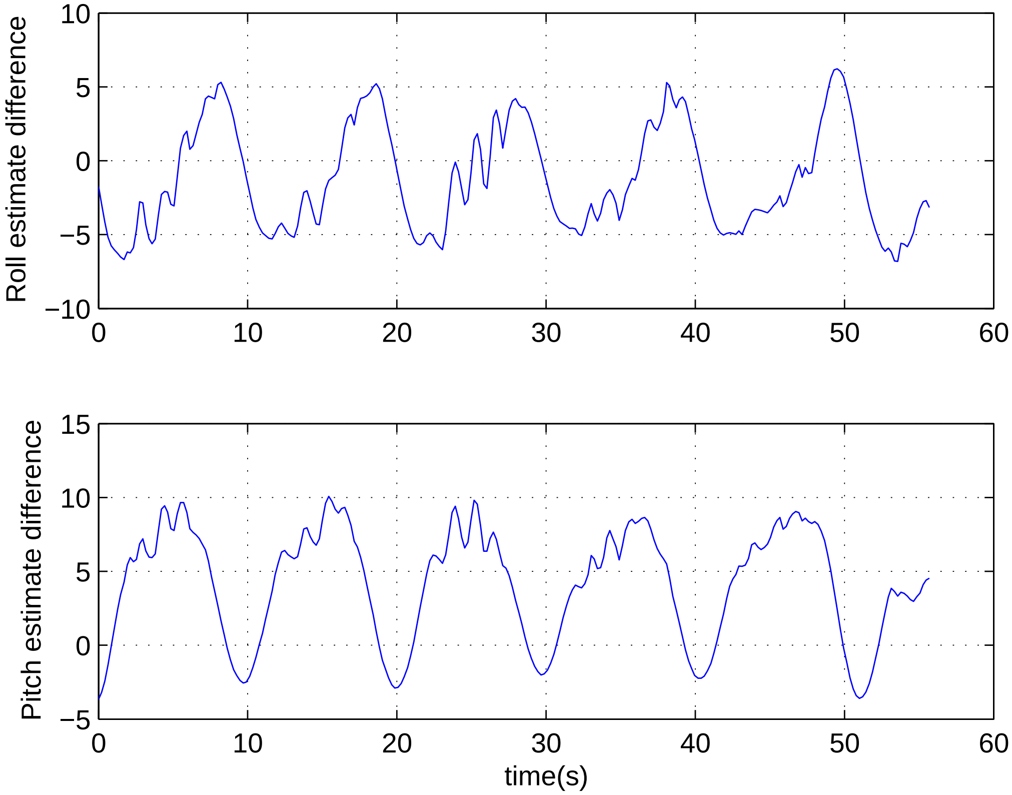

Figure 4.4: Difference Between EKF and VGO Bank Angle Estimates During 15 Meter Radius Orbit

but it is important to note that the roll angles are much steeper in this particular experiment, being a 15 meter orbit rather than a more typical 150 meter orbit.

The x accelerometer is limited in its influence in this situation because of the penalty assigned to it in the high pitch-rate maneuver. It is used periodically in updating the estimates, but as Figure 4.5 shows, matching predictions and corrections is rare, occurring at roughly ten second periods. By looking at Figure 4.6, we see that the algorithm is disallowing x-axis updates most of the time, with short updates allowed at two seconds and roughly every ten seconds thereafter. Returning to Figure 4.5, we see that those times correspond to times when the x-axis predictions and measurements are in agreement, each time with the prediction a downward slope. Although the disagreement between the x-axis predictions and measurements is large,

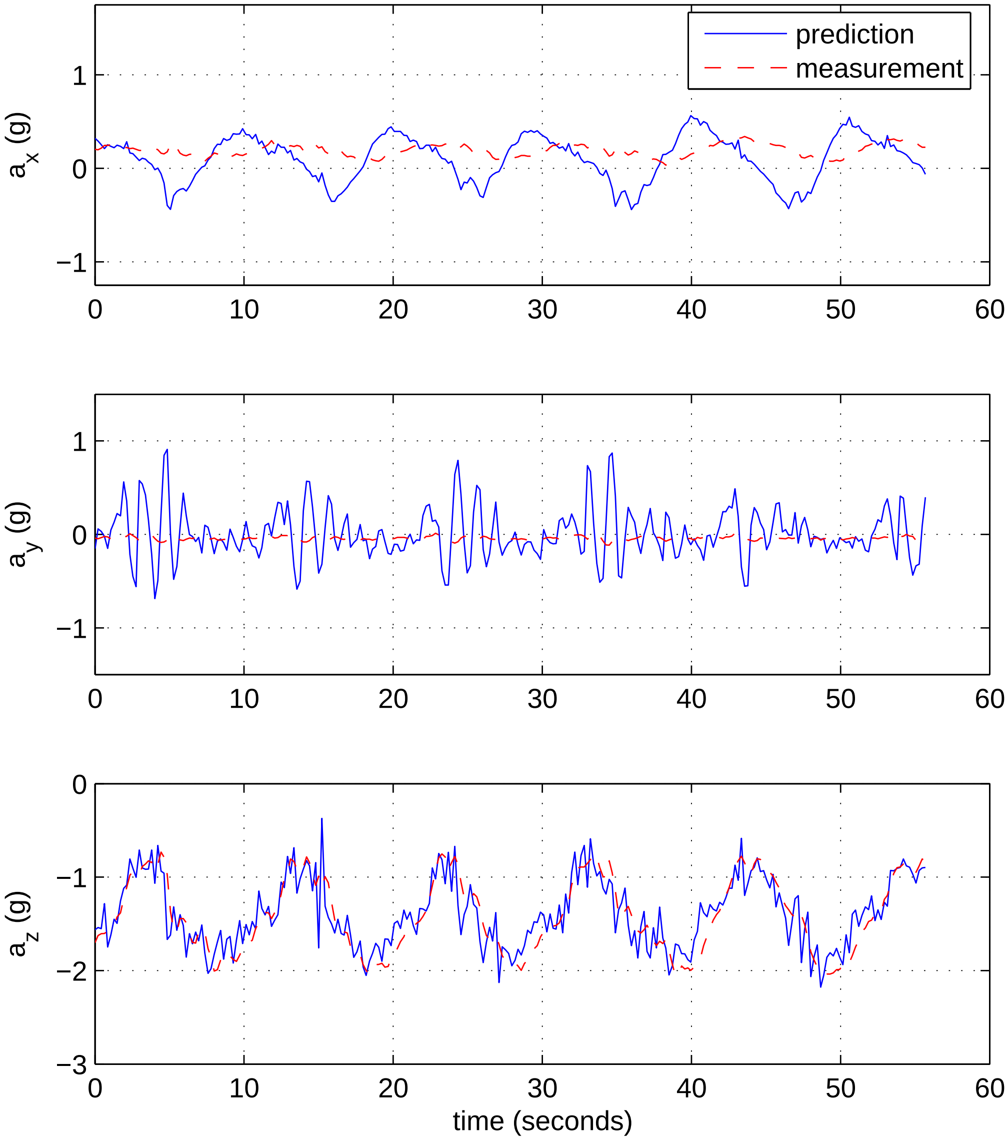

Figure 4.5: Accelerometer Predictions and Measurements During 15 Meter Radius Orbit

the gain scheduling portion of the algorithm correctly identifies when the comparison will be useful, and more importantly, when it will give erroneous information. The updates are sufficient at these times to keep the estimate stabilized, as the vehicle continued to fly the pattern with no noticeable degradation in performance after each

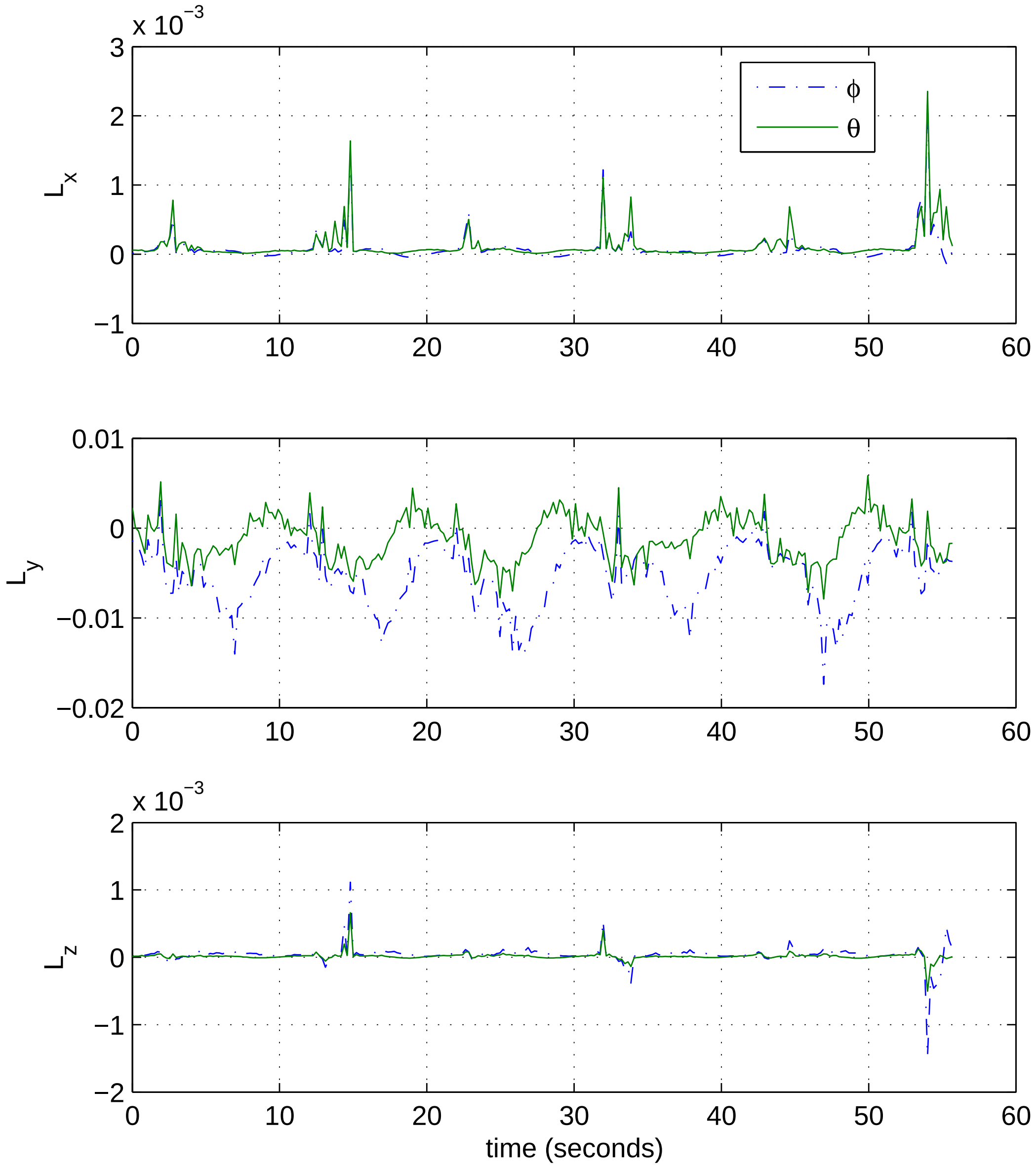

Figure 4.6: Sensor Correction Gains During 15 Meter Radius Orbit

orbit. The y and z axes show behavior consistent with the simulation results in Section 3.1, with good agreement on the z-axis, and the y-axis dominated by prediction noise rather than sensor noise.

4.2 Stage 2: Heading Estimation

In testing the heading observer, the vehicle was flown in a rectangular pattern. This data set was taken with the vehicle making right hand turns. Figure 4.7 shows that the experiment begins and ends with the vehicle on a Northbound heading, The heading data wraps while the vehicle is on a Southbound heading.

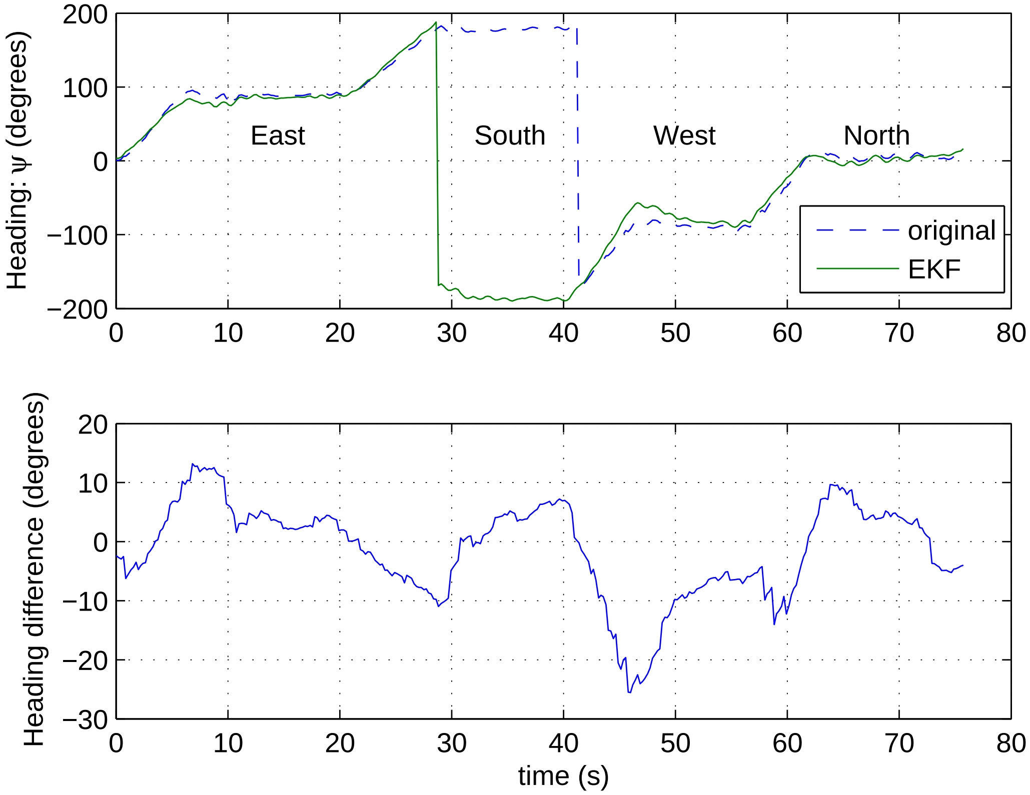

Figure 4.7: Heading Estimates During a Right-handed Rectangular Pattern

Again, in the absence of truth data, the difference between the EKF estimate and the default estimate is shown. The mean difference between the two estimates is less than nine degrees. In the absence of truth data, however, it is unclear which estimate is more correct at any particular time. By looking at the length of time spent on each leg of the pattern, one may surmise that a wind was present coming from a Northeastern direction, which would explain an overshoot in heading between the South and West headings. In the event that the wind is with the MAV, the MAV often overshoots it's desired ground track, since the ground track controller has no feed-forward wind compensation. After the overshoot, it makes sense that the MAV would take a heading North of West in order to rejoin the Westbound course.

Section 3.2 included a discussion on how gains in an Extended Kalman Filter may change sign depending on the value of the state. Figure 4.9 show the same behavior as the gains in Figure 3.11, except that they correspond with a square pattern rather than a round one. In both cases, the gains change appropriately with the estimates to allow the most useful magnetometer axes to be considered with the greatest weight in the update of the heading estimate. Again, the greater weight is applied when the sensors are near the center of their sensing ranges, rather than at their extremities, as these are the situations in which changes in sensor reading give the greatest sense in the change of state.

4.3 Stage 3: Position and Wind Estimation

One interesting possibility created by the EKF navigation filter over GPS smoothing is the ability to navigate for brief periods without the aid of GPS. To observe the effect of loss of GPS signal on the filter, a set of data was taken with the aircraft in a rectangular pattern, turning off GPS updates to the navigation filter midway through the experiment, with the vehicle at the far end of it's flight pattern. Instead of continuing the rectangle, the plane was then commanded to orbit a point 100 meters north of the home position.

The baseline algorithm is the GPS smoothing algorithm discussed in Appendix A continues to run uninterrupted. The GPS smoothing algorithm uses rate gyros to help smooth the estimate of position from the GPS. GPS ground track and groundspeed are also utilized. This is in contrast with the EKF observer, which uses airspeed and heading and uses GPS to make corrections.

Figure 4.10 shows a position plot of the vehicle in a right turn. GPS updates are happening during this segment. Arrows indicate the influence of the airspeed and

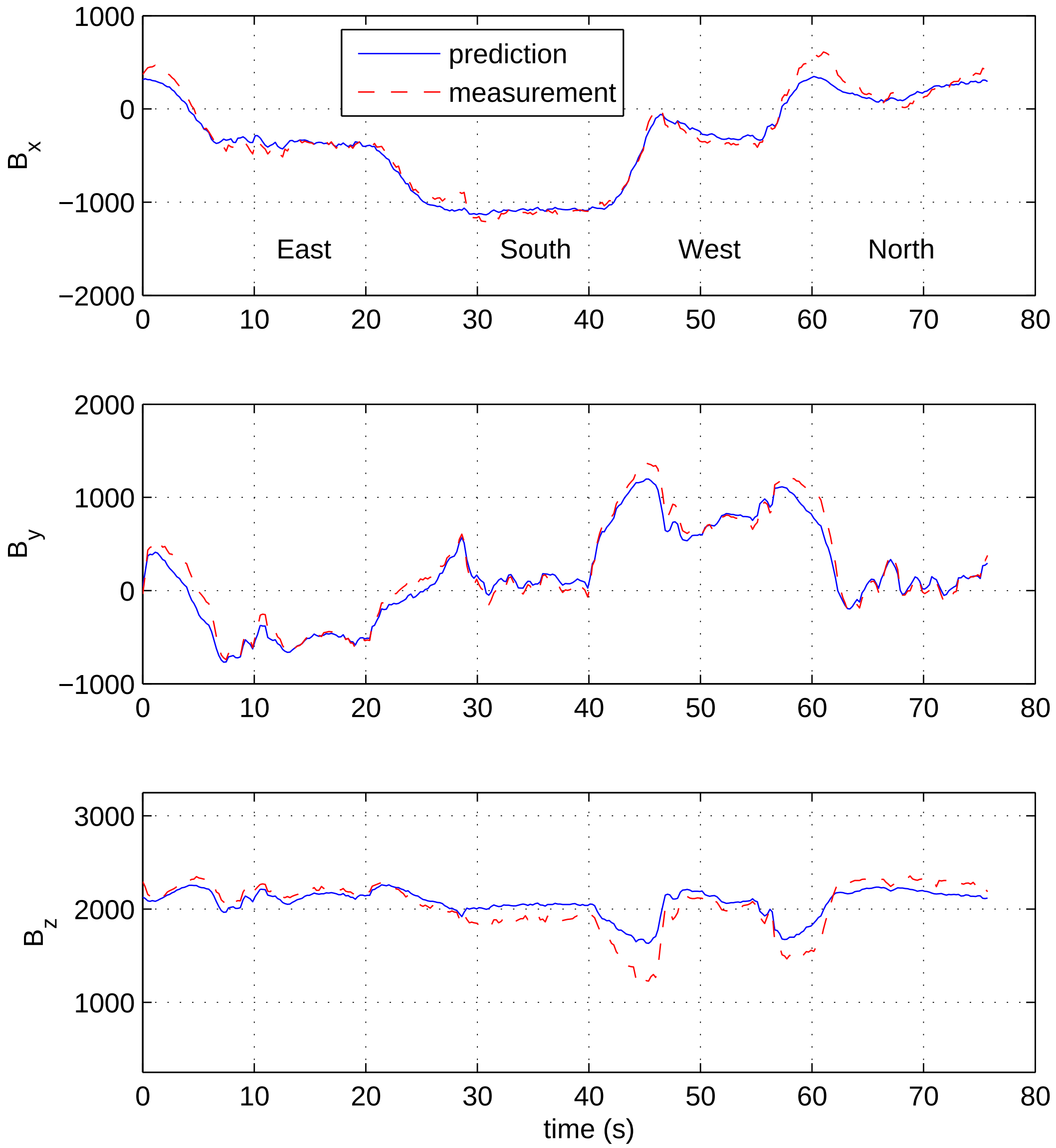

Figure 4.8: Magnetometer Predictions and Measurements During a Right-handed Rectangular Pattern

heading and the influence of wind on successive estimates. GPS updates sometimes causes a small jump in the estimate, where the GPS provides an estimate which makes a significant correction to the estimate. Jumps in the GPS smoothing algorithm estimate are also observable.

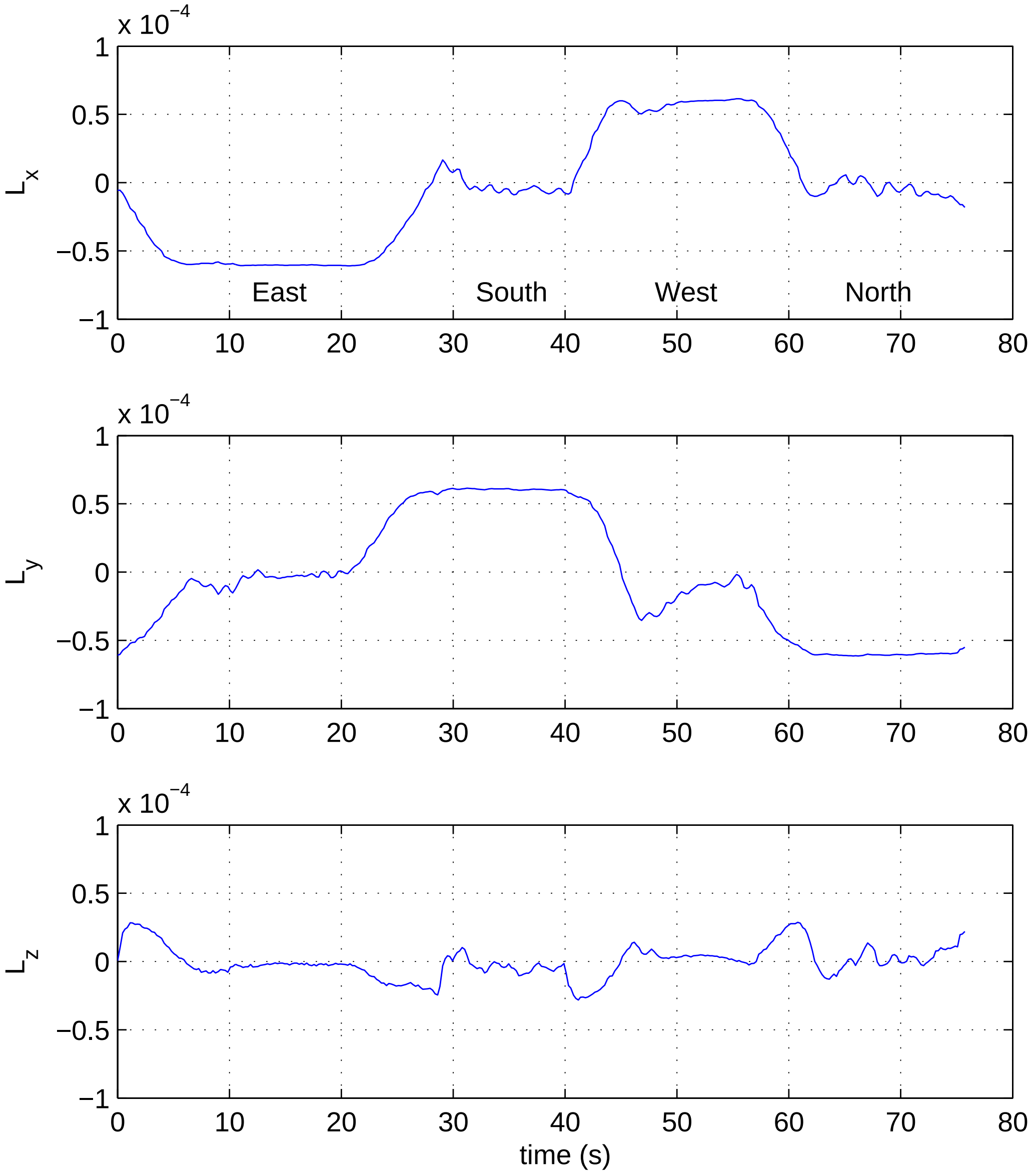

Figure 4.9: Heading Estimates During a Right-handed Rectangular Pattern

Figure 4.12 shows the position of the MAV in time, covering the entire time frame of the experiment. The plot of differences shows a correlation with heading in the difference between the original and EKF estimates. GPS updates periodically bring the EKF estimate closer to the default estimate, causing the sawtooth effect in

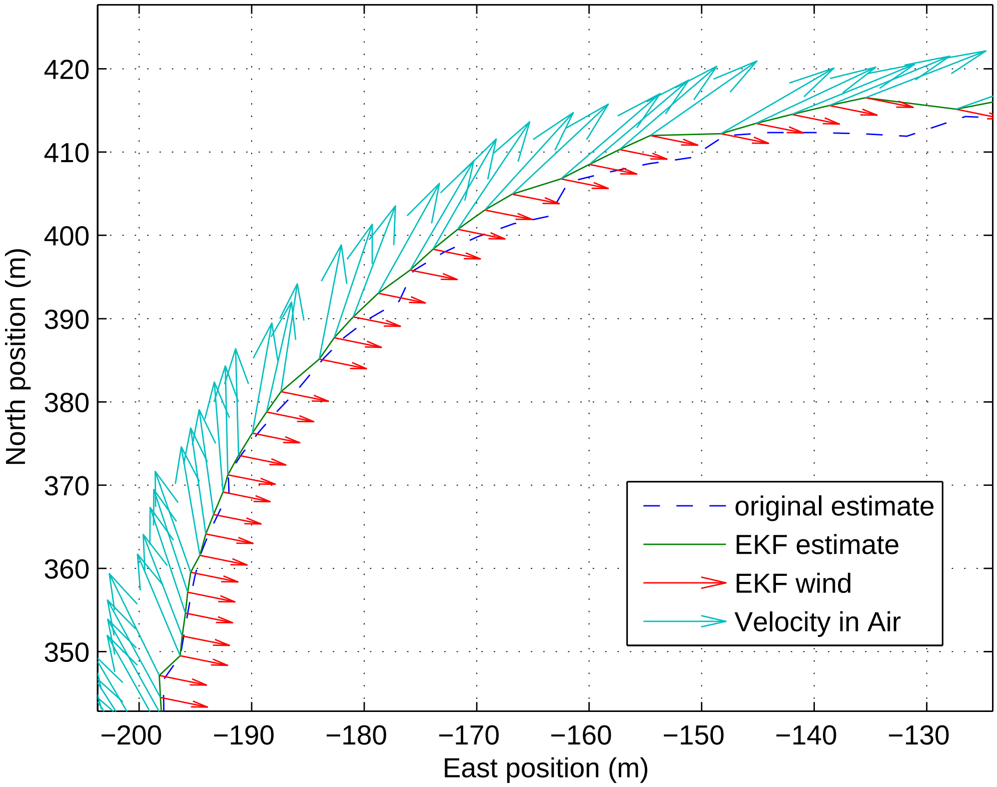

Figure 4.10: Position Estimate During a Segment of a Rectangular Pattern

the difference. The difference remains bounded, but could clearly benefit from a better measurement of airspeed and heading. The GPS updates to the EKF were switched off at about 36 seconds at which time the position estimate begins to diverge from the GPS smoothing estimate, which is continuing to update from the GPS. It appears that the airspeed estimate feeding the EKF is short, since the observer undershoots on the eastbound and southbound legs, but it is also interesting to note that shortly after the GPS updates were switched off, The default wind estimate, shown in Figure 4.13, reports a change in wind from two meters per second from the south, to four meters per second from the north, which, if true, would greatly increase the actual distance traveled on the southbound leg. The wind speed difference coresponds closely to the rate of divergence seen on the top graph of Figure 4.12. The EKF wind estimate in Figure 4.13 does not show the change in wind because the wind update requires GPS

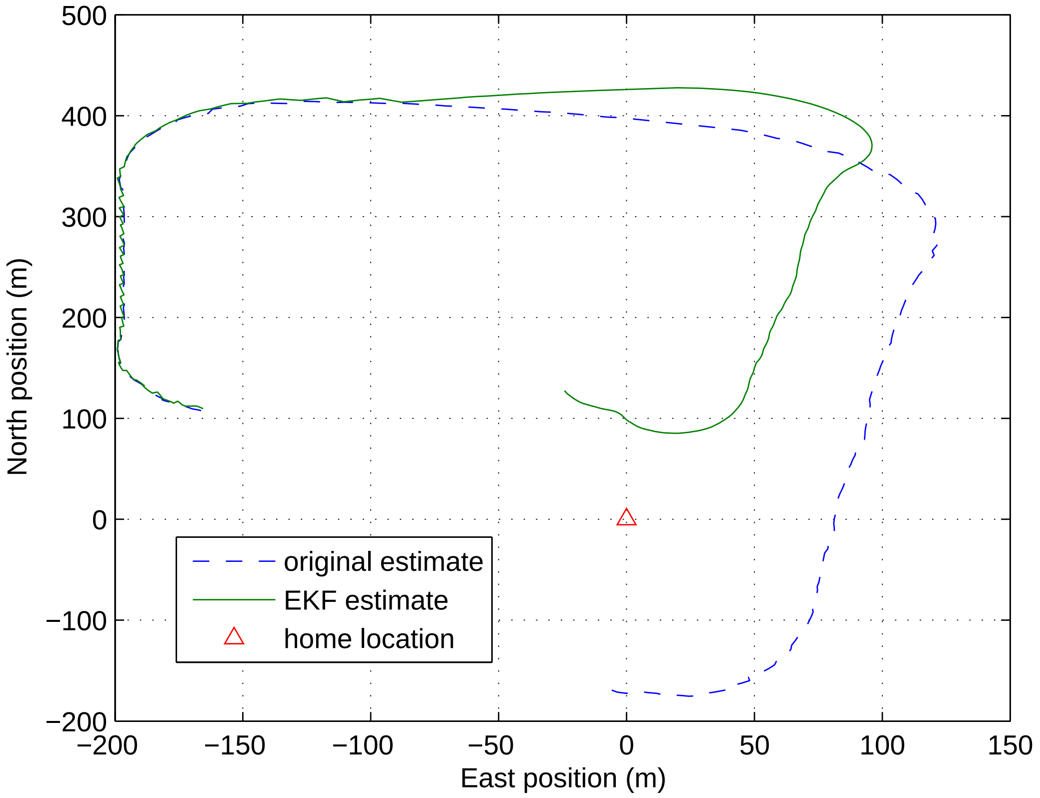

Figure 4.11: Position Estimates With GPS Updates to the EKF Stopped Mid-experiment

measurements to update. Since the wind change occurred after the GPS updates to the EKF were turned off, the EKF wind estimate does not show the change. Remember that the EKF wind estimate is tunable as well, it may be as sensitive or insensitive as desired, showing a general trend or a more sensitive response. The more sensitive the response, however, the more correlated the error will be to errors in airspeed and heading.

Supporting information to the navigation filter is shown in Figure 4.14. The heading estimates show a large difference on the North and Eastbound legs, with good agreement on the southbound legs. The plot of airspeed versus groundspeed show airspeed remaining relatively constant, with groundspeed being two to three meters per second slower than airspeed while Northbound, but being six to seven meters per

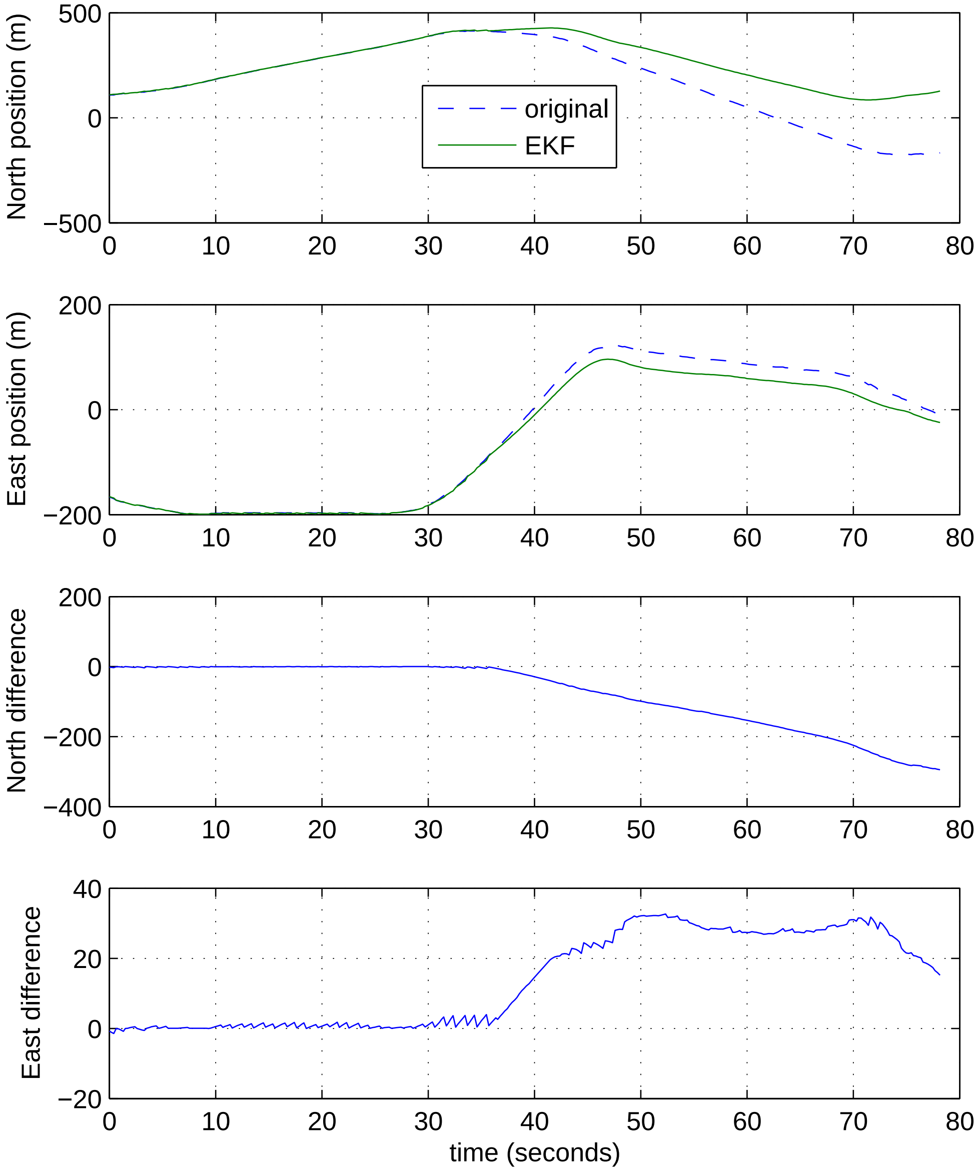

Figure 4.12: Position Estimates, Difference in Position Estimates in Time

second faster on the southbound portion, which is consistent with an increase of wind from the North.

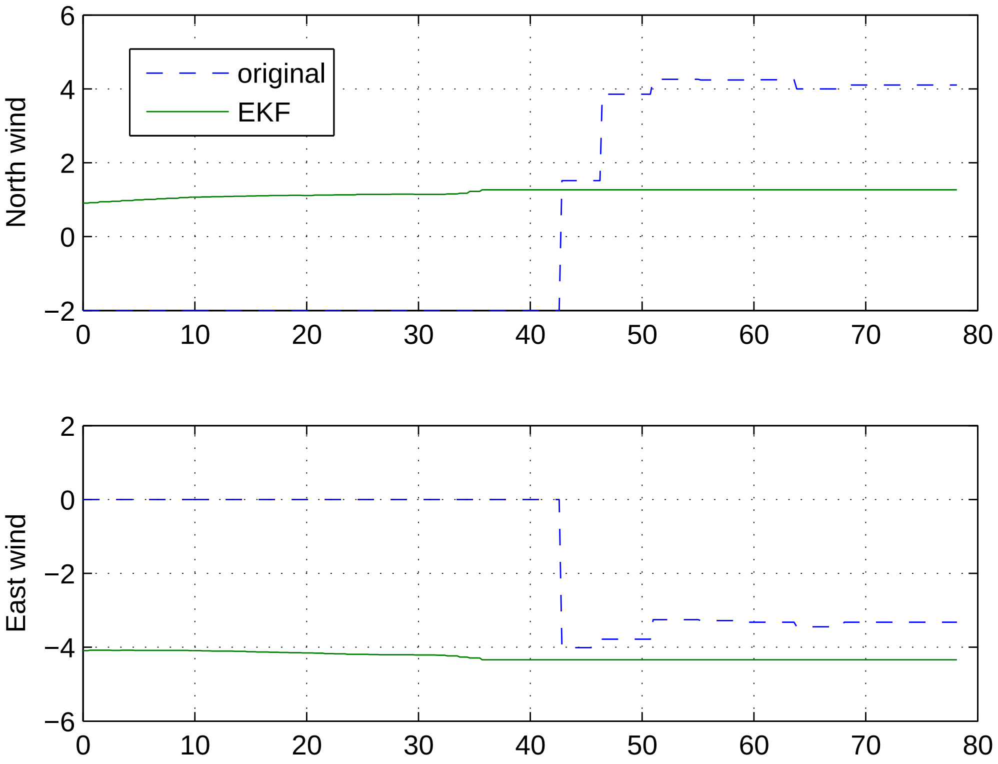

Figure 4.13: Wind Estimate While in a Rectangular Pattern

4.4 Summary of Flight Test Results

Each stage of the Cascaded filter structure was compared to results from an original algorithm detailed in Appendix A. Stage one, which estimates pitch and roll, has better performance in turns able to hold altitude while in a steeply banked turns. A small radius position hold orbit demonstrated the function of the sensor variance penalty. Stage one results are contained in Section 4.1. Stage two results were covered in Section 4.2, where it was shown that an effective heading estimate could be achieved without GPS measurements. The magnetometer-updated heading estimate agreed well with the original GPS based estimate. Operation without GPS measurements is one of the chief benefits of Stage 3. While the navigation EKF is sensitive to errors in airspeed and heading measurements, it has the ability to

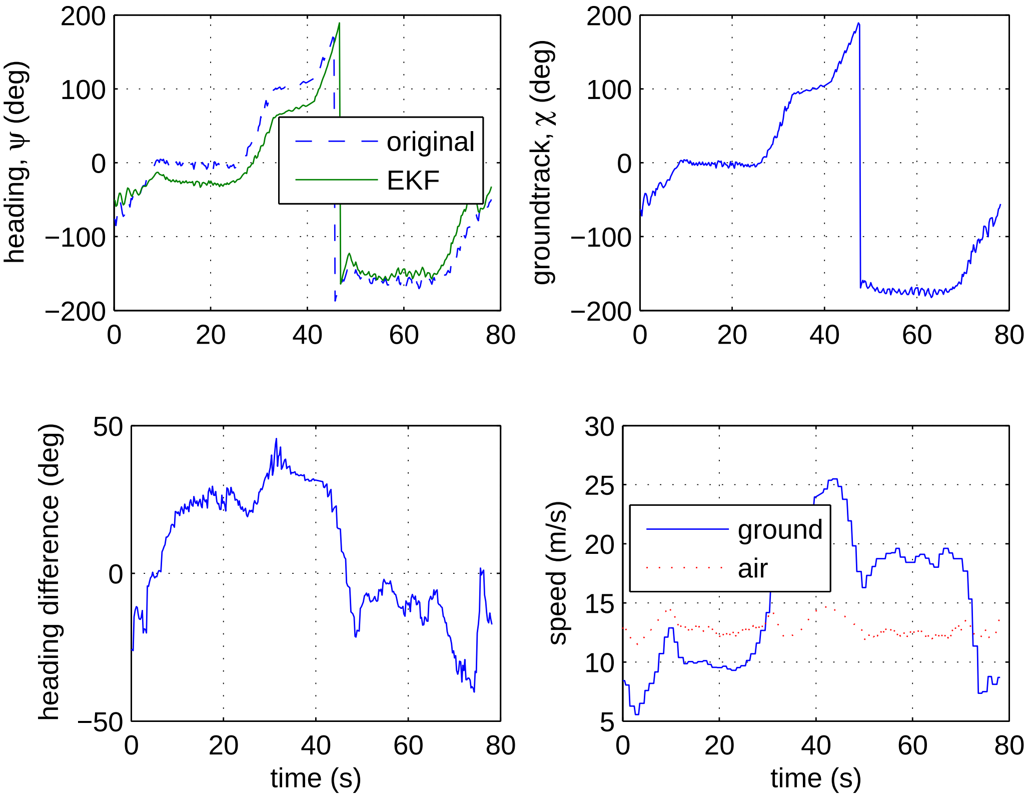

Figure 4.14: Observer Inputs and Helpful GPS Ground-track and Ground-speed Estimate from a Rectangular Pattern

operate without GPS updates, where the original state estimate would be completely lost. Results for stage three are contained in Section 4.3.

Chapter 5

Conclusions and Future Work

5.1 Conclusions

Continuing improvement of MAV state estimation has benefits to the performance of MAV missions including sensing applications and expanding operational capabilities of the vehicles. One typical mission profile involves flying to a target area, identifying the target, and, while orbiting the target using onboard sensors, such as a cameras, to locate the target in World coordinates. Accuracy of state estimates directly affects the ability of localization programs to resolve sensor images to World coordinates quickly and accurately. The ability of the MAV to maneuver energetically and effectively is limited by the capabilities of the vehicle, and also the capabilities of the estimation. By improving the estimation algorithm's ability to deal with energetic dynamics, the control algorithms are more able control effectively through the desired maneuvers. Also valuable is the ability of a vehicle to navigate without GPS. Some environments may deny a sufficient GPS signal, or in the event of sensor failure, the MAV has a way to navigate to a position as close to home as possible. All of these capabilities are strengths of the cascaded state estimation scheme set forth in this work.

5.1.1 Pitch and Roll Estimation

Simulation and flight test results show that the the EKF attitude observer is more accurate in transient and steady state performance over the VGO. The VGO has no dynamic correction for the accelerometer readings, which appears to be responsible for 5.5 degree roll, and 2.5 degree pitch errors in simulation, shown in Section 3.1. In each test, the EKF pitch and roll was within a degree of accuracy for the duration of the test. In flight testing, feedback control in a steep bank using the EKF kept resulted in a stable turn with altitude in control, where VGO feedback caused the vehicle to oscillate in and eventually lose altitude.

In considering the hardware test results, it becomes clear that the mean error of sensors is more important than noise. Hardware results in Section 4.1, show that the x accelerometer measurement and predictions was less noisy than the y, but still required modification of the algorithm, because it had unmodeled dynamics, which causes poor agreement of the predictions and measurements. The y-axis was noisy, but required no modification of the all ills could be cured with more complete model information.

5.1.2 Heading, Position and Wind Estimation

While the EKF heading estimate appears to be better than the default estimate, it is unknown which is better in flight, since the flight data relies on a magnetic field estimate determined in flight, but the two agree with a root mean square difference of approximately eight degrees. The principle advantage of the EKF heading estimate is that it is independent of the GPS measurement, and can therefore be used as a basis for dead reckoning navigation in subsequent stages.

The EKF navigation and wind estimate performs comparably to GPS smoothing and wind estimation. The EKF is sensitive to errors in airspeed measurements and heading estimates. Hardware results in Section 4.3 show GPS updates making corrections to both navigation schemes of approximately the same magnitude. It should be noted that the rate of convergence of the wind estimate is more or less arbitrary, and can be traded off with noise sensitivity. The results in Section 4.3 represents a relatively slow rate of convergence, which will indicate general trends rather than providing a time history of wind on the scale necessary to identify short disturbances such as gusts. This navigation EKF has the advantage that it can operate without the aid of GPS and continue to make sensible updates of its position, which may allow the MAV to make brief navigation in GPS denied areas, or return to a position close to home in the event of a GPS failure.

5.2 Future Work

The following are some additions and improvements which may be pursued in the development of estimation algorithms for MAV's. The first is a modification to the attitude estimation which eliminates some of the restrictive assumptions in its derivation, making it more useful in more flight situations. Also included are some ideas for streamlining computation with the end goal reducing the processor time dedicated to state estimation, important for cases in which processor cycles are placed at a premium.

5.2.1 Assumptions Revisited

Likely the most restrictive simplifying assumption made in the derivation of this filter is that the climb angle is close to the angle of attack which is used only in calculation of cross acceleration terms. The only flight mode in which this assumption is at all a limiting factor is climbing and descending turns. This assumption can be removed by using information on the rate of climb, derived from the barometric pressure sensor, which will give a notion of the actual climb angle, γ. The quality of this information must be evaluated, as it will very likely be noisy and delayed, since it represents a numeric differentiation on an already noisy sensor. Details of the revised filter can be found in Appendix B.

5.2.2 Variation: Tuning Constant Covariance Matrix

The nature of the covariance matrix, $\mathbf{P}$, constrains it to be positive definite and symmetric. For a two by two matrix, this means that the terms on the diagonal must be positive, and the determinant must be greater than zero. A variant on the implementation of the EKF estimation scheme may take advantage of the fact that the time and measurement updates each happen at regular intervals. If a range of covariance values are observed for typical maneuvers, the dynamic covariance matrix may be replaced with a static one, constrained as described below. While this may sacrifice the rate of convergence, the computational overhead associated with propagating the covariance matrix would be eliminated.

The matrix $\mathbf{P}$ has the form

$$\mathbf{P} = \begin{bmatrix} P_{11} & P_{12} \\ P_{12} & P_{22} \end{bmatrix}.$$

The matrix elements may be manually tuned subject to the constraints

$$P_{11} > 0$$
$$P_{22} > 0$$

and

$$P_{12} < \sqrt{P_{11}P_{22}}$$

using the results from a record of dynamic covariance data as a starting point. Since P_{12} must satisfy the constraint for the matrix to remain positive definite it can be chosen using the parameter, τ, as shown below, retaining positive definite property, which requires that

$$P_{12} = \tau P_{11}P_{22}$$

and

$$0 < \tau < 1.$$

5.2.3 Computational Streamlining

In addition to the modification described in Section 5.2.2, there are several other modifications to this state estimation structure which show promise in streamlining the computation and possibly speeding the algorithms' execution. For the heading estimate in stage two, a significant amount of time is spent in querying the sensor and waiting for it to respond with a measurement. Each time this cycle is repeated, all three sensor axes are queried, each with associated delay. When this sensor information is processed, each axis is weighted according to its usefulness in updating the estimate. At this time, the sensor is queried at a quasi-fixed interval, regardless of the state of the observer. Depending on the state of the estimate, these estimates may not even be used, such as when the sensor is near a local maximum and deviation in the measurement indicates a turn to either the left or the right; at that time the gain on that measurement will be low, diminishing its effect on the estimate. At other times, the variance of the estimate may be low and a measurement may not make a significant change the estimate. In these situations, it may be useful to put the heading observer in charge of querying the magnetometer, choosing what axis it uses based on Kalman gain $\mathbf{L}$, linearization of output equations $\mathbf{C}$, or even the state. This modification may also be sensible to the overall variance, where the noise model grows the uncertainty on the state relatively slowly, the sensor may be queried less often. This modification may significantly reduce the overhead associated with stalling the processor while waiting for the sensor to make and return a measurement.

The PNI magnetometer had the additional feature that it can be queried at different resolutions, the coarser measurements taking less time. If this information could be collected and tabulated, with its associated noise characteristic, it could work to the advantage of the observer by choosing the axis and query level which will minimize the state variance most effectively.

A similar justification may be used for disallowing GPS updates on orthogonal position and wind states. Several operations can be eliminated by not calculating gains for the GPS north measurement update on the east position and east wind. The filter regularly ignores these types of updates in any case by calculating a very small gain.

Observing the Kalman gains may offer other streamlining hints which may not have been noticed during the derivation of the filters. The x accelerometer measurement of the attitude filter is generally not beneficial to the roll estimates, since a change in roll angle at any attitude will not change the gravity vector on the x-axis. Herein lies another opportunity for trimming some operations thereby speeding computation.

Appendix A

Original State Estimation Algorithms

This chapter contains descriptions of the original state estimation algorithms implemented on the Kestrel$^{\text{TM}}$autopilot. Pitch and roll are estimated by the Variable Gain Observer Attitude Estimation Algorithm. Posistion is estimated by the GPS smoothing alogrithim, and wind and heading are estimated by the Wind estimation

A.1 Attitude Estimation with the Variable Gain Observer

The Variable Gain Observer (VGO) is a relatively simple algorithm and has been useful for simple pitch and roll control. The observer dynamics are sufficiently stable for feedback control for the waypoint navigation problem, where pitch and roll angles are limited.

A.1.1 Formulation

The VGO uses a kinematic model to update pitch and roll angles with body frame angular rate measurements as inputs, see Equation A.1. At the same time, three-axis accelerometers used as an inclinometer compute an alternate pitch and roll angle, using accelerometer information only. The main pitch and roll estimate are corrected by the inclinometer estimate which is weighted inversely proportional to the sum of the angular rates, effectively putting less trust on the accelerometer measurements when the vehicle is yawing, pitching or rolling. Because there is no correction for centripetal effects, bias errors eventually work into the estimation during sustained turns.

A.1.2 Kinematic (Time) Update

The expression

$$\begin{bmatrix} \dot{\hat{\phi}} \\ \dot{\hat{\theta}} \end{bmatrix} = \begin{bmatrix} 1 & \sin\hat{\phi}\tan\hat{\theta} & \cos\hat{\phi}\tan\hat{\theta} \\ 0 & \cos\hat{\phi} & -\sin\hat{\phi} \end{bmatrix} \begin{bmatrix} p \\ q \\ r \end{bmatrix} \tag{A.1}$$

relates body frame angular rates to changes in Euler angles. Using the angular rates as inputs, these equations are numerically integrated to update the estimates. This estimation scheme includes only roll (ϕ) and pitch (θ) angles as states. The change of heading in terms of the body frame angular rates is omitted.

A.1.3 Accelerometer Updates

Using the accelerometers on each body frame axis as an inclinometer and neglecting dynamic effects, the roll and pitch are calculated as

$$\phi_a = -\tan^{-1}\left(\frac{a_y}{-a_z}\right) \tag{A.2}$$

and

$$\theta_a = \tan^{-1}\left(\frac{a_x}{-a_y\sin\phi - a_z\cos\phi}\right). \tag{A.3}$$

In this scheme, error is defined as

$$\tilde{\phi} = \phi_a - \hat{\phi}$$

and

$$\tilde{\theta} = \theta_a - \hat{\theta}$$

or the difference between the accelerometer measurement and the current observer estimate. The observer measurement is corrected by the error multiplied by a gain chosen to be inversely proportionally to the sum of the absolute values of the body frame angular rates. When rate measurements are high, there will be a dynamic influence on the accelerometers, so the weighting of the accelerometer measurements is reduced. In summary, the accelerometer measurement correction is given by

$$K = \frac{1}{1 + k_1(|p| + |q| + |r|)}, \tag{A.4}$$

$$\hat{\phi}^+ = \hat{\phi}^- + K k_2 \tilde{\phi} \tag{A.5}$$

and

$$\hat{\theta}^+ = \hat{\theta}^- + K k_3 \tilde{\theta}, \tag{A.6}$$

where the parameters k_1, k_2 and k_3 are user selectable gains.

A.2 Position Estimation with GPS Smoothing

GPS is uses as the sole source of position information in this algorithm. At each update, the current GPS measurement is copied to the position estimate, and the GPS ground track and ground speed measurements are used in conjunction with rate gyro updates to predict subsequent positions until the next measurement update.

A.2.1 GPS Smoothing Kinematic Update

Between GPS measurements, the ground track angle is updated using body frame angular rate gyros q and r. A running total of the turn made since the last update is kept as $\Delta\chi$. The position estimates are updated using the current estimate of groundspeed and ground track. Between updates from the GPS, we smooth with

$$\dot{\hat{\chi}} = q\frac{\sin\phi}{\cos\theta} + r\frac{\cos\phi}{\cos\theta} \tag{A.7}$$

$$\Delta\dot{\chi} = \dot{\hat{\chi}} \tag{A.8}$$

$$\dot{\hat{P}}_N = \hat{V}_g \cos\chi \tag{A.9}$$

and

$$\dot{\hat{P}}_E = \hat{V}_g \sin\chi. \tag{A.10}$$

A.2.2 GPS Smoothing Measurement Update

When a GPS measurement is received, the new measurements replace the old position estimates. GPS ground track and ground speed measurements are typically based on the time and space difference between the current and previous position measurements and therefore represent an average for the period between the two measurements. These angle and speed measurements, representing an average, are therefore delayed. To attempt to compensate for these delays, the trend from the last segment is extended to the current speed and track estimates in a simple manner. When information is received from the GPS, we use

$$\hat{P}_N = GPS_{N_k} \tag{A.11}$$

$$\hat{P}_E = GPS_{E_k} \tag{A.12}$$

$$\hat{V}_g = GPS_{V_k} + \left(GPS_{V_k} - GPS_{V_{k-1}}\right) \tag{A.13}$$

$$\hat{\chi} = GPS_\chi + \Delta\chi/2 \tag{A.14}$$

and

$$\Delta\chi = 0 \tag{A.15}$$

First, whatever the difference in ground speed between the last and current measurement is added to the current speed measurement. For ground track angle, the current delayed measurement plus half of the turn history from the last segment is used, and the turn history is reset. This smoothing algorithm is well suited for straight path segments and constant radius turns.

A.3 Wind and Heading Estimation

This section outlines a method for determining the wind vector based on solving an over-determined set of nonlinear equations. This system of equations is continually updated with new data sets as the airplane reports new telemetry, and thus provides a continuously updated and improving estimate of the current wind conditions over the duration of the MAVs flight.

The system of nonlinear equations stems from the basic relationship between winds peed, ground speed, and airspeed as shown in Figure A.1.

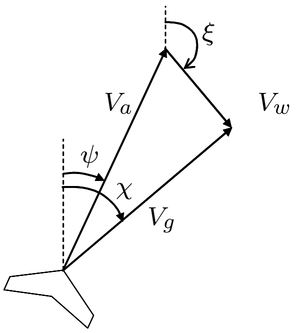

Figure A.1: Relationship Between Ground, Air, and Wind Velocities.

The relationship shown in Figure A.1 can be resolved in the direction of χ as

$$V_g = V_a \cos\left(\psi - \chi\right) + V_w \cos\left(\xi - \chi\right). \tag{A.16}$$

Groundspeed and course as determined by Equation (A.16) for a commanded airspeed of 18 m/s and a windspeed of 10 m/s out of the south is shown in Figure A.2.

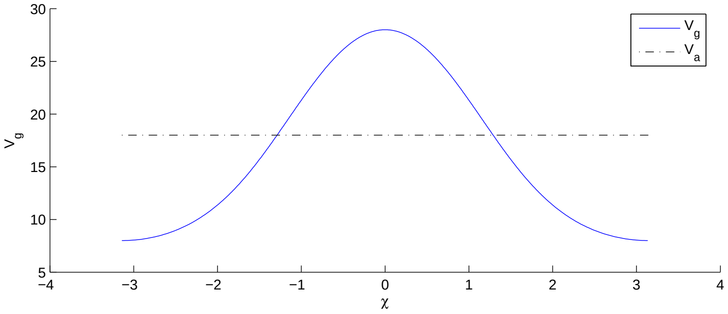

Figure A.2: $V_w = 10$ m/s, $\xi = 0.0$.

In Equation (A.16) the quantities V_g, V_a, and χ are measurable quantities using GPS and a pressure sensor connected to a pitot probe. The quantities ψ, V_w, and ξ are not directly measurable with these sensors. The problem is to solve Equation A.16 for V_w and ξ using measurements of V_g, V_a, and χ.

The law of cosines,

$$\cos(A) = \frac{-a^2 + b^2 + c^2}{2bc}, \tag{A.17}$$

can be used to reduce the number of unknowns in Equation A.16 to ξ and V_w, giving us

$$V_g = \left(\frac{V_g^2 + V_a^2 - V_w^2}{2V_g} \right) + V_w \cos(\xi - \chi). \tag{A.18}$$

Collecting all the terms with unmeasurable values on the right hand side of the equation yields

$$V_g^2 - V_a^2 = -V_w^2 + 2V_g V_w \cos(\xi - \chi). \tag{A.19}$$

If a minimum of two different headings are flown Equation A.19 can be used to form a system of two nonlinear equations in two unknowns (V_w and ξ). This system of equations can then be solved (Assuming a solution exists) for the wind speed and wind direction that exactly explains the data. Because the data is noisy it is preferable to collect numerous data points to form an over-determined system of nonlinear equations. This set of equations can then be solved using a nonlinear solver to find the winds peed and wind direction that best explains the data collected. This solution can be obtained by minimizing the objective function

$$\sum_{i=0}^{n} \left(V_{g_i}^2 - V_{a_i}^2 + V_w^2 - 2V_{g_i}V_w \cos\left(\xi - \chi_i\right)\right)^2 . \tag{A.20}$$

The windspeed, V_w, and wind direction, ξ, which minimize the objective function in Equation (A.20) represent the least squares estimate of the wind vector given the data vectors $\mathbf{V}_g$, χ, and $\mathbf{V}_a$.

A.4 Nonlinear Solver

The objective function of Equation (A.20) is solved using a Quasi-Newton solver based on the method of Broyden, Fletcher, Goldfarb, and Shanno (BFGS). Using the BFGS algorithm with a fixed number of iterations, six, and an eleven iteration line search showed good convergence to the true optimum given arbitrary starting conditions. A plot of the required execution time for the algorithm to run through six iterations with an eleven step line search for various numbers of data points is shown in Figure A.3. Even for extremely large numbers of data points (≈ 500) the solution is reached in less than four milliseconds. These tests were run on a laptop computer with 3.2 GHz Intel Pentium processor.

Actual execution time for the algorithm can be reduced drastically since it is not necessary to solve the system of equations from an arbitrary starting point over consecutive iterations of the algorithm. Because the wind is assumed to be slowly varying successive calls to the nonlinear solver can use past solutions as good starting points for the solver.

Using this method, each time a significant number of new data points is received the nonlinear solver can be run, beginning at its last solution. Using the past solution as the starting point for the new solution usually results in convergence in only one to two iterations.

Given this performance, it would not be too computationally burdensome to find a new solution for the wind vector every time a new telemetry sample is received. However, computational burden can be further reduced, without loss of accuracy,

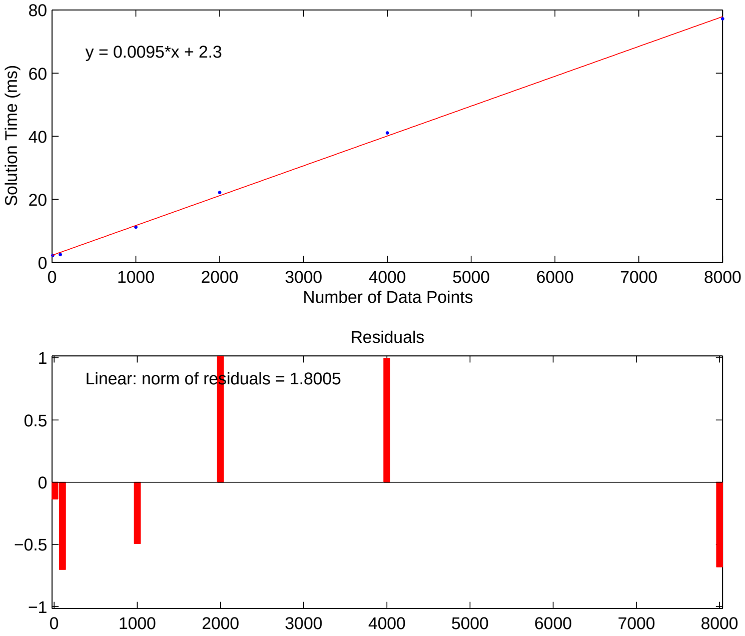

Figure A.3: Execution Time vs. Number of Data Points for the Solution of Equation (A.20).

by separating the datapoints into bins by their course measurement. The solver can then be used to solve the system of equations determined by the most recent datapoints in each of the bins. In this case, instead of optimizing over all previous data points, the solver optimizes over the most recent set of data points which form a good representation of the actual signal over the entire signal space.

Requiring a certain minimum spread in course between data points also avoids solving a set of equations which is ill-conditioned and thus very sensitive to the noise inherent in the measurements. Using the most recent data points and discarding old data points reduces demands on memory and results in a solution that is more robust to changing wind conditions. We currently use eighteen bins separated by course. We use the two most recent data points from each of the bins to give us a maximum of 36 data points which are actually used in the solution of the wind vector (this number of data points is probably significantly higher than what is actually necessary to arrive at a good solution for the wind vector). We update our estimate of the wind vector every fifteen data points, or roughly every five seconds.

Appendix B

Inclusion of Climb information in Attitude EKF

This modification of the attitude observer described in Section 2.6 is more general, eliminating the level flight assumption by using climb information from the barometric pressure sensor. In this treatment, kinematic update equations remain unaffected, coming directly from Equation 2.4. Output equations, however, will be reconstructed using the new assumptions, which are as follows:

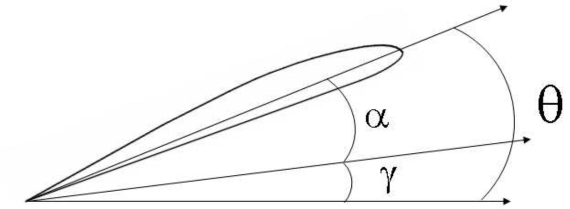

Figure B.1: Relationship of Pitch, Angle of Attack and Flight Path Angles

Instead of assuming that the angle of attack is equal to the pitch angle, we define angle of attack as the difference between pitch angle and climb angle,

$$\alpha = \theta - \gamma. \tag{B.1}$$

Again, we assume zero side slip,

$$\beta \approx 0. \tag{B.2}$$

and also that linear accelerations are small,

$$\begin{bmatrix} \dot{u} \\ \dot{v} \\ \dot{w} \end{bmatrix} = \mathbf{0}. \tag{B.3}$$

Substituting Equation B.1 and Equation B.2 into the alternate expression for component airspeeds in Equation 2.22 gives us

$$V_{air} \begin{bmatrix} \cos(\theta - \gamma) \\ 0 \\ \sin(\theta - \gamma) \end{bmatrix}. \tag{B.4}$$

Since climb angle is not directly available, we may simplify implementation by using a trigonometric identity which obviates the need to find the difference in angles and allows us to work directly with sines and cosines of the climb angle, giving us

$$\begin{bmatrix} u \\ v \\ w \end{bmatrix} = V_{air} \begin{bmatrix} \cos\theta\cos\gamma + \sin\theta\sin\gamma \\ 0 \\ \sin\theta\cos\gamma - \cos\theta\sin\gamma \end{bmatrix}. \tag{B.5}$$

The sine and cosine of climb angle can be expressed in terms of airspeed and climb rate, which is known information. We will use

$$V_{air}\sin\gamma = \dot{h} \tag{B.6}$$

and

$$V_{air}\cos\gamma = \sqrt{V_{air}^2 - \dot{h}^2}. \tag{B.7}$$

In the development of the output equations, we will use the sine and cosine of the pitch angle in calculating the gravity portion of the acceleration vector, along with the approximation of component velocities in Equation B.5. For our sensor model outputs, Equation 2.5 is now approximated by

$$\begin{bmatrix} a_x \\ a_y \\ a_z \end{bmatrix} = \begin{bmatrix} \frac{qV_{air}(\sin\theta\cos\gamma - \sin\gamma\cos\theta)}{g} & + & \sin\theta \\ \frac{rV_{air}(\cos\theta\cos\gamma + \sin\theta\sin\gamma) - pV_{air}(\sin\theta\cos\gamma - \sin\gamma\cos\theta)}{g} & - & \cos\theta\sin\phi \\ \frac{-qV_{air}(\cos\theta\cos\gamma + \sin\theta\sin\gamma)}{g} & - & \cos\theta\cos\phi \end{bmatrix}. \tag{B.8}$$

These expressions for accelerometer model output are the principle difference between this filter implementation and the filter described in Section 2.6. Equation B.8 is complicated compared to the output from Equation 2.26, but offer some advantage in climbing turn situations. However this advantage must be weighed against the extra computational burden.

The assumptions in this case, while more general than those in Section 2.6 still do not capture the true nature of angle of attack. For example, if the vehicle is banked, it could be experiencing a high angle of attack with a zero pitch and zero climb angle. Again, the merits of taking a more general approach must be weighed in terms of computational cost and performance benefit.

B.0.1 Revised Filter Summary

First-stage state variables, inputs and outputs are

$$\mathbf{x} = \begin{bmatrix} \phi \\ \theta \end{bmatrix} \qquad \mathbf{u} = \begin{bmatrix} p \\ q \\ r \\ V_{air} \end{bmatrix} \qquad \text{and} \qquad \mathbf{y} = \begin{bmatrix} a_x \\ a_y \\ a_z \end{bmatrix}.$$

The EKF time update including the kinematic state update, linearization of the state update, and covariance matrix update is precisely the same as the original attitude EKF described in Section 2.6 (See Equation 2.20 and Equation 2.21). The sensor update equations for the revised attitude estimator are now

$$\mathbf{h}(\mathbf{x},\mathbf{u}) = \left[\begin{array}{ccc} \frac{q}{g}(\sin\theta\sqrt{V_{air}^2 - \dot{h}^2} - \cos\theta\dot{h}) & + & \sin\theta \\ \frac{r}{g}(\cos\theta\sqrt{V_{air}^2 - \dot{h}^2} + \sin\theta\dot{h}) - \frac{p}{g}(\sin\theta\sqrt{V_{air}^2 - \dot{h}^2} - \cos\theta\dot{h}) & - & \cos\theta\sin\phi \\ \frac{-q}{g}(\cos\theta\sqrt{V_{air}^2 - \dot{h}^2} + \sin\theta\dot{h}) & - & \cos\theta\cos\phi \end{array}\right] \tag{B.9}$$

and

$$C = \frac{\partial\mathbf{h}(\mathbf{x},\mathbf{u})}{\partial\mathbf{x}} = \left[\begin{array}{cccc} 0 & \frac{q}{g}(\cos\theta\sqrt{V_{air}^2 - \dot{h}^2} + \dot{h}\sin\theta) & + & \cos\theta \\ -\cos\theta\cos\phi & \frac{-r}{g}(\sin\theta\sqrt{V_{air}^2 - \dot{h}^2} - \dot{h}\cos\theta) - \frac{p}{g}(\cos\theta\sqrt{V_{air}^2 - \dot{h}^2} + \dot{h}\sin\theta) & + & \sin\theta\sin\phi \\ \cos\theta\sin\phi & \frac{q}{g}(\sin\theta\sqrt{V_{air}^2 - \dot{h}^2} - \dot{h}\cos\theta) & + & \sin\theta\cos\phi \end{array}\right]. \tag{B.10}$$

The expression in Equation B.9 includes substitutions from Equation B.6 and Equation B.7. It may be desirable to precalculate $V_{air}\sin\gamma$ and $V_{air}\cos\gamma$ for the implementation, which are expressed in terms of climb rate, which is the available informatoin.

Appendix C

Airborne Magnetic Field Determination

C.1 Magnetometer Calibration Data

The MAV with the PNI MicroMag three-axis magnetometer was installed and flown in a large cross shaped pattern, 600 meters long on legs aligned in cardinal directions at 100 meters altitude. Once established on heading, magnetometer data was taken, along with roll pitch, and default heading estimates from the Kestrel$^{\mathrm{TM}}$autopilot. Two sets of data were taken for each cardinal direction, yielding eight total sets. This data was then rotated in three dimensions to determine the ambient magnetic field as measured by the sensor. The rotation is given by

$$\hat{\mathbf{B}}_0 = \mathbf{R}^{-1}(\phi, \theta, \psi)\mathbf{B}. \tag{C.1}$$

Assuming the total magnetic flux is constant for the relatively small geographic area of interest, regardless of vehicle orientation, we assume that the magnetic flux is the same. By comparing runs from opposite headings, an estimate of x and y axis sensor biases were made. These new biases were applied to the data sets, and the earth frame magnetic field was estimated again from Equation C.1 for each set, yielding a much better agreement between data sets. A bias for the z axis was determined by perturbing the value of the bias and observing the effect on the variance of the norm of the estimated earth frame magnetic field vector. A bias was chosen which minimized the variance.

The data in Figure C.1 represents a single data collection run on a Eastbound heading. The data labeled 'sensor' is the raw data collected from the sensor and the data labeled B_0 is the same data with the estimated sensor biases removed, then

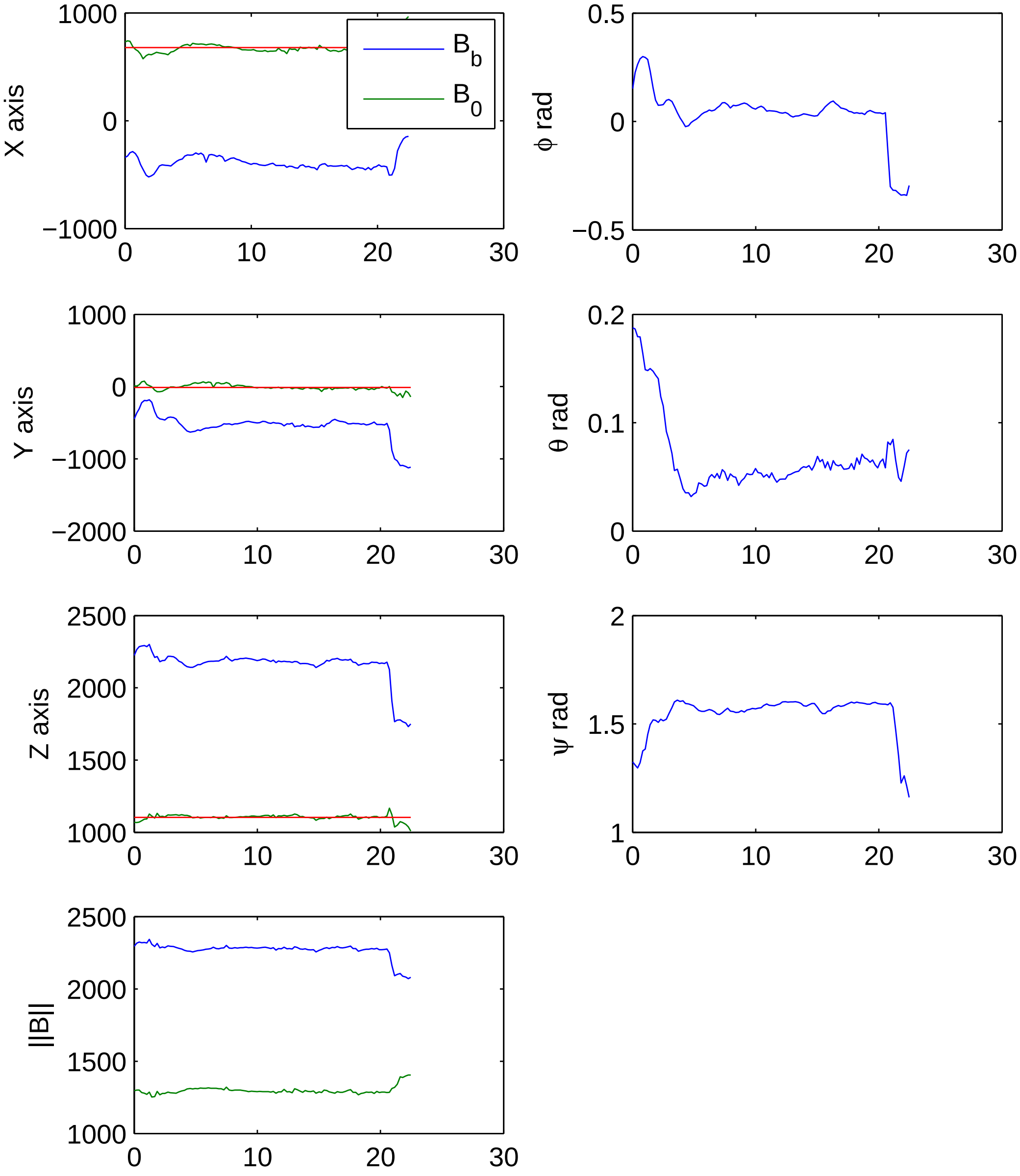

Figure C.1: Calibration Flight Data From the PNI Micromag 3-axis Magnetometer.

Table C.1: Magnetometer Data Summary from North, East, South and West Runs

Dataset	M0x	M0y	M0z
northbound01	698	-14.5	1190
northbound02	699	7.99	1170
eastbound01	679	-12.5	1100
eastbound02	658	9.71	1100
southbound01	735	-48.7	884
southbound02	731	-58.9	892
westbound01	632	-35.6	1000

rotated in three dimensions back through the pitch and roll and heading angles as calculated at each point local magnetic field vector. The resulting magnetic field vector was much closer to having the same direction as the one offered by NOAA than the original data prescribed. The red line on each axis marks the mean of the earth frame magnetic field estimates.

The data in Table C.1 represents average earth frame magnetic field estimates over several runs on cardinal directions. The averages were taken after data corresponding to high pitch and roll angles was trimmed. The data shows good correspondence for magnetic field strength along each axis for each cardinal direction, giving confidence in the accuracy of the magnitude and direction for the local magnetic field. The second westbound data set was dropped because it was accidentally taken on an eastbound heading.

The average value for these data sets give a magnetic field vector in sensor counts of $B_0 = [690 \quad -21 \quad 1050]^T$ for a declination of $-1.8°$ and an inclination of $56.6°$. The NOAA[1] model gives $B_0 = [20969 \quad 4712 \quad 48314]^T$ in nanoTesla, indicating an declination of $12.6°$ and inclination of $65.4°$. These vectors are closer to similar than if the data had been taken without debiasing, in which case the inclination shows itself to be nearly 80°. It is possible that the local magnetic field is disturbed from the prevailing field.

---

[1] Available from http://www.ngdc.noaa.gov/seg/geomag/jsp/IGRF.jsp

Bibliography

[1] M. Akella, J. Halbert, and G. Kotamraju. Feedback control of rigid body attitude with inclinometer and low-cost gyro measurements. *Proceedings of the 11 th Annual AAS/AIAA Space Flight Mechanics Meeting, Santa Barbara, CA*, pages 545–553, 2001.

[2] M. Akella, J. Halbert, and G. Kotamraju. Rigid body attitude control with inclinometer and low-cost gyro measurements. *Systems and Control Letters*, 49(2):151–159, 2003.

[3] A. Brown and Y. Lu. Performance Test Results of an Integrated GPS/MEMS Inertial Navigation Package. *Proceedings of ION GNSS*, pages 21–24, 2004.

[4] R. S. Christiansen. Design of an autopilot for small unmanned aerial vehicles. Master's thesis, Brigham Young University, 2004.

[5] J. Crassidis, K. Lai, and R. Harman. Real-Time Attitude-Independent Three-Axis Magnetometer Calibration. *Journal of Guidance, Control, and Dynamics*, 28(1):115–120, 2005.

[6] D. Dungate, M. Allery, and M. Shelley. Generic robust attitude determination (grade). July 2002. http://www.cranfield.ac.uk/soe/space/papers2002.htm Session E: Technology and Subsystems.

[7] D. Gebre-Egziabher, G. Elkaim, J. Powell, and B. Parkinson. A gyro-free quaternion-based attitude determination system suitablefor implementation using low cost sensors. *Position Location and Navigation Symposium, IEEE 2000*, pages 185–192, 2000.

[8] A. Gelb, editor. *Applied Optimal Estimation*. The M.I.T. Press, 1974.

[9] T. Hamel and R. Mahony. Attitude estimation on SO (3) based on direct inertial measurements. *IEEE International Conference on Robotics and Automation, Orlando, Florida, May*, pages 15–19.

[10] S. Julier and J. Uhlmann. A new extension of the Kalman filter to nonlinear systems. *Proc. of AeroSense: The 11th Int. Symp. on Aerospace/Defence Sensing, Simulation and Controls*, 1997.

[11] R. Kalman. A new approach to linear filtering and prediction problems. *Transactions of the ASME-Journal of Basic Engineering*, 82:35–45, 1960.

[12] D. Kingston and R. Beard. Real-Time Attitude and Position Estimation for Small UAVs Using Low-Cost Sensors. *AIAA 3rd*, pages 2004–6488.

[13] D. B. Kingston. Implementation issues of real-time trajectory generation on small uavs. Master's thesis, Brigham Young University, 2004.

[14] M. Lundberg, P. Nordlund, and K. Stahl-Gunnarsson. Synthetic attitude and heading reference for Saab Gripen. *Decision and Control, 2000. Proceedings of the 39th IEEE Conference on*, 3:2040–2043, 2000.

[15] P. S. Maybeck. *Stochastic models, estimaion and control.* Academic Press, a Subsidiary of Harcourt Brace Jovanovich, New York, San Francisco, London.

[16] W. Phillips, C. Hailey, and G. Gebert. A review of attitude representations used for aircraft kinematics. *AIAA Journal of Aircraft*, 38(4):718–737, 2001.

[17] M. L. Psiaki. Attitude-determination filtering via extended quaternion estimation. *Journal of Guidance, Control, and Dynamics*, 23(2):206–214, March-April 2000.

[18] H. Rehbinder and X. Hu. Drift-free attitude estimation for accelerated rigid bodies. *Robotics and Automation, 2001. Proceedings 2001 ICRA. IEEE International Conference on*, 4:4244–4249, 2001.

[19] J. Roskam. *Airplane Flight Dynamics and Automatic Flight Controls.* DARcorporation, 1440 Wakaruse Drive, Suite 500, Lawrence, Kansas 66049 USA, 2001.

[20] S. Roumeliotis, G. Sukhatme, and G. Bekey. Smoother based 3D attitude estimation for mobile robot localization. *Robotics and Automation, 1999. Proceedings. 1999 IEEE International Conference on*, 3:1979–1986, 1999.

[21] J. Sedlak. Comparison of Kalman filter and optimal smoother estimates of spacecraft attitude. *In NASA. Goddard Space Flight Center, Flight Mechanics/Estimation Theory Symposium, 1994 p 431-445 (SEE N94-35605 11-13)*, 1994.

[22] M. Shuster. A simple Kalman filter and smoother for spacecraft attitude. *Journal of the Astronautical Sciences*, 37(1):89–106, 1989.

[23] M. Shuster. Kalman filtering of spacecraft attitude and the QUEST model. *Journal of the Astronautical Sciences*, 38:377–393, 1990.

[24] M. D. Shuster. A survey of attitude representations. *The Journal for the Astronautical Sciences*, 41(4):439–517, October - December 1993.

[25] B. L. Stevens and F. L. Lewis. *Aircraft Control and Simulation.* John Wiley & Sons, Inc, Hoboken, NJ, 2003.

[26] G. Welch and G. Bishop. An introduction to the kalman filter. A Course Packet to accompany Course 8 at ACM SIGGRAPH 2001.

[27] G. Welch and G. Bishop. *SCAAT: incremental tracking with incomplete information.* ACM Press/Addison-Wesley Publishing Co. New York, NY, USA, 1997.